

130073

NASA CR- [REDACTED]

Interhemispheric Comparison of Atmospheric Circulation

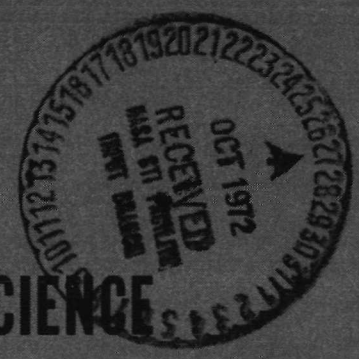
Features as Evaluated from NIMBUS Satellite Data



Annual Report

1 July 1971 — 30 June 1972

Grant NGR 06-002-098



DEPARTMENT OF ATMOSPHERIC SCIENCE
COLORADO STATE UNIVERSITY
FORT COLLINS, COLORADO

ANNUAL REPORT

for

Grant NGR 06-002-098

E. R. Reiter, Principal Investigator

1 July 1971 - 30 June 1972

Prepared by

E. R. Reiter, T. H. Vonder Haar, J. E. Lovill

R. Adler, S. Srivatsangam and Alice Fields

Department of Atmospheric Science

Colorado State University

for

National Aeronautics and Space Administration

Contracting Officer: J. B. Jishow

Technical Monitor : V. V. Salomonson

TABLE OF CONTENTS

	<u>Page</u>
SUMMARY.	1
1.0 INTRODUCTION TO GRANT OBJECTIVES.	2
2.0 DISCUSSION OF RESULTS	4
2.1 Use of Ozone to Study Atmospheric Transport Processes. . .	4
2.11 Meridional O ₃ Gradient vs. Jet Stream Maxima; Temporal and Geographical Variations of Ozone. . .	4
2.12 Extended Study of Mid-latitude Wave Patterns . . .	8
2.2 Atmospheric Thermal Structure from IRIS Spectra.	8
2.21 Results from Radiometric Inversion and from Direct Regression on Radiance Values.	11
2.22 Special Comparison with 30 mb Radiosonde Data. . .	33
2.23 Additional Comparison of Temperature-Radiance Relation for Cloud-Contaminated and "Cloudless" Data	43
2.3 Tropopause Temperature and Pressure Detection using IRIS Radiances.	48
2.31 Description of Method.	48
2.32 Comparison of Satellite-derived parameters with tropopause pressures and temperatures obtained from radiosondes	51
2.33 Comparison of Analyses of Tropopause Channel and Tropopause Radiance with Synoptic Conditions at 200 mb and with IRIS ozone analyses.	55
2.4 Special Supporting Data.	62
3.0 PROGRAM FOR THE NEXT REPORTING PERIOD	65
4.0 CONCLUSIONS AND RECOMMENDATIONS	67
5.0 REFERENCES.	69

APPENDIX I

Characteristics of the General Circulation of the Atmosphere and the Global Distribution of Total Ozone as Determined by the NIMBUS-III Satellite Infrared Interferometer Spectrometer (Ph.D. Dissertation by James E. Lovill) (attachment)

SUMMARY

With the completion of an extensive study of global ozone patterns, this project has moved into the diagnostic phase of investigation of interhemispheric circulation differences. Early results are most interesting and will soon be joined by studies of the atmospheric mass structure inferred from the satellite measurements.

The report includes a complete analyses of O_3 data inferred from NIMBUS-3 measurements, a discussion of future areas of study, description of the regression and inversion methods developed to infer atmospheric temperature and tropopause characteristics, as well as the plan to process the satellite data for a systematic study of the relative circulation differences between northern and southern hemispheres.

1.0 INTRODUCTION TO GRANT OBJECTIVES

It is the purpose of this research project to:

- a) Investigate, with the aid of satellite measurements, the fundamental processes and interactions affecting inter-hemispheric differences in mass structure and energetics, and
- b) To apply measurements from satellites to the problem of large-scale global weather forecasting.

In this, the second, annual report we present results of studies using measurements of infrared radiance from the Infrared Interferometer Spectrometer (IRIS) flown on NASA's NIMBUS-3 satellite. These data, with the aid of NASA, have been analysed selectively to study the x , y , t distribution of atmospheric ozone and its relation to large-scale circulation parameters. The satellite data provide a global view during the period April-July, 1969. Dr. James Lovill, as his dissertation, has examined this ozone climatology, compared it with ground-based observations, and used it to infer the characteristics of regional and planetary scale circulation systems in both the Northern and Southern Hemispheres. In addition to the study of mid-latitude waves, reported herein, O_3 data are used to infer the magnitude of jet stream wind maxima and for other special studies.

From the same atmospheric spectra used to derive O_3 , selected spectral radiance measurements have been used by Mr. S. Srivatsangam to obtain vertical temperature profiles in both hemispheres from a statistical inversion method developed by Rodgers (1969). Together with a less complex regression method to determine upper tropospheric temperature from radiance, the satellite results are "calibrated" over the Northern Hemisphere using standard NMC data. Examples of the results are included in this report.

Mr. Robert Adler has devised a special technique to detect tropopause temperature and pressure using IRIS data. This allows rapid inference of inter-hemispheric circulation differences and may be a great aid to operational use of satellite data. Both he and Srivatsangam plan to use the extensive satellite data set to study the geopotential height fields, the available potential and kinetic energy magnitudes of each hemisphere.

Special data used in support of the satellite measurements include ground-based ozone measurements, conventional meteorological analyses over the Northern Hemisphere and a 5-year set of upper air wind data from the Australian sector. Further work will include Selective Chopper Radiometer (SCR), Satellite InfraRed Spectrometer (SIRS), and IRIS measurements from the NIMBUS-4 as well as results from the EOLE experiment.

The following sections provide a more detailed discussion of grant research. It is without doubt that a controlled use of the recently available satellite measurements to study the circulation differences between Northern and Southern Hemispheres offers atmospheric scientists a potential quantum-jump in knowledge regarding the significant processes and interactions and their natural variation.

2.0 DISCUSSION OF RESULTS

2.1 Use of Ozone to Study Atmospheric Transport Processes

2.11 Meridional O_3 gradient vs. jet stream maxima; temporal and geographical variations of ozone

Studies in recent years have shown distinct differences of the atmospheric general circulation of the Northern and Southern Hemispheres. Earlier publications postulated a more zonal flow in the Southern Hemisphere supposedly because of less land mass and fewer mountain massifs. More recent investigations show that such statements need to be qualified.

Wooldridge and Reiter (1970) have shown that significantly stronger horizontal anisotropy of flow prevails at cyclone wavelengths in the Southern Hemisphere than in the Northern Hemisphere. In the Southern Hemisphere meridional perturbations exceed zonal flow perturbations. Eulerian spectral densities of the zonal component in the Southern Hemisphere were seen to be only half of those in the Northern Hemisphere. This would seem to imply that there is less zonal energy at cyclone-wave frequencies in the Southern than in the Northern Hemisphere. This may occur because of a lack of orographically induced planetary longwaves in the Southern Hemisphere that are superimposed upon the hemispheric jet stream zones. Apparently the relatively zonal character of the Southern Hemisphere pertains to the long planetary-scale waves only.

Interest in global total ozone measurements is widespread and increasing. The paucity of total ozone measuring stations over the oceans and in the tropics in the Northern Hemisphere and throughout

the Southern Hemisphere has greatly hindered a complete understanding of the role that stratospheric ozone plays in the general circulation processes of the atmosphere. With total ozone sensors (such as the IRIS instrument) on earth-orbiting satellites the ozone over the entire earth is measured daily. The conclusions of some of the analysis from the first satellite (Nimbus III) capable of these measurements follow.

A statistical analysis of the total ozone data for two days indicated that average standard error between data obtained by the inversion technique and data obtained by regression coefficients was only 3.7 percent. When surface total ozone measurements were compared with regression data at monthly intervals a standard error of 3.6 percent was seen.

A strong correlation was discovered between the meridional gradient of total ozone and the wind velocity in jet stream systems. A graph has been constructed which will allow the computation of the wind velocity at 250 mb if the total ozone distribution in the vicinity is known. This should be a very useful relation to apply over the oceanic regions of the Northern Hemisphere and throughout the entire Southern Hemisphere. Wind velocities at jet aircraft operation levels could then be forecasted by consulting the daily satellite total ozone analysis. This method to obtain wind velocity might ideally complement the technique to infer upper troposphere wind direction, based on water vapor measurements, being developed at NASA.

A study of the total ozone distribution over a Pacific Ocean extratropical cyclone and its associated jet stream indicated large vertical motions and strong horizontal advective processes were present near this

system. Large amounts of total ozone were measured immediately behind the system and low amounts in front which were indicative of air rich in ozone moving southward and downward behind the system and air poor in ozone moving northward and upward in front of the storm.

Time-longitude variations of the total ozone for several latitudes in the Northern and Southern Hemisphere for June 1969 were analyzed. Several interesting facts were seen in these results. Firstly, one can observe that the speed at which the 'waves' progress eastward is greater in the winter hemisphere (here the Southern Hemisphere). Secondly, the speed of eastward progression decreases as one approaches the lower latitudes in the winter hemisphere. Thirdly, in the equatorial region and in the Northern Hemisphere there is not a strong eastward progression of 'waves' but at best only weak eastward movement. Progression rates as high as fifteen degrees of longitude per day were seen at the high latitudes in the Southern Hemisphere. As one follows the 'waves' in time, continuous changes in intensity are observed (see also 2.12).

When total ozone data for the period of observations are plotted against latitude for the various months the following is indicated. For the first time the average distribution of ozone has been described during the autumn and winter at close intervals, both temporally and spatially, in the Southern Hemisphere. The smallest variation of total ozone from spring to summer was seen at 15°N . The lowest mean total ozone value for the globe was at 6°S .

When two maps were prepared describing the distribution of total ozone for the entire period for the Northern and Southern Hemispheres, the following was seen. Closely spaced total ozone isolines appear to have revealed a reasonably strong jet stream west of South America at

approximately 35°S . This system, at least at the intensity indicated by the total ozone gradient, has gone more-or-less unnoticed in the past.

Additionally, a large region of low total ozone was observed in the tropics, extending from southeast Asia eastward to the central Pacific. Earlier studies have indicated that this region also has an anomalously high albedo. The manner by which this correlates with low total ozone concentrations is not at all clear.

Both the Northern and Southern Hemispheres appear to provide 'anchoring' mechanisms for total ozone ridges. The most predominant of the ridges is also usually associated with a 'tight' ozone gradient. In the Northern Hemisphere these locations are eastern North America, central Europe, western Asia, and eastern Asia. The ridge over the Soviet Union appears to be the weakest of the four ridges. In the Southern Hemisphere 'ozone' ridges are evident over the east Indian Ocean, the central Pacific Ocean and the eastern Atlantic. In general, the ridge pattern is easier to delineate in the Southern Hemisphere than in the Northern Hemisphere.

The 'tightest' gradient of total ozone in either hemisphere was seen over Japan. This correlates closely with the high frequency of jet streams observed over the region.

An average global value of the total ozone for the entire period was calculated to be $330.3 \text{ m}\cdot\text{atm}\cdot\text{cm}$.

A paper containing these results in detail is enclosed as Appendix I to this report.

2.12 Extended study of mid-latitude wave patterns

Special time-space displays of the ozone data are being used in an extended study of mid-latitude wave patterns. This work will be summarized in a special report, now in preparation.

2.2 Atmospheric Thermal Structure From IRIS Spectra

Recent research under this grant (Reiter, et al., 1971) using some 88 near-simultaneous ($\Delta t \leq 3$ hours) radiosonde and IRIS radiance observations indicate that in the stratosphere the correlations between the ambient temperatures and the radiances of the infrared wave-numbers weighted predominantly in this atmospheric layer (such as 675 cm^{-1}) are so significant that temperatures inferred directly from the scatter-diagrams are comparable in accuracy to radiosonde observations. Differences between the inferred temperatures and the NMC grid temperatures a few hours apart are of the order of 2°C .

However, isobaric level temperatures in the troposphere and the radiances of the IR wave-numbers weighted significantly about these levels show such a wide scatter that direct inference of temperatures from the scatter-diagrams is impossible. This difficulty leads one to the use of other, and generally computationally more costly, methods of analysis in order to study stratosphere-troposphere interaction using satellite data.

The method due to Rodgers (1970), which we have decided to employ, uses estimation theory as a means to invert the linearised radiative transfer equation to obtain atmospheric vertical temperature profiles. Two important constraints are imposed by this method on the resulting

data for analysis. One is its limitation to clear-sky cases only and the other is the satisfaction of the linearity criterion mentioned above. The differentiation between cloudy and clear sky cases is discussed in both 2.21 and 2.23.

More important than the vertical thermal structure in the analysis of tropospheric circulation features is the distribution of mass. Despite the inter-relationship between the mass and temperature fields "there is no method of inferring the sea-level pressure field hydrostatically from the three-dimensional temperature field alone" (Lorenz, 1967, p. 28) and, because of this restriction it would not be possible to obtain the geopotential height of a given isobaric level from the temperature profile only. Statistical analysis (Smith and Fritz, 1969) shows that this is not an unavoidable condition.

In our own analysis here at Colorado State University we intend to derive, at the present time, only the relative height fields (Z' -fields) of some 5 isobaric levels from 100 mb to 700 mb. The Z' -fields (deviations from the mean \bar{Z} for an area S comparable to the area of a hemisphere) are expressible in terms of fast-converging empirical orthogonal functions F_k and their coefficients Z_k as

$$Z' (x, y, p, t) = \sum_{k=1}^n Z_k (x, y, t) F_k (p, t) \quad (1)$$

The analytical solution of equation (1) as given by Holmström (1963; see also Obukhov, 1960) is

$$\left. \begin{aligned} \frac{1}{p} \int_p (Z' - \sum_{k=1}^{n-1} Z_k F_k) F_n dp &= Z_n, \\ \int_S (Z' - \sum_{k=1}^{n-1} Z_k F_k) Z_n ds &= F_n \int_S Z_n^2 ds \end{aligned} \right\} \quad (2)$$

We have developed a program for evaluating Z_k and F_k , and used it for computations in the range $k \leq 6$, $P = 1000$ mb to 100 mb and $P = 700$ mb to 100 mb.

By using the hydrostatic equation and the equation of state in (1) we obtain

$$t' = -\sum \frac{Z_k}{R} g \frac{d}{dp} F_k \quad (3a)$$

$$= \sum_k Z_k \varepsilon_k \quad (3b)$$

where ε_k are defined through (3a) and t' are defined as temperature deviations from the area mean, analogous to Z' (see Smith et al., 1970 and Holmström, 1963). From (3b) and (1) the Z' -field is obtained from the t' -field through the matrix equation

$$Z' = t' \varepsilon^{-1} F \quad (4)$$

We have solved equation 4 for the data of 10 July 1969. The first results indicate considerable deviations from actual values. It is not clear whether the 5-mode solution is over-descriptive or under-descriptive. Holmström (1963) says the functions $\tau_k(p)$ which he develops for the temperature-field from $F_k(p)$ are not fast-converging. On the other hand Z_5 's are very small, especially when F_k are normalized in the interval 700 mb-100 mb. We are trying to evaluate equation (4) with a 4-mode system.

If subsequent results are encouraging we intend to use empirical orthogonal functions to the vorticity tendency equation, first with conventional data and later with IRIS-derived Z' -field data. Initial theoretical considerations indicate that such an analysis would enable

the separation of different atmospheric developmental processes such as the development of the semi-permanent high and lows and baroclinic development due to ultra-long and cyclone waves.

Should the empirical orthogonal function approach prove not to be a feasible one, our circulation studies would still be based on:

- a) studies of the time and space variation of the mean temperature of atmospheric layers, and/or
- b) geopotential height fields derived using a regression method very similar to the one employed operationally with the SIRS data

Throughout the remainder of this section we report on results of inferring the atmospheric temperature at distinct levels. This is a fundamental step that allows us to compare with other work of this type. However, for our circulation study, the comparisons with NMC data must be regarded as worst-case since random errors in temperature retrieval that affect RMS level comparison are removed from atmospheric layer (mass) comparisons.

2.21 Results from radiometric inversion and from direct regression on radiance values

The InfraRed Interferometer spectrometer, IRIS, is a Michelson interferometer employing a beamsplitter which divides the incoming radiation into two approximately equal components, one of which is made to reflect from a stationary mirror and the other from a moving mirror. The interference of the two beams produces an interference pattern (interferogram) from which a radiation spectrum is constructed by applying the inverse Fourier transform. Spectral radiances in wave-number bands of 5 cm^{-1} can be obtained from this spectrum. The weighting functions K_i for these bands in a vertical atmospheric

column are given by

$$K_i = \frac{d\tau_i}{d \ln p} \quad (5)$$

where τ_i is the transmissivity of the atmosphere in the i^{th} wave-number interval. The weighting functions for such wavenumber intervals in the $15\mu\text{m CO}_2$ band, some of which we used to retrieve atmospheric temperatures by Rodgers' (1970) method, are given in Figure 1.

Our aim was to obtain temperatures at 6 isobaric levels, viz., 700 mb, 500 mb, 400 mb, 200 mb, 100 mb and 30 mb. Cloud interference makes the retrieval of tropospheric temperatures difficult. One solution to the problem is to prescribe sufficiently accurately, a set of parameters such as the surface temperature in the field of view of IRIS and cloud-top heights. (For other usable sets of parameters see Chahine (1970)). In an iterative procedure such as the one described by Smith et al. (1970)--where cloud-top heights are treated as variables--the only parameter needed, in addition to the spectral radiances themselves, is the surface temperature. This can be accomplished over oceans by using independent satellite observations whereas, over land the diurnal temperature variation makes this rather difficult to carry out.

Another way of solving the cloud problem would be to prescribe adequate lower limits for spectral radiances whose weighting curves for the gaseous atmosphere peak in the lower troposphere and therefore would be affected significantly by clouds at any level in the atmosphere. Thus clear-sky and cloudy areas in a region (such as a latitude band) could be distinguished. 745 cm^{-1} is a wave-number that satisfies this criterion (see Figure 1). Radiances in the window region, which are influenced primarily by surface and cloud-top temperatures could also be used this way, but these depend very much on surface characteristics.

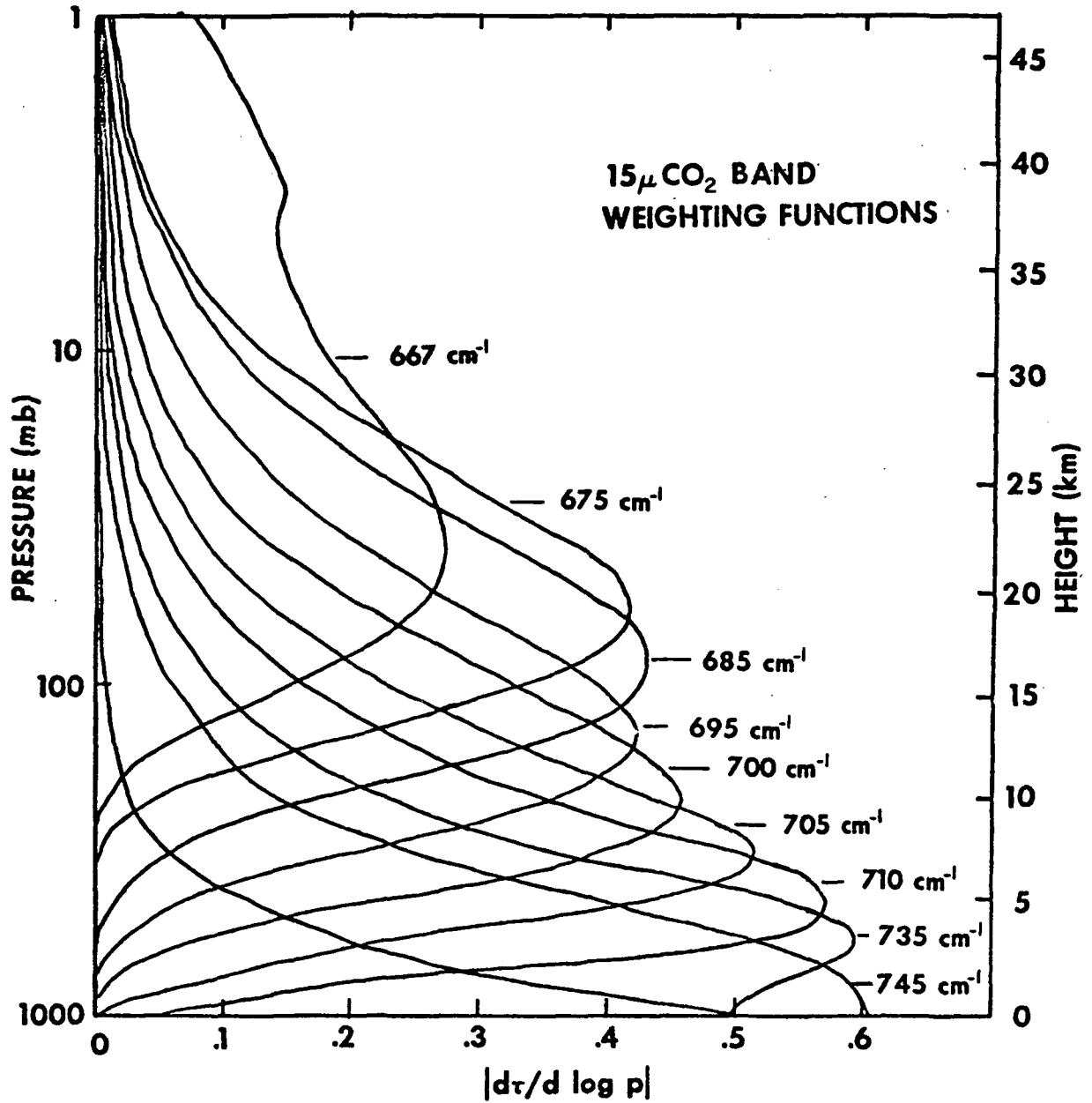


Fig. 1 - Atmospheric weighting functions for 667 cm⁻¹ (15 μ m) CO₂ absorption band. The curves were calculated assuming an instrument function 5 cm⁻¹ wide at the half maximum point, centered on the wave number indicated. (After Conrath, et. al., 1970).

TABLE 1

Limiting values of 745 cm^{-1} radiances for distinguishing between clear and cloudy areas. T_{bb} is equivalent black body temperature in degrees centigrade.

Latitude Band (Degrees)	Initial Values		Values when lower tropospheric deviations are random	
	745 cm^{-1} $\text{erg cm}^{-1} \text{ s}^{-1} \text{ sr}^{-1}$	T_{bb} Degrees C	745 cm^{-1} $\text{erg cm}^{-1} \text{ s}^{-1} \text{ sr}^{-1}$	T_{bb} Degrees C
0-30	80	-14.0	90	- 6.6
30-60	78	-15.6	85	-10.2
60-81	68	-23.6	80	-14.0

Since the satellite observations are made (in the case of NIMBUS III which carried IRIS) very nearly at local noon and midnight except at subpolar latitudes allowance has to be made for the diurnal temperature variation over land. Wave-number 745 cm^{-1} is much less dependent upon surface thermal characteristics and obviates the need for ocean surface temperature and therefore was used. The limiting values used for different latitude bands are listed in Table 1. Atmospheric temperatures obtained under such criteria and using Rodgers' (1970) method were interpolated linearly from the subsatellite track to a 5° latitude by 5° longitude grid for the Northern Hemisphere. The data were again interpolated using a 16 point Bessel interpolation to fill the NMC grid points. Contours fitted for these data using a CDC user program were plotted on microfilm by a CDC 6400 Computer. From these analyses, data for locations corresponding to 20 Eurasian and 18 North American radiosonde stations were collected and plotted against the actual radiosonde data for each of the levels mentioned above. (The North American radiosonde data are for 1200 GMT and the Eurasian ones for 0000 GMT; so the local time is approximately the same for Asian and American data.) The scatters were studied for any consistent (bias) deviations of the IRIS-derived temperatures from the radiosonde observations. Since we started with low limits for 745 cm^{-1} radiances the initial IRIS-derived temperatures were colder than radiosonde temperatures at the 700 mb and 500 mb levels. So the limiting 745 cm^{-1} radiance values were raised, and the new scatters checked and the procedure repeated until the errors at the lower tropospheric levels were completely random. Under such conditions the RMS deviation of the IRIS-derived temperatures is sufficiently independent of any cloud influence. The values of 745 cm^{-1} radiances for which the errors at the 700 mb

TABLE 2

RMS and mean deviations for the data presented in Fig. 2, which are for days 3 and 8 July, 1969.

Level (mb)	RMS Deviations (Deg. C)		Mean deviation of IRIS-derived temp. from radiosonde temp. (Deg. C)*	
	Eurasian data	All data	Eurasian data	All data
700	3.61	3.78	0.29	0.11
500	2.76	2.87	0.18	0.31
400	3.14	3.46	0.48	0.99
200	4.18	3.78	-0.38	-0.92
100	2.39	2.94	0.08	-0.25
30	2.15	3.24	0.92	2.16

* Hence a positive value indicates a warmer radiosonde temperature compared to IRIS-derived temperature.

and 500 mb levels were completely random are presented in Table 2. The r.m.s. error is much larger at the 700 mb level compared to the r.m.s. error at the 500 mb level. The final IRIS-derived temperatures plotted against radiosonde temperatures for all the levels considered are presented as Figures 2a - 2f.

The r.m.s. errors are generally smaller for the Eurasian data than for the combined Eurasian-North American data, as seen from Table 2. Since there is no reason to expect that the analytical method employed here has any regional bias, this increase in error for the combined data might be attributed to the time difference between the satellite and radiosonde observations. This difference is larger for North America and smaller for Eurasia, but is close to zero even here only at 0000 GMT. Thus, at least part of the r.m.s. errors of Table 2 might be due to time difference in observations.

In our earlier report (Reiter, et al., 1970) a scatter diagram for 100 mb temperatures against $\nu = 675 \text{ cm}^{-1}$ radiances was given. For that scatter a third degree curve seemed to be in best fit. 100 mb temperatures for 2 days in July 1969 were obtained from this curve. Distributions of these temperatures in the NMC grid area are presented here (Fig. 3a and 3e) and compared to the NMC temperature distribution (Fig. 3c, 3d, 3g and 3h) at 0000 GMT and 1200 GMT on the same days. The distributions obtained by using Rodgers' (1970) method are also presented (Fig. 3b and 3f). A comparison of these three types of distributions indicates that in general there is qualitative agreement between them both in temperature gradients (and hence in thermal wind shears) as well as in contour orientation (i.e., trough-ridge location). The results obtained are good considering the inability of the present

FIGURE 2a

Level: 700mb

Scatter of IRIS-derived temp. (Deg. C) against Radiosonde temp. (Deg. C)

OO EURASIAN RADIOSONDES (0000 GMT)

++ N. AMERICAN RADIOSONDES (1200 GMT)

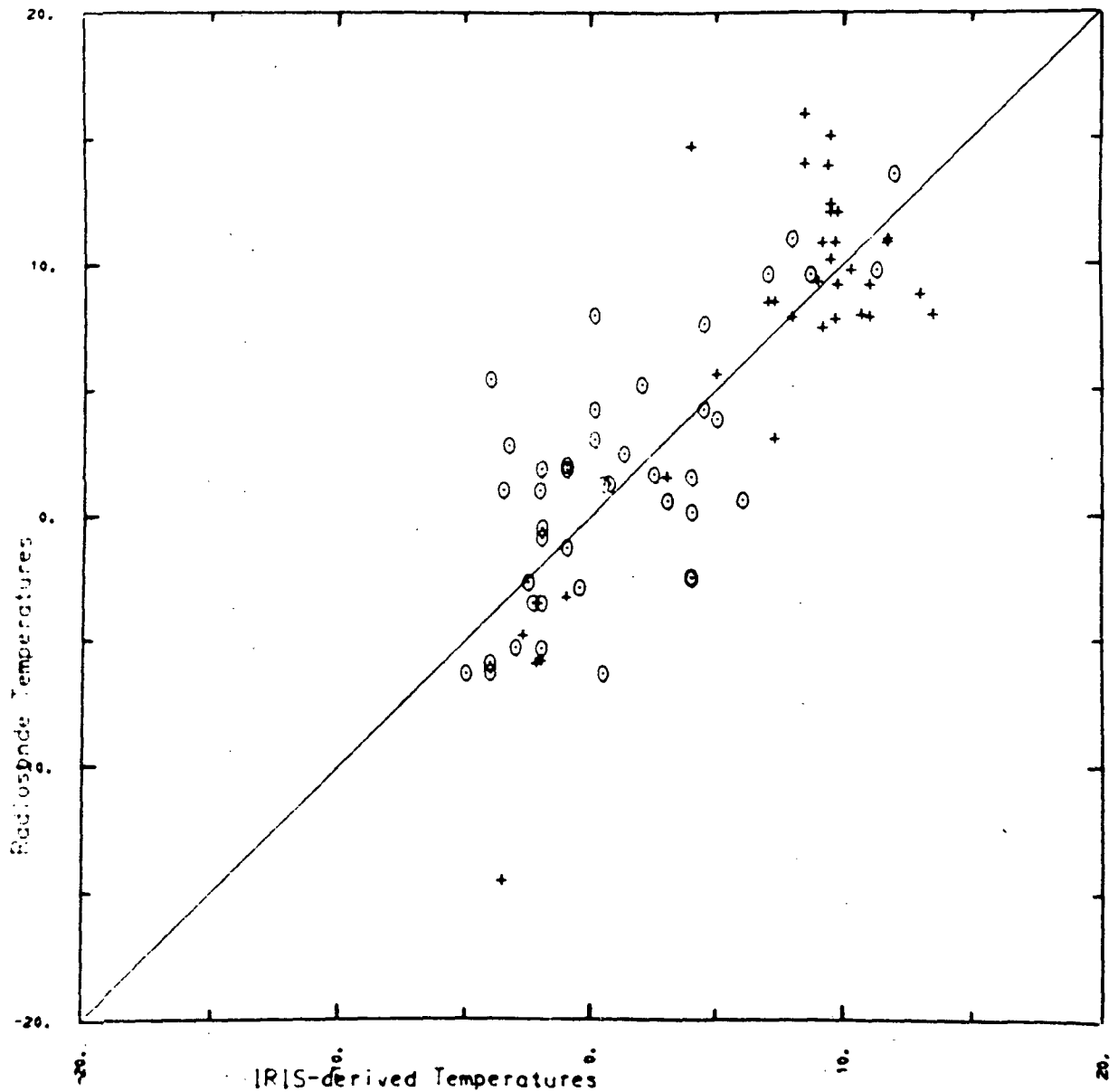


FIGURE 2b

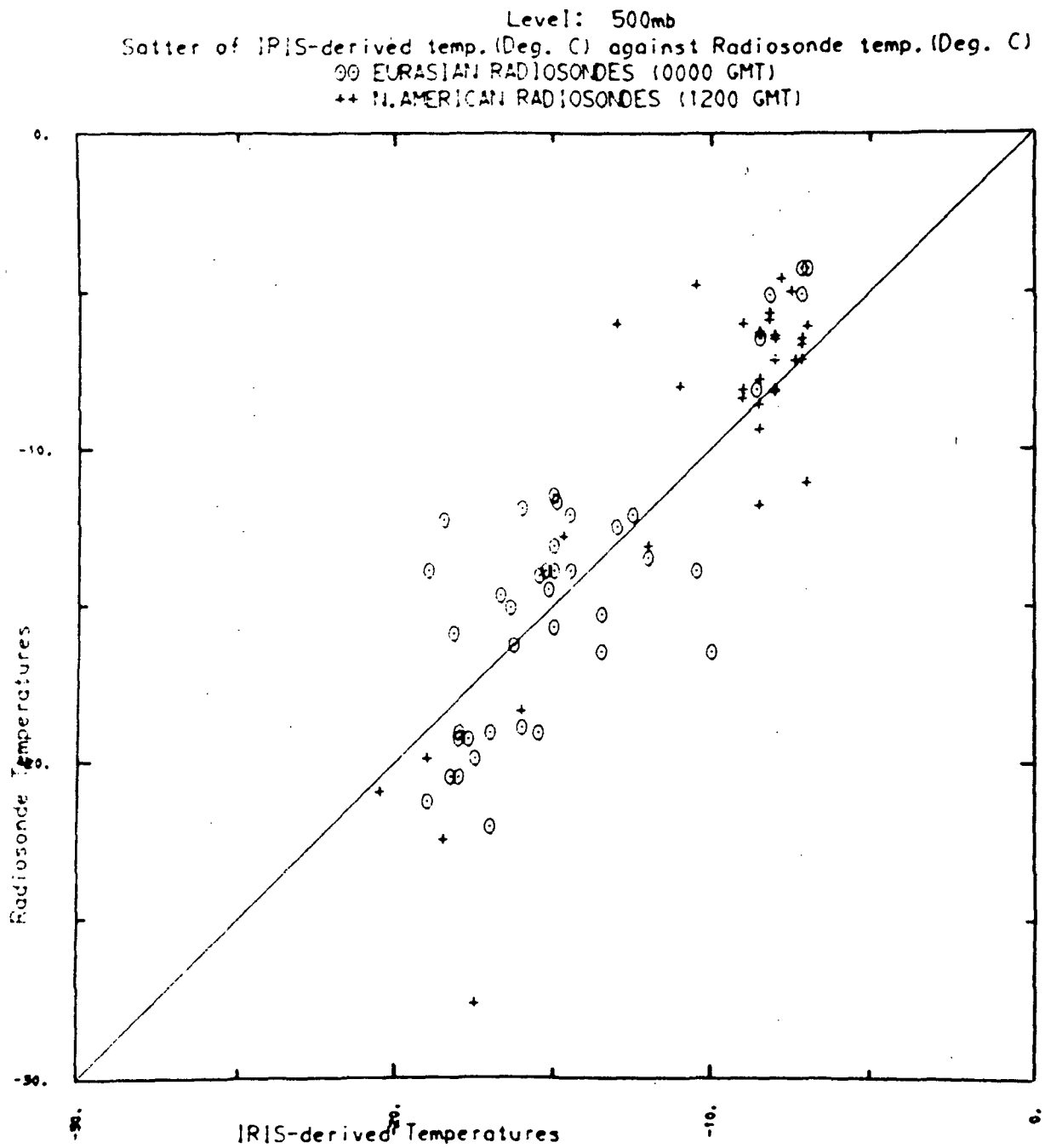


FIGURE 2c

Level: 400mb
Scatter of IRIS-derived temp. (Deg. C) against Radiosonde temp. (Deg. C)
OO EURASIAN RADIOSONDES (0000 GMT)
++ N. AMERICAN RADIOSONDES (1200 GMT)

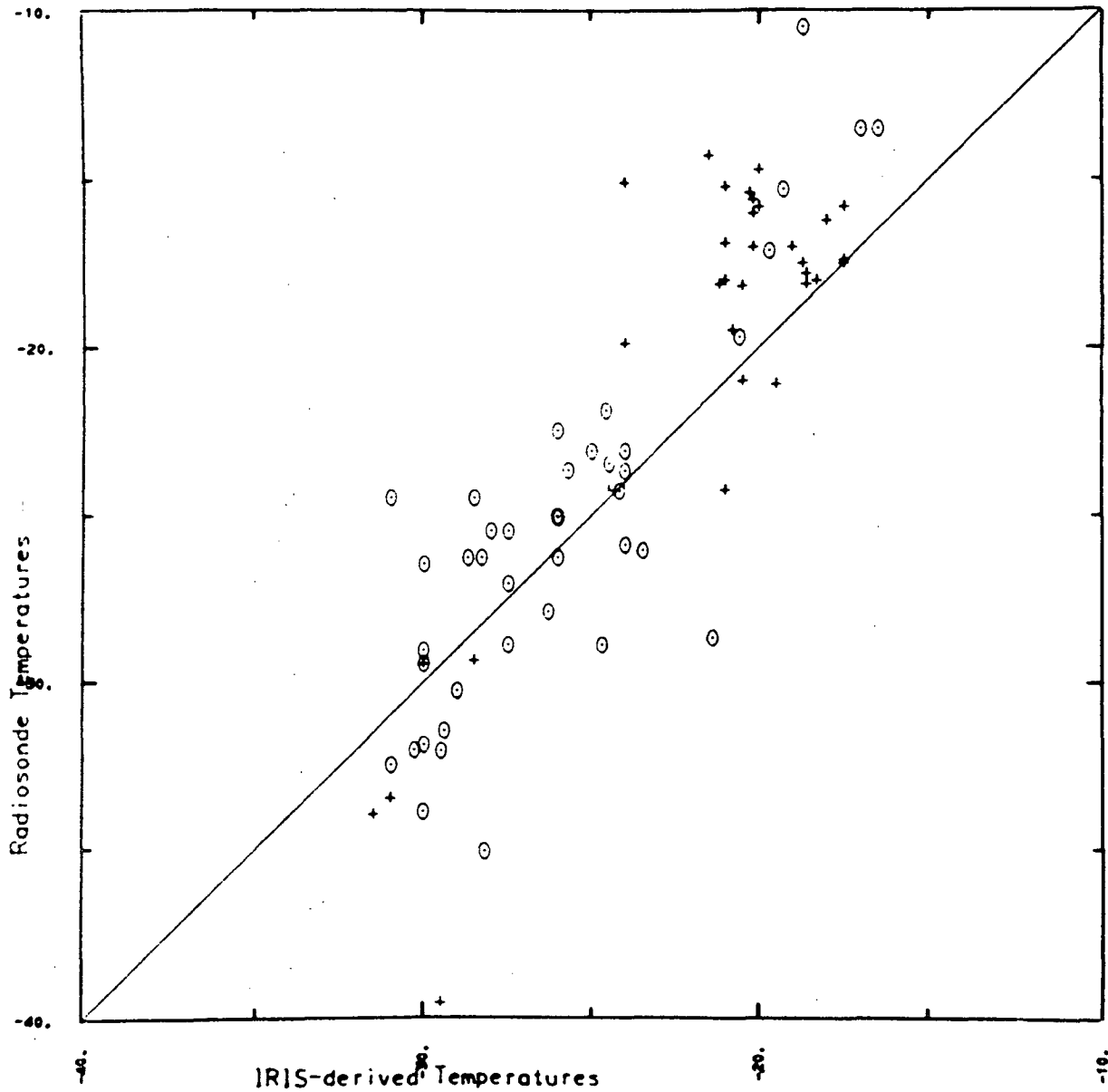


FIGURE 2d

Level: 200mb

Scatter of IRIS-derived temp. (Deg. C) against Radiosonde temp. (Deg. C)

OO EURASIAN RADIOSONDES (0000 GMT)

++ N. AMERICAN RADIOSONDES (1200 GMT)

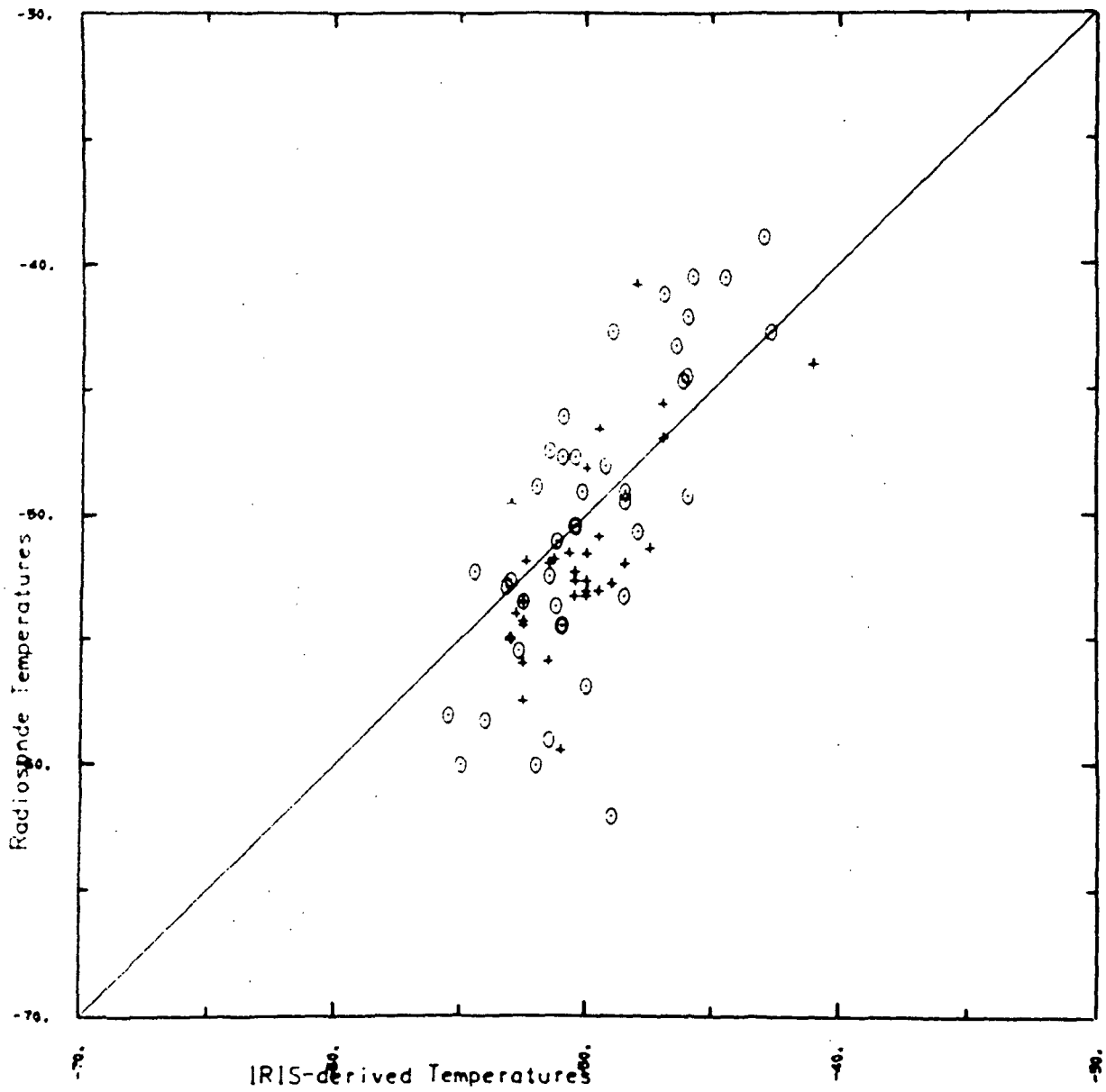


FIGURE 2e

Level: 100mb

Satter of IRIS-derived temp. (Deg. C) against Radiosonde temp. (Deg. C)

OO EURASIAN RADIOSONDES (0000 GMT)

++ N.AMERICAN RADIOSONDES (1200 GMT)

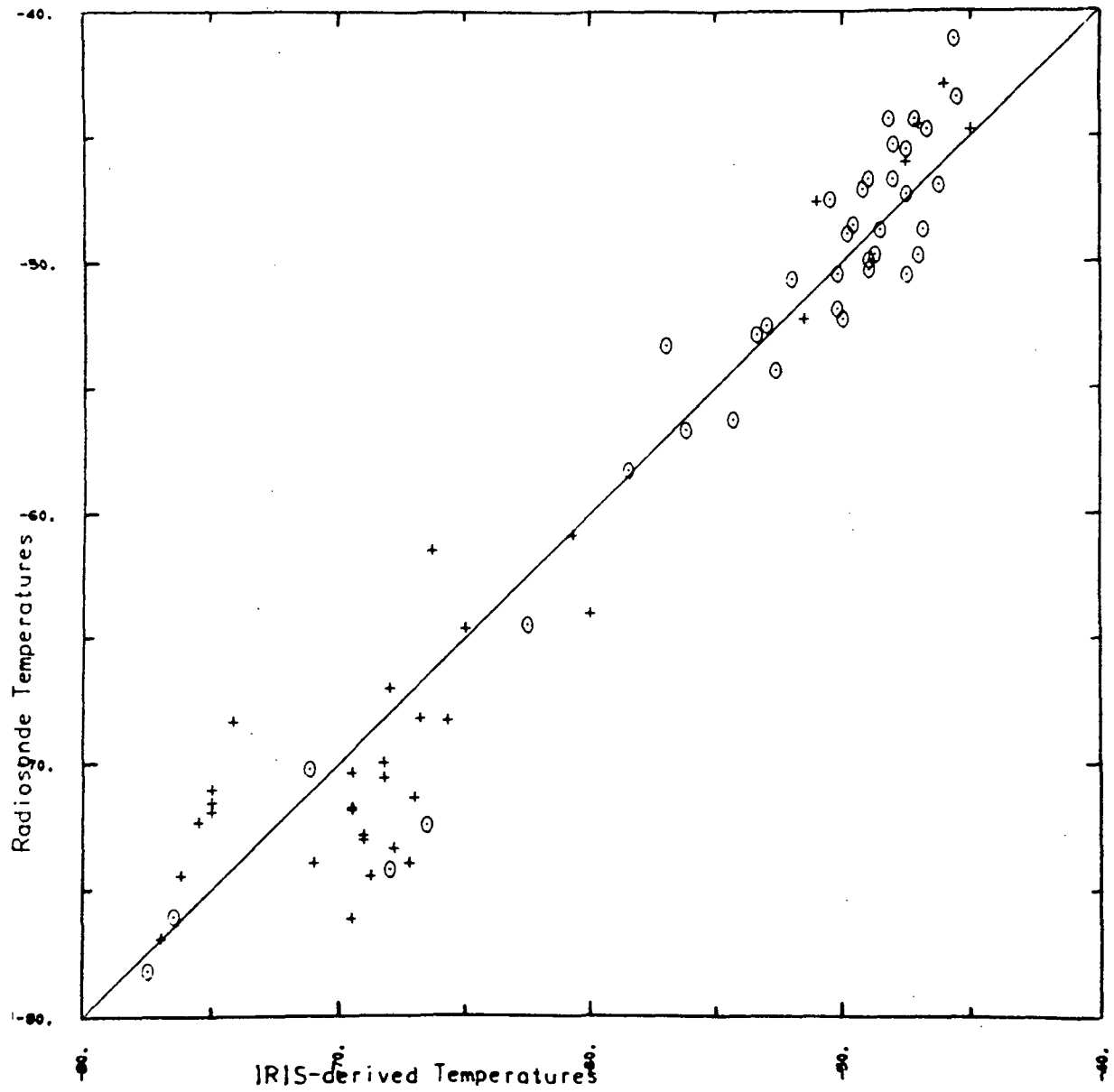


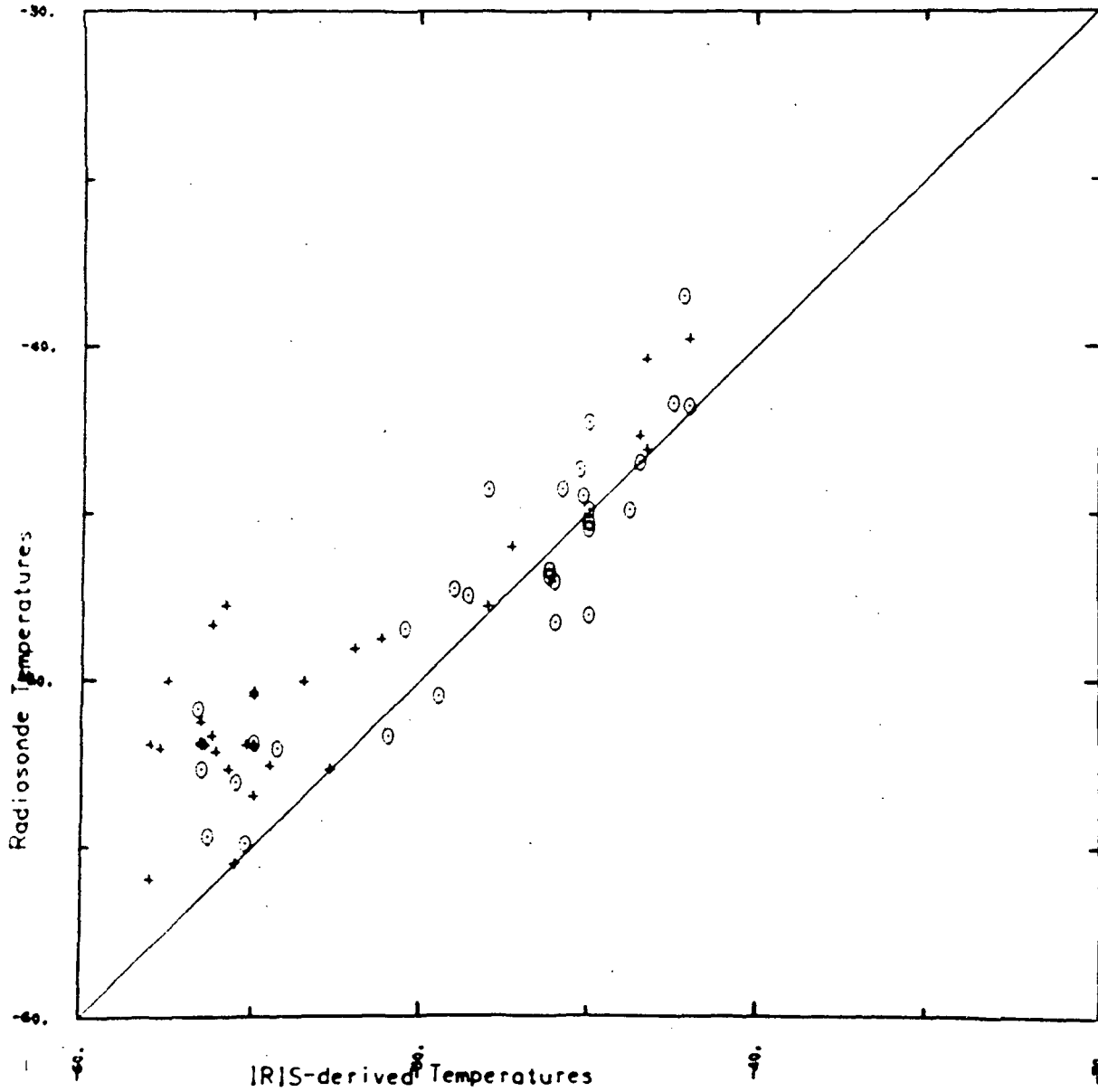
FIGURE 2f

Level: 30mb

Scatter of IRIS-derived temp. (Deg. C) against Radiosonde temp. (Deg. C)

OO EURASIAN RADIOSONDES (0000 GMT)

++ N. AMERICAN RADIOSONDES (1200 GMT)



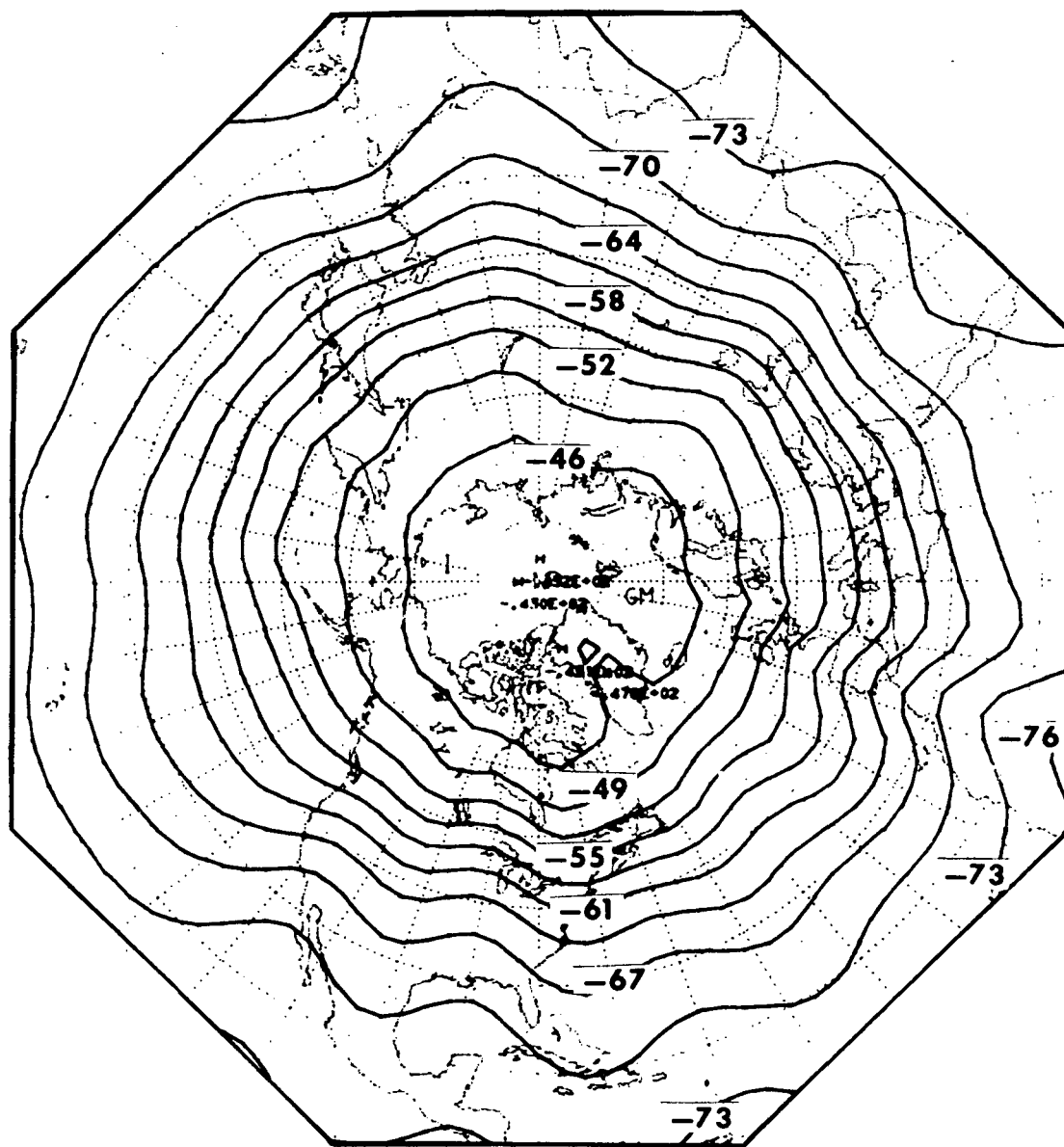


Fig. 3a - 100 mb temperatures (Degrees C.) obtained by correlation between $\nu = 675 \text{ cm}^{-1}$ radiances and 100 mb temperatures. 3 July 1969. Number of data points 1597.

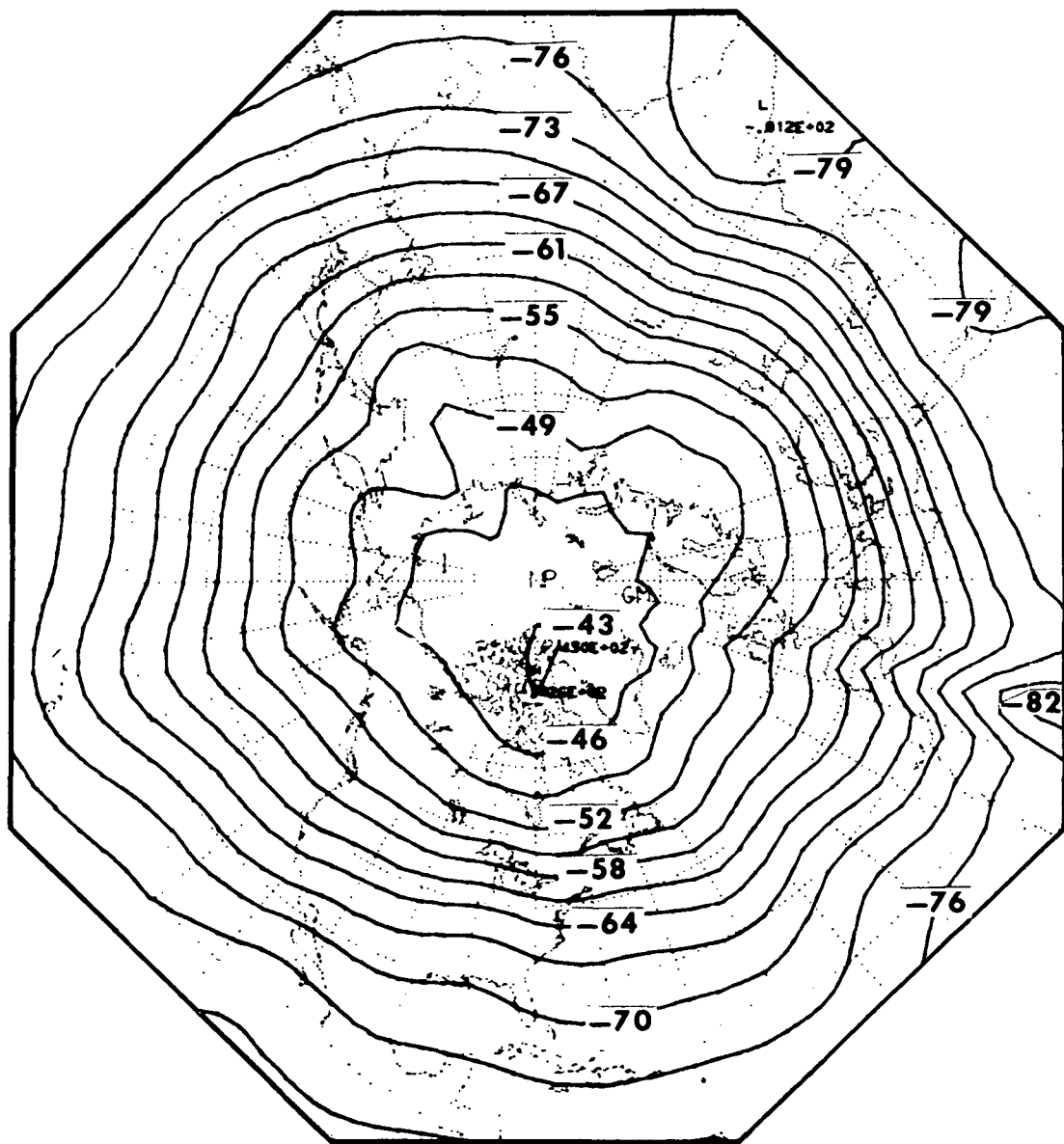


Fig. 3b - 100 mb temperatures (Degrees C.) obtained from InfraRed Interferometer Spectrometer (IRIS) spectral radiances using Rodgers' (1970) method. 3 July 1969. Number of data points 311.

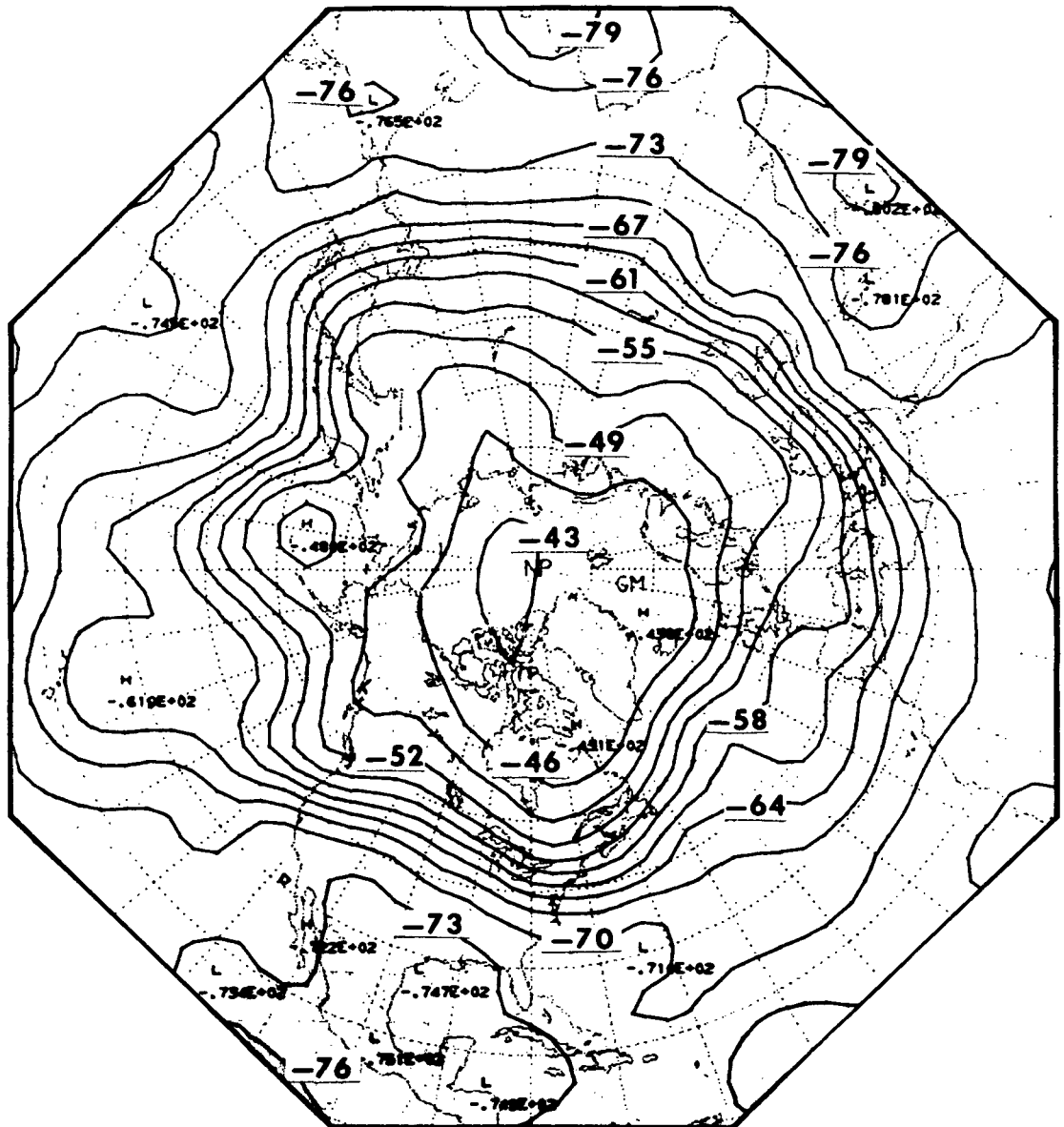


Fig. 3c - Northern Hemisphere Radiosonde temperatures (Degrees C.) at 100 mb. National Meteorological Center (NMC) mapping. 8 July 1969. 0000 GMT.

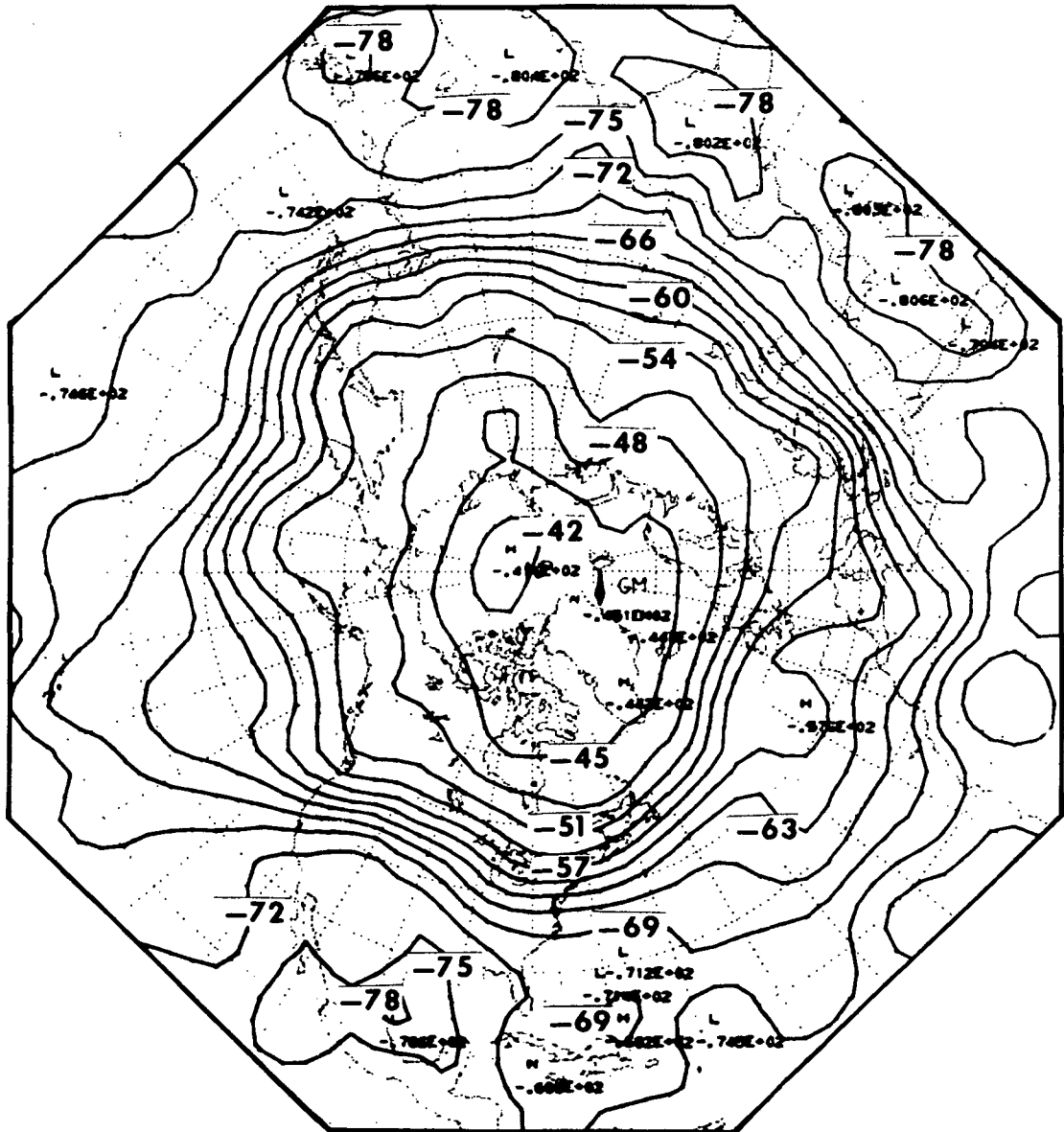


Fig. 3d - Northern Hemisphere Radiosonde temperatures (Degrees C.) at 100 mb. National Meteorological Centre (NMC) mapping. 3 July 1969. 1200 GMT

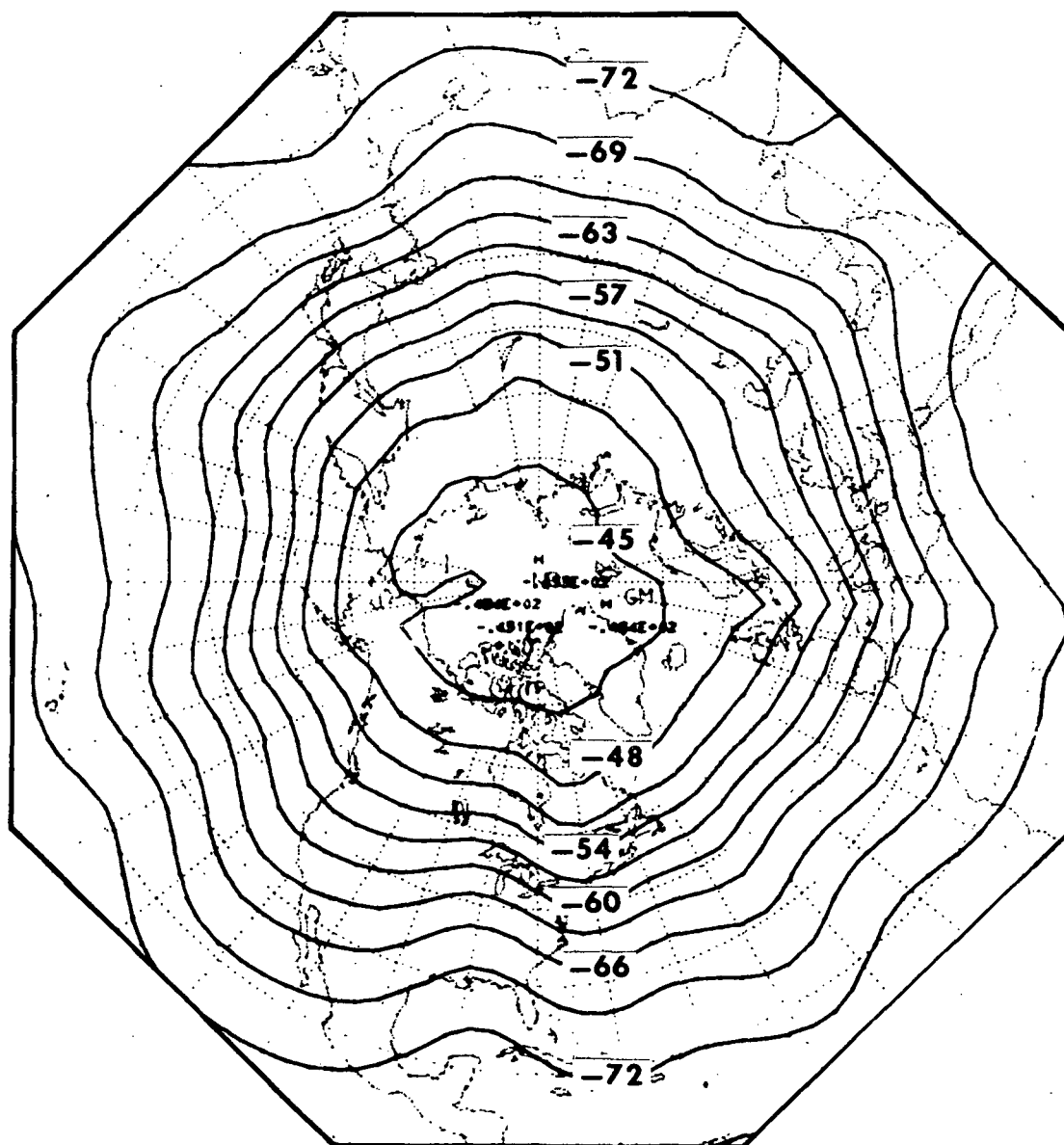


Fig. 3e - 100 mb temperatures₁ (Degrees C.) obtained by correlation between $\nu = 675 \text{ cm}^{-1}$ radiances and 100 mb temperatures. 8 July 1969. Number of data points 1193.

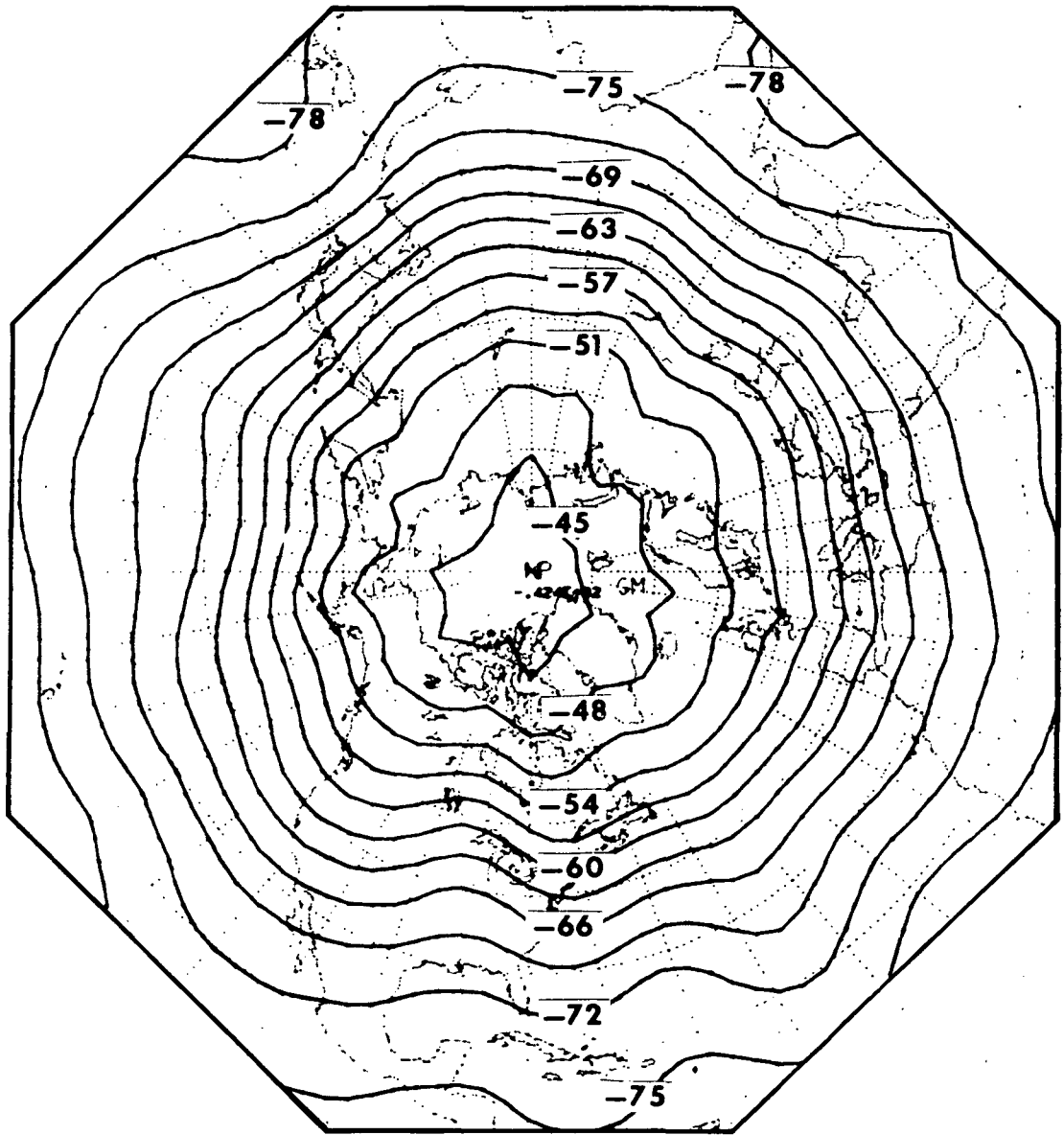


Fig. 3f - 100 mb temperatures (Degrees C.) obtained from InfraRed Interferometer Spectrometer (IRIS) spectral radiances using Rodgers' (1970) method. 8 July 1969. Number of data points, 271.

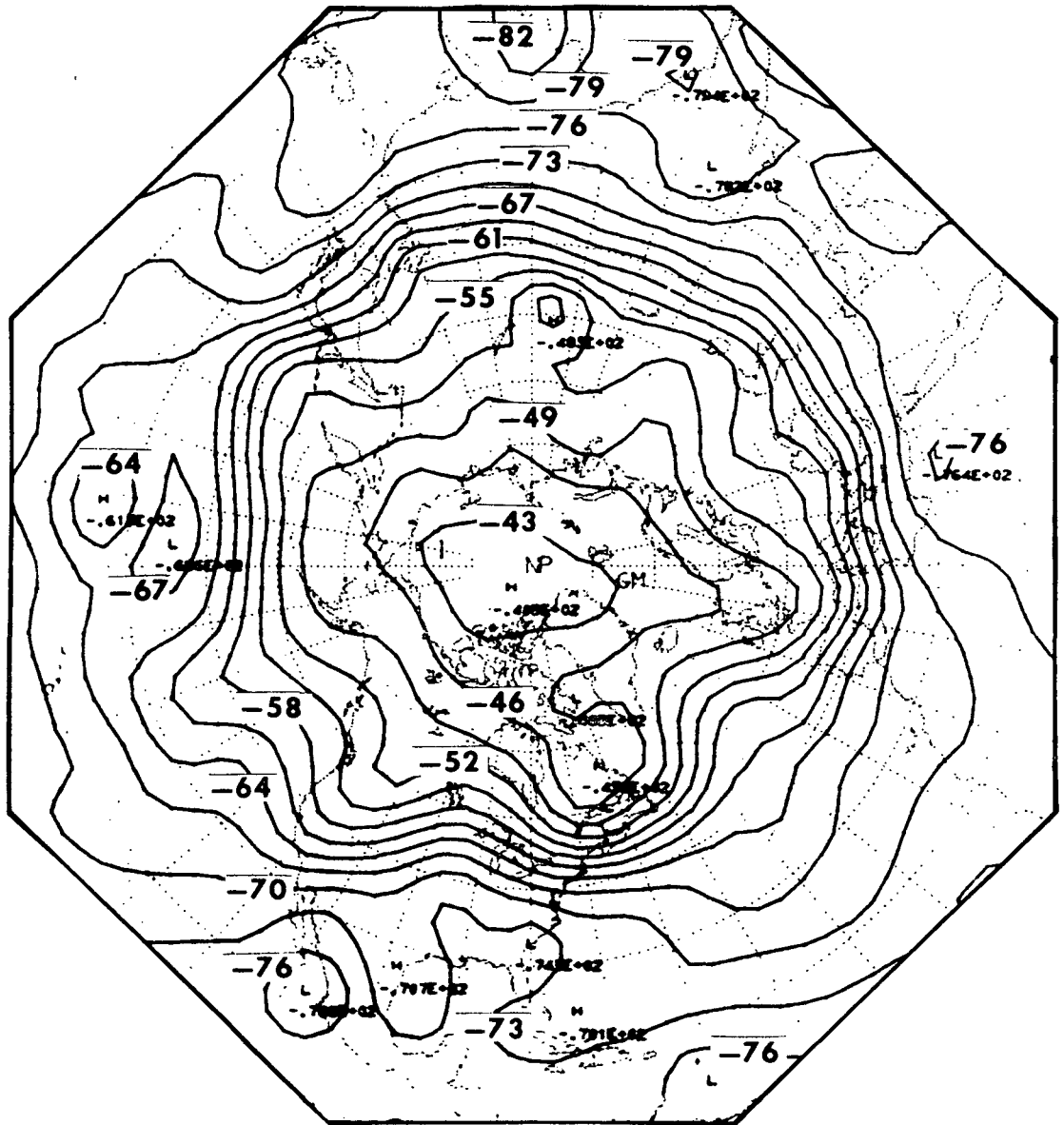


Fig. 3g - Northern Hemisphere Radiosonde temperatures (Degrees C.) at 100 mb. National Meteorological Centre (NMC) mapping. 8 July 1969. 0000 GMT.

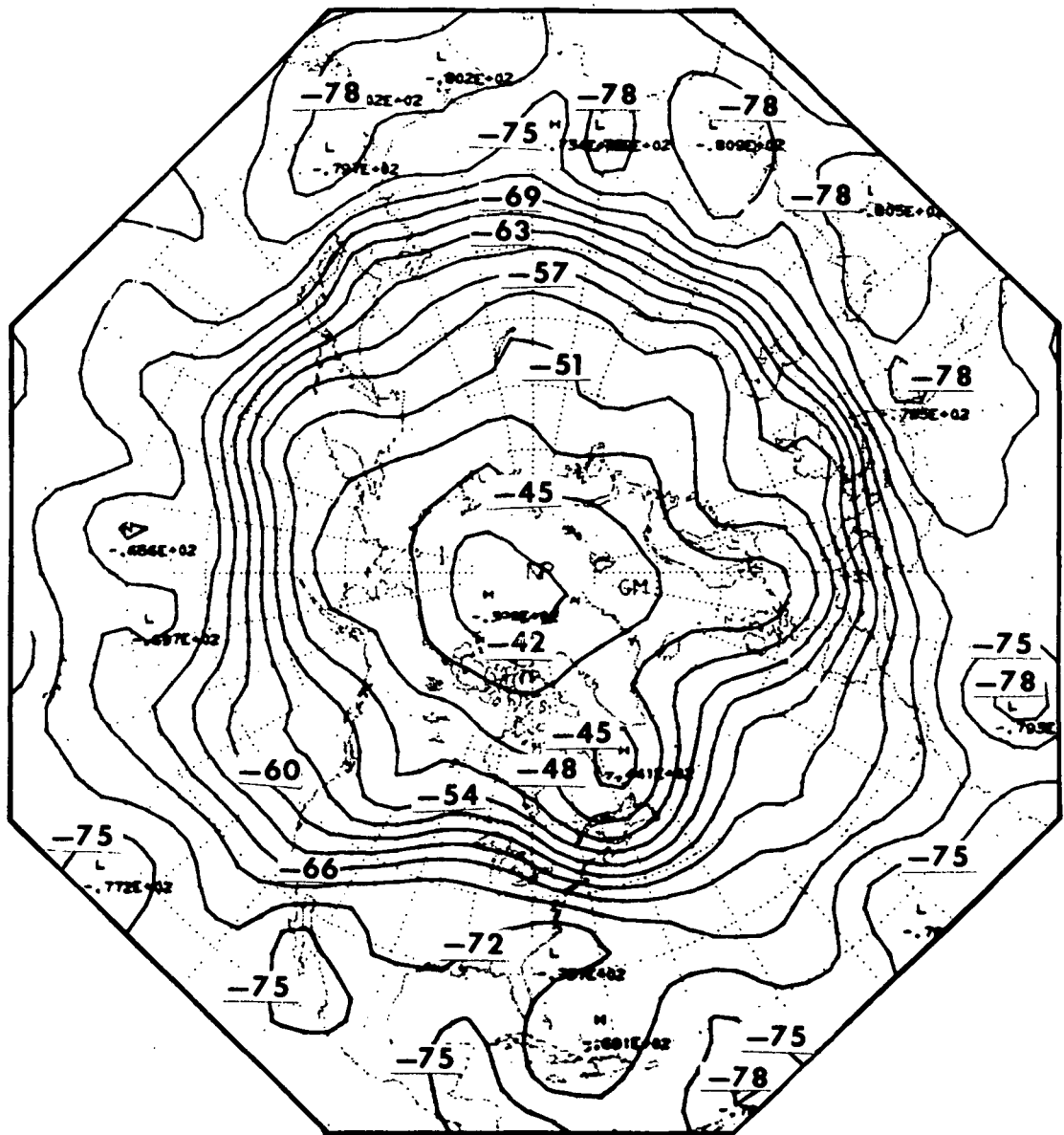


Fig. 3h - Northern Hemisphere Radiosonde temperatures (Degrees C.) at 100 mb. National Meteorological Center (NMC) mapping. 8 July 1969. 1200 GMT.

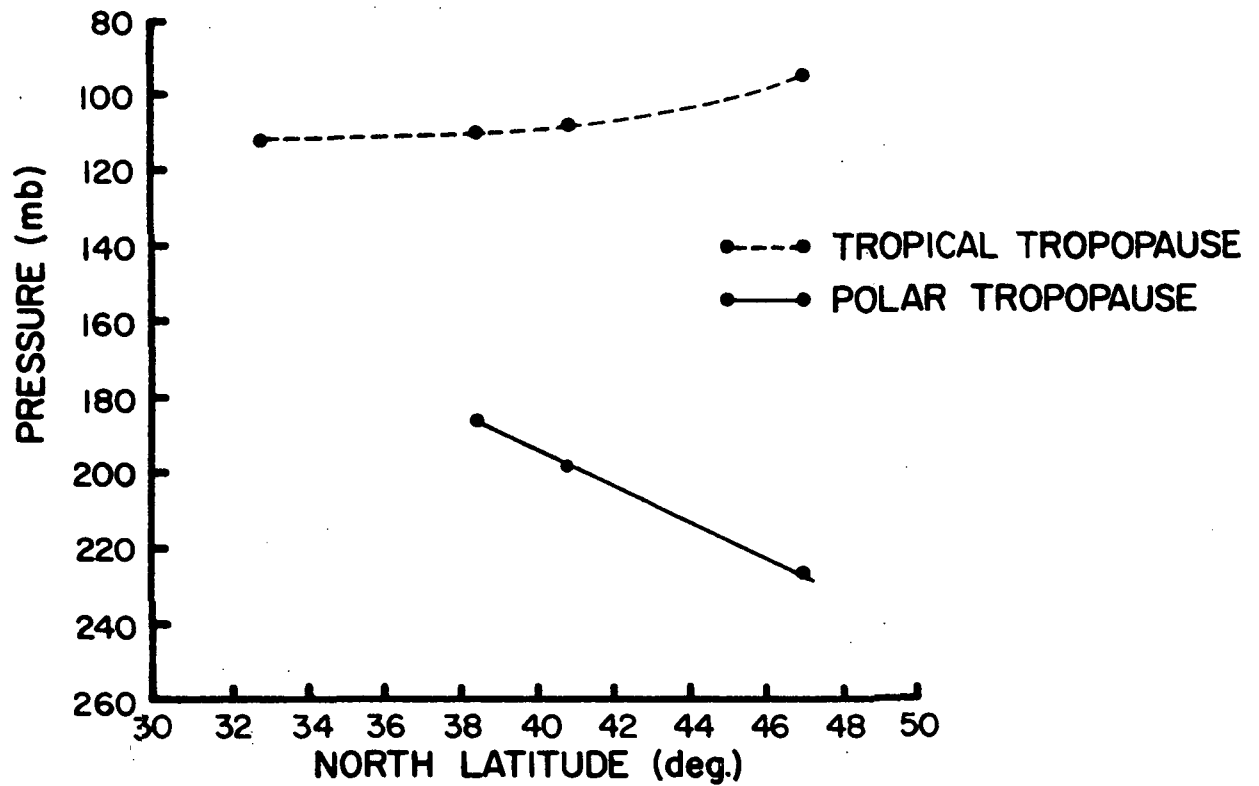


Fig. 3i - Mean July 1969 tropopauses along North American coastal regions. A tertiary region of stability exists at about the 140 mb level at most latitudes considered here.

methods for inverting the radiative transfer equation to detect temperature inversion in the upper atmosphere. Smith et al., (1970) discuss the problem; sec. 2.3 includes a suggested method of improvement in the tropopause region. The tropical tropopause which extends into very high latitudes during the summer (Fig. 3i) causes some of the deviations of the derived temperatures from the NMC temperatures.

NMC temperature distributions indicate very weak temperature gradients over the oceans. Satellite observations also indicate such gradients over oceans, but the differences between the oceans and the continents are not as large as in the case of the NMC distributions. These discrepancies are probably due to the very meager radiosonde data available in oceanic regions. Thus, IRIS-derived temperatures show greater zonal symmetry than the NMC data.

2.22 Special comparison of results with 30 mb radiosonde data

Figure 2f shows that at the 30 mb level the North American radiosonde temperatures are relatively warmer compared to the IRIS-derived temperatures whereas the Eurasian data are randomly distributed about the one-to-one correspondence line. (See also Table 2: The r.m.s. error for the 30 mb level temperatures is much smaller for the Eurasian data compared to the combined Eurasian-North American data.) This could be due to a natural diurnal temperature variation or a larger radiational error of the instrument used in North America compared to that of the Eurasian instrument. The former explanation is difficult to maintain in view of the fact that the Asian stations, which have made the observations at about the same local time as the North American stations, do not indicate such large systematic departures from the IRIS-derived temperatures.

One way to check any such large radiational errors would be to compare the radiosonde observations made at 0000 GMT and 1200 GMT along the two coastal regions of the North American Continent where the Local Standard Time (LST) for the above observational hours are significantly different. These LST equivalences are given in Table 3, after making an allowance of 2 hours for the ascent of the balloon to the 30 mb level. Table 4 contains the solar elevation angles in July at different latitudes along these coasts an hour after the release of the balloon; the radiational error generally accumulates after this time in the presence of sun because the balloon is in the stratosphere exposed to high insolation is not well ventilated. We will be concerned only with the latitude band 30-50N. From Tables 3 and 4 it is seen that the observations numbered 1 and 4 in Table 3 are made under low solar elevations and those numbered 2 and 3 under high solar elevations.

The mean temperatures for July 1969 at 30 mb at 4 east coast and 4 west coast stations for 0000 GMT and 1200 GMT were calculated and are presented in Fig. 4a. By averaging data for an entire month we hope to have eliminated all the diurnal temperature variation due to changes of synoptic situations. In Fig. 4a all observed values are consistent with the fitted profiles except Pittsburgh at 0000 GMT. It is readily inferred from the diagram that the daily mean temperatures. (in July 1969 at 30 mb) are very nearly the same in the two coastal areas.

Except for some small deviations the observations made under low solar elevations coincide in Fig. 4a and the observations made under

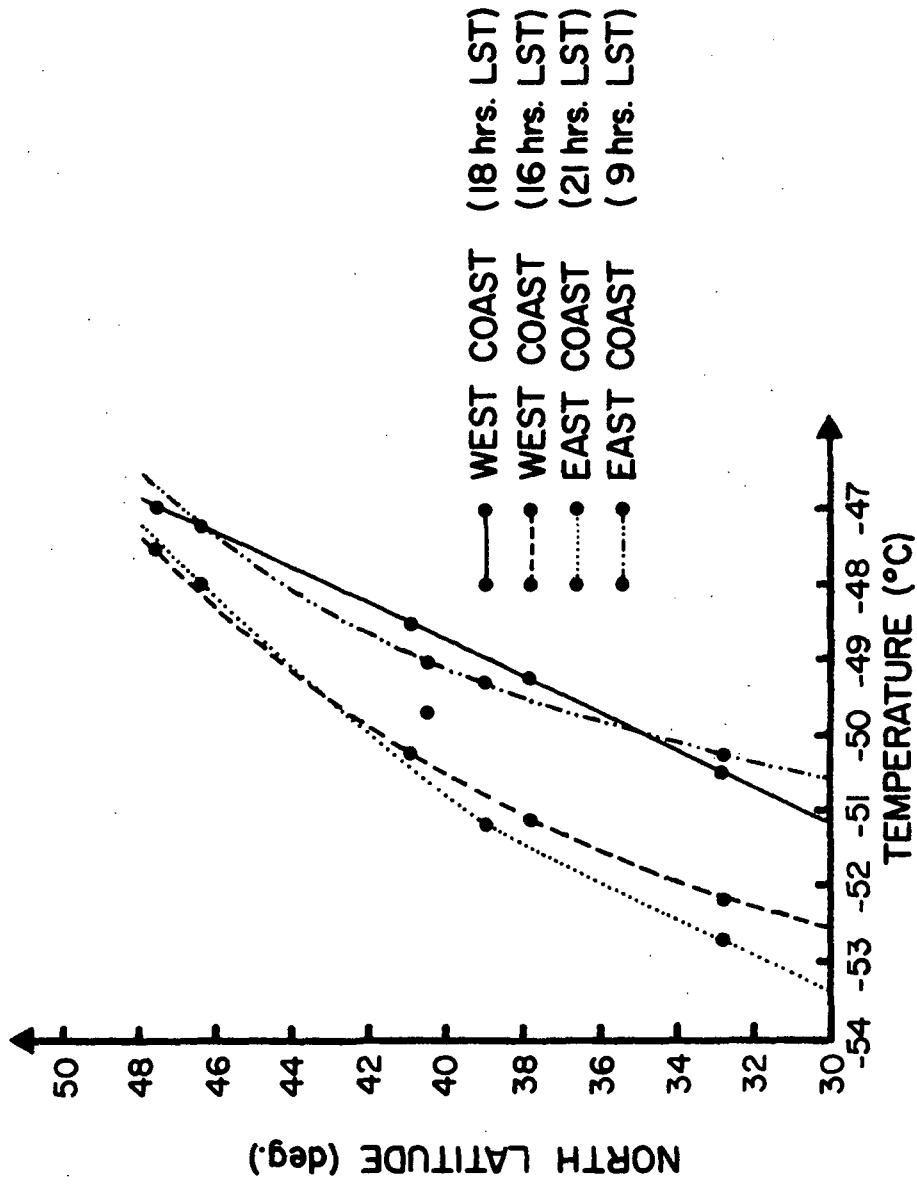


Fig. 4a - Mean July 1969 temperatures (Degrees C.) at 0000 GMT and 1200 GMT along North American coastal regions.

TABLE 3

Approximate local standard time (LST) for the 30 mb radiosonde observations in North American continental coastal areas between 30-50N. Ascent to this level assumed to take place in 2 hours. Arbitrary observation numbers are given in parentheses.

GMT	LST HOURS	
	East Coast	West Coast
0000	2100 (1)	1800 (2)
1200	0900 (3)	0600 (4)

TABLE 4

July solar elevation (to the nearest full degree) for 0000 GMT and 1200 GMT radiosonde observations an hour after the release of balloons at the Local Standard Time (LST) given. Arbitrary observation numbers written in parantheses. W.C. - West coast of North America. E.C. - East coast of North America. Data from Smithsonian Meteorological Tables (R.J. List, editor).

Latitude Degrees North	0000		1200		GMT LST
	E.C.	W.C.	E.C.	W.C.	
	2000 (1)	1700 (2)	0800 (3)	0500 (4)	
50	0	27	36	8	
45	0	26	36	6	
40	0	25	36	3	
35	0	24	36	1	
30	0	23	36	0	

NOTE: Refraction of solar radiation would advance sunrise and delay sunset. This factor has not been taken into account in the above calculations. Because of this factor more radiation would fall on the radiosonde at 2000 LST and 0500 LST than is suggested by its solar elevation angles given above (see Mitra, 1951).

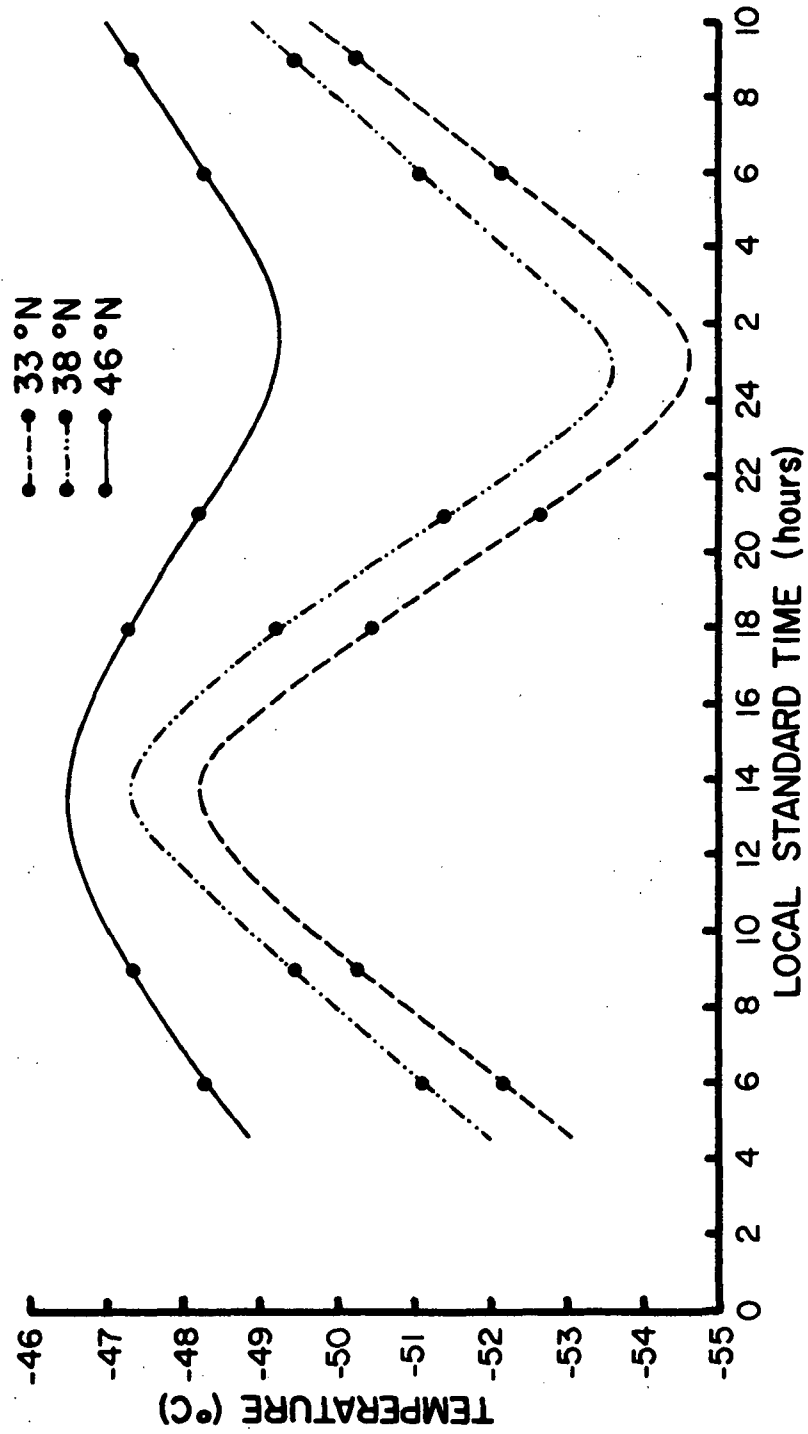


Fig. 4b - Apparent diurnal variation of temperature (Degrees C.) at 30 mb at different latitudes along North American coastal regions in July 1969 as deduced from Fig. 4a.

high solar elevations coincide also. The latter are some 2C warmer than the former south of 40N and gradually decrease with latitude north of that latitude.

Treating the two coasts as a single meridional sector in view of the invariance of the daily mean temperature mentioned above the apparent diurnal variation of temperature at 30 mb as obtained from the radiosonde data of Figure 4a are plotted as a time-series in Figure 4b. It is seen from this diagram that the diurnal maxima and minima must occur at 1400 LST and 0100 LST respectively at all latitudes between 30N and 50N (to a reasonable degree of approximation). This periodicity is extremely odd, both the increase in temperature from 0100 LST to sunrise and the decrease from 1400 LST onwards being quite inexplicable. The amplitude of the apparent diurnal variation is in excess of 6C in the latitude band 33-38N and decreases to some 2.8C at 46N.

The following remarks by Craig (1951) concerning the heating rates in the ozone layer and below are of interest: "Karandikar's (1946) computations show that the heating produced by infrared absorption of solar energy can be safely neglected above 30 km in comparison with the heating produced by ultraviolet absorption of ozone. Below 30 km, on the other hand, the former process becomes dominant, water vapor playing the most important role. . . The absolute values of the rates of heating and cooling are relatively low, of the order of magnitude of 0.1C per three hours below 30 km and of 1C per three hours at 35-50 km." The radiosonde-given temperature change at the 30 mb (~ 25 km) level, as seen in Fig. 4b, exceeds even the latter value in the 33-38N latitude band.

Finger and McInturff (1968), using North American radiosonde data for the period Jan. 1964 to June 1966 at the 30 mb level and above, have evaluated the diurnal temperature range $R(T)$ considering stations which make both 0000 GMT and 1200 GMT observations either in the sun or in darkness. They arrive at these conclusions: The computed diurnal temperature range $R(T)$ shows a definite increase with altitude in summer, $R(T)$ at 10 mb being double that at 30 mb and that at 5 mb being 2.5 times the $R(T)$ at 10 mb. In winter the change with height is not so well-defined. At 30 mb $R(T)$ is less than 0.5C in summer and generally decreases with latitude (Fig. 4c). The true diurnal change most probably peaks near sunset and has a minimum near sunrise. These conclusions are in very good agreement with Craig's (1951) remarks above.

Fritz (1970) states that the diurnal variation of stratospheric temperature (integrated in the vertical) is small and is of the order of $0.5 \text{ erg cm}^{-1} \text{ sr}^{-1} \text{ s}^{-1}$. The temperature equivalent for this quantity is approximately 0.5C for a black-body. The integration referred to here is over the altitude range in which $\nu = 669 \text{ cm}^{-1}$ has a non-zero weighting function value. Our own studies using $\nu = 675 \text{ cm}^{-1}$ which has maximum weighting in slightly lower stratospheric levels (Fig. 1) show that there is very little diurnal variation of radiances in this wave-number. As this is probably also true of individual levels above the 100 mb level the differences between the 0000 GMT and 1200 GMT observations seen in Fig. 4a are most probably radiational errors in the sonde.

Figure 5 also lends support to this contention. In this diagram the 1200 GMT east and west coast temperatures at 30 mb are differentiated and plotted against IRIS-derived temperatures which are a good approximation to the daily mean value since the observations are made at local

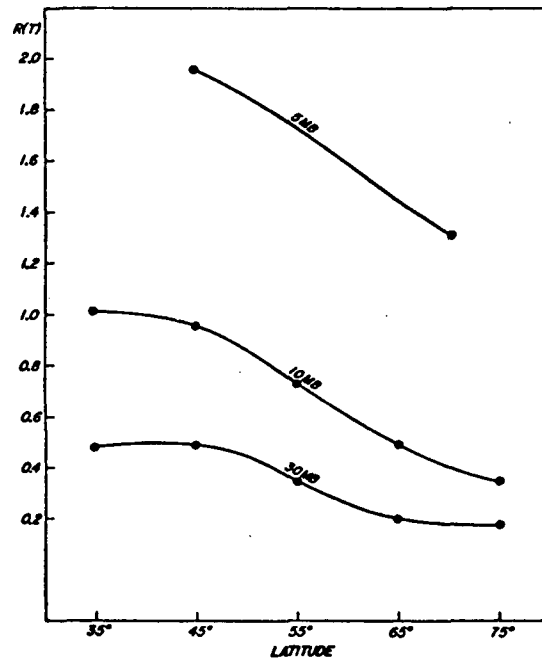


Fig. 4c - Summertime variation of diurnal temperature range $R(T)$ in degrees C. for 30, 10 and 5 mb as a function of latitude. (From Finger and McInturff, 1968).

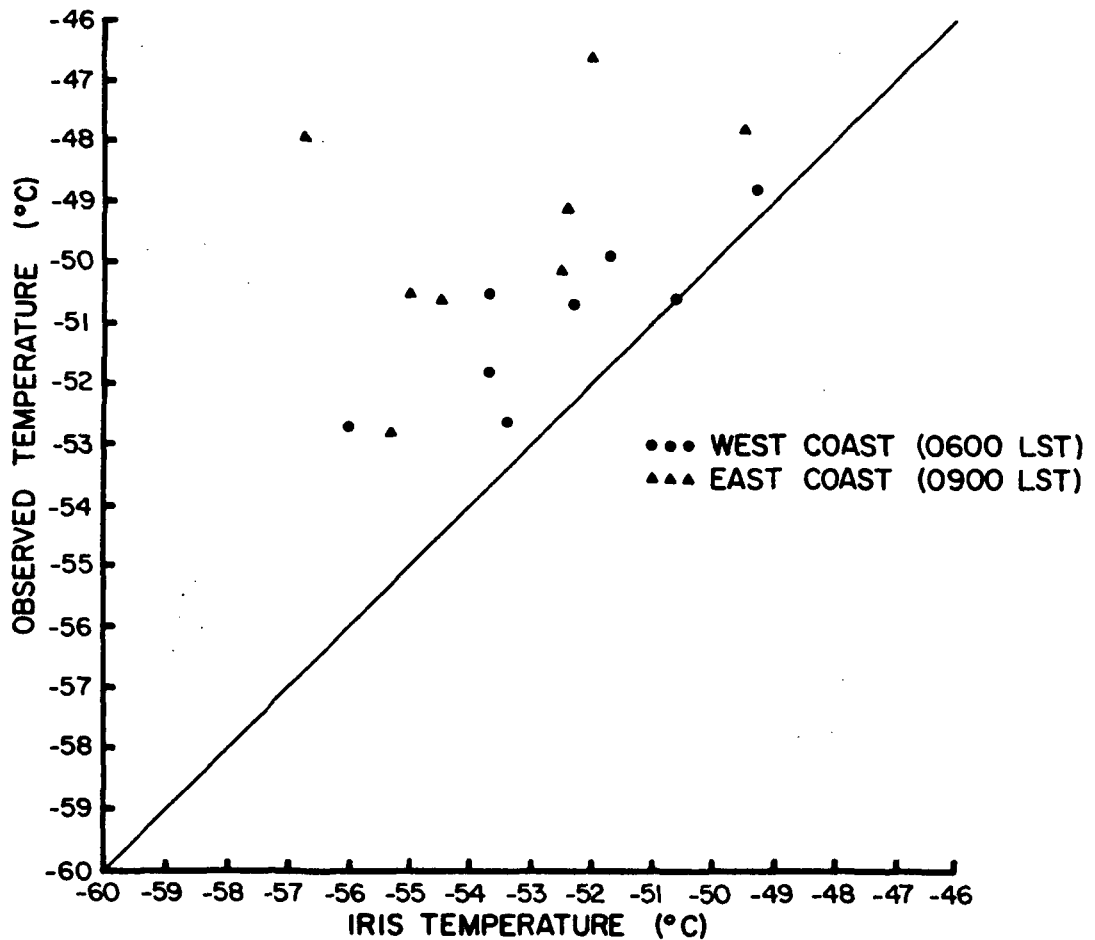


Fig. 5 - North American West Coast and East Coast radiosonde temperatures at 1200 GMT compared to IRIS-derived temperatures. Data for 3, 8 July 1969. Local Standard Time (LST) given is adjusted by 2 hours for balloon ascent to the 30 mb level.

noon and midnight. It is seen that the east coast soundings (at 0900 LST) are generally warmer than the west coast soundings (at 0600 LST) even on individual days.

If these rather large apparent diurnal variations are adjusted, the IRIS-derived and radiosonde temperatures at the 30 mb level would agree very well over all the regions where comparisons have been made.

2.23 Additional comparison of temperature-radiance relation for cloud-contaminated and "cloudless" data

Two sets of "simultaneous" IRIS radiance and NMC temperatures were compiled. One set of data consisted of data from which cloud-contaminated points had been eliminated by a technique to be described. The other set retained data from points affected by clouds.

The method of removing cloud-affected data is as follows. For each day of data (there were three days of data in each set) frequency distributions of radiance in the 735 cm^{-1} channel, $N(735)$, are made for each ten degrees of latitude from 20°N to 80°N . The median of each of the frequency distributions is calculated. From comparisons of the spatial variations of $N(735)$ and video cloud information, a criterion for elimination of cloud-affected data was subjectively determined. The criterion eliminates data points where $N(735)$ is less than $\overline{N(735)} - 8.0$, where $\overline{N(735)}$ is the median for the latitude band of the data. This criterion was applied for each of three days of data (3, 4, 8 July 1969) to obtain the "cloudless" data set. The data were averaged over 5 points. The other set, the "with-cloud" set, was obtained by setting the cloud elimination criterion low enough so that cloud-affected data is accepted into the data set.

The temperature-radiance correlation matrix for the "cloud-free" set and the cloud-affected data set are given in Table 5. The "cloud-free" correlations are the upper ones in each box; the "cloud-affected" correlations are the lower ones. The differences between the "cloud-free" and "cloud-affected" correlations are less than 0.01 for channels 665 cm^{-1} to 695 cm^{-1} . For channels 705 cm^{-1} to 900 cm^{-1} the differences vary from 0.03 to 0.45. This relation is to be expected from the distribution of the individual channel weighting functions. The channels with large differences have weighting functions with peaks in the middle and low troposphere. Those are the channels that are most affected by the presence of clouds. The "cloud-affected" set had 567 data points, the "cloud-free" set, 469. Thus about twenty percent of the data were eliminated by judging it cloud-contaminated.

The correlation matrix for the "cloud-free" data displays the expected high positive correlation between low wave number radiance and high altitude temperature (e.g., $N(675)$ and 100 mb temperature) and between high wave number radiance and low altitude temperature (e.g., $N(725)$ and 850 mb temperature). The data set included measurements from 20°N to 80°N . Therefore, there is a strong negative correlation between tropospheric and stratospheric temperature. This is reason for the large negative correlations in the bottom-left and upper-right corners of the correlation matrix.

Regression equations for the two sets of data for temperatures at various pressure levels are given in Table 6. The fraction of the variance explained and the standard error are also given. A stepwise regression procedure was used with the selection of variables halted when the percent variance explained failed to increase by at least 1%.

Temperature vs. Radiance Correlation Matrix

Temperature at Pressure Levels		665	675	685	690	695	700	705	710	715	725	745	900
	100 mb	.971 .970	.975 .974	.974 .973	.969 .967	.950 .944	.804 .762	.019 .181	-.620 -.207	-.746 -.345	-.801 -.486	-.784 -.488	-.748 -.556
	150 mb	.943 .944	.947 .948	.950 .952	.955 .954	.950 .946	.838 .800	.099 .243	-.562 -.155	-.692 -.293	-.745 -.431	-.725 -.432	-.686 -.496
	200 mb	.730 .736	.731 .737	.738 .746	.764 .769	.792 .792	.775 .730	.245 .272	-.348 -.085	-.510 -.226	-.579 -.356	-.563 -.357	-.533 -.408
	250 mb	-.528 -.534	-.531 -.534	-.524 -.528	-.490 -.494	-.433 -.441	-.230 -.257	.281 .042	.487 .180	.466 .206	.457 .263	.449 .266	.443 .319
	300 mb	-.870 -.868	-.879 -.878	-.879 -.878	-.864 -.863	-.839 -.838	-.652 -.649	.130 -.118	.654 .206	.728 .311	.741 .422	.716 .419	.669 .475
	400 mb	-.885 -.887	-.895 -.897	-.897 -.899	-.889 -.892	-.874 -.874	-.708 -.694	.084 -.136	.650 .215	.742 .333	.763 .452	.738 .449	.683 .499
	500 mb	-.889 -.894	-.900 -.904	-.902 -.907	-.900 -.903	-.887 -.887	-.730 -.704	.069 -.129	.655 .235	.761 .364	.786 .486	.760 .482	.701 .529
	700 mb	-.897 -.895	-.905 -.904	-.906 -.904	-.903 -.901	-.877 -.881	-.731 -.694	.074 -.109	.659 .255	.773 .386	.810 .518	.786 .514	.740 .571
	850 mb	-.864 -.857	-.870 -.864	-.869 -.863	-.868 -.862	-.851 -.840	-.712 -.668	.061 -.101	.625 .248	.750 .384	.803 .522	.784 .522	.754 .592

TEMPERATURE AND RADIANCE CORRELATION MATRIX FOR CLOUD FREE AND CLOUD CONTAMINATED DATA

Cloud Free	Cloud Affected
$T_{100} = -151.93 + 1.78 N_{675}$ Variance Explained = .950 Standard Error of Estimate = 2.44	$T_{100} = -151.53 + 1.78 N_{675}$ Variance Explained = .949 Standard Error of Estimate = 2.46
$T_{150} = -130.93 + 1.54 N_{690}$ VE = .911 SEE = 2.78	$T_{150} = -131.20 + 1.55 N_{690}$ VE = .911 SEE = 2.80
$T_{200} = -107.18 - 1.01 N_{675}$ VE = .675 SEE = 3.18	$T_{200} = -91.27 - 0.92 N_{675} + 1.54 N_{695}$ VE = .691 SEE = 3.08
$T_{250} = -69.47 - 1.54 N_{675} + 1.06 N_{695}$ $+ 1.06 N_{695} + 0.97 N_{700}$ VE = .506 SEE = 3.06	$T_{250} = -48.95 - 0.72 N_{675} - 0.90 N_{685}$ $+ 1.26 N_{700} - 0.38 N_{725} + 0.09 N_{900}$ VE = .508 SEE = 3.02
$T_{300} = -41.16 - 0.98 N_{685} + 1.07 N_{705}$ $+ 1.07 N_{705} - 0.12 N_{745}$ VE = .835 SEE = 2.26	$T_{300} = -14.59 - 1.21 N_{685} + 0.82 N_{700}$ $- 0.08 N_{745}$ VE = .802 SEE = 2.54
$T_{400} = -18.91 - 0.99 N_{685} + 0.78 N_{705}$ VE = .838 SEE = 2.68	$T_{400} = 10.85 - 1.02 N_{685} + 0.29 N_{705}$ VE = .820 SEE = 2.85
$T_{500} = -7.32 - 0.85 N_{685} + 0.60 N_{710}$ VE = .842 SEE = 2.62	$T_{500} = 20.81 - 1.01 N_{685} + 0.39 N_{705}$ VE = .836 SEE = 2.66
$T_{700} = 5.82 - 0.42 N_{685} - 1.00 N_{695}$ $+ 1.19 N_{705}$ VE = .862 SEE = 2.87	$T_{700} = 38.88 - 1.17 N_{685} + 0.42 N_{705}$ VE = .837 SEE = 3.07
$T_{850} = 33.98 - 0.94 N_{675} + 0.34 N_{725}$ VE = .786 SEE = 4.12	$T_{850} = 61.11 - 1.16 N_{675} + 0.15 N_{725}$ VE = .765 SEE = 4.24

TABLE 6

REGRESSION EQUATIONS FOR CLOUD FREE AND CLOUD AFFECTED DATA SETS

 T in $^{\circ}\text{C}$, N in erg/

The most striking feature of Table 6 is the similarity between the cloud-free and cloud-affected regression parameters. There is hardly any difference in the variance explained between the two data sets and in some cases (200 and 250 mb) the variance explained is actually higher for the cloud contaminated set than for the cloud-free set. There is a significant difference, however, in the regression coefficients in the equation for 300 mb and below. In these equations, the coefficients of radiances such as $N(705)$, $N(710)$ etc. are larger in the cloud-free set than in the cloud-affected set. For example, for T_{400} the size of the coefficient for $N(705)$ is greater in the cloud free set than in the cloud affected set. This difference is because of the effect of cloud on $N(705)$.

Both data sets contained data from 20-80°N. The greatest contribution to the total variance of the temperature fields is the north-south variation. The variability of temperature around latitude circles is much smaller than the north-south variation. This leads to the high explanation of variance even for pressure levels in the low and mid-troposphere by equations containing radiances with weighting function peaks in the stratosphere (e.g., $N(675)$ in equation for T_{850}). This is because of the strong negative correlation between troposphere and stratospheric temperatures. Thus the regression equations in Table 6 are probably of limited use, except perhaps for the top three levels. Below that the equations are explaining mostly the north-south temperature gradient and will not accurately pick out longitudinal, synoptic variations in the troposphere.

2.3 Determination of Tropopause Pressures and Tropopause Temperatures from IRIS Data

2.31 Description of method

In general the tropopause slopes from high altitude and low pressures over the tropics to lower elevations and higher pressures in temperate and polar latitudes. The temperature of the tropopause also varies with latitudes being cold in low latitudes and warmer in higher latitudes. Tropopause pressure and temperature also vary in relation to synoptic features with low and warm tropopause associated with upper troposphere troughs and cold and high tropopause associated with ridges. The IRIS radiances are related to atmospheric temperatures through the radiative transfer equation. IRIS channels with low wave numbers, for example with $\nu = 667 \text{ cm}^{-1}$ or $\nu = 675 \text{ cm}^{-1}$, have a peak in their weighting functions ($d\tau/d \ln p$) in the low stratosphere while channels with higher wave numbers have weighting function peaks lower in the atmosphere. Thus, the radiances in the channels of the IRIS experiment are related to a weighted mean Planck function with different channels representing different overlapping layers. Because the Planck function is a function of temperature the weighted mean Planck function is related to the temperature in the layer.

Figure 6 shows two plots of IRIS radiance against channel number with lower channel numbers associated with higher wave numbers. Channels with lower wave numbers which have weighting function peaks in the stratosphere are higher on the ordinate than channels with weighting function peaks in the troposphere. The plots are for the same orbit on 3 July 1969 for latitudes 24°N and 62°N and are for cloud-free data. The two profiles are typical for low and high latitude radiance profiles. There is

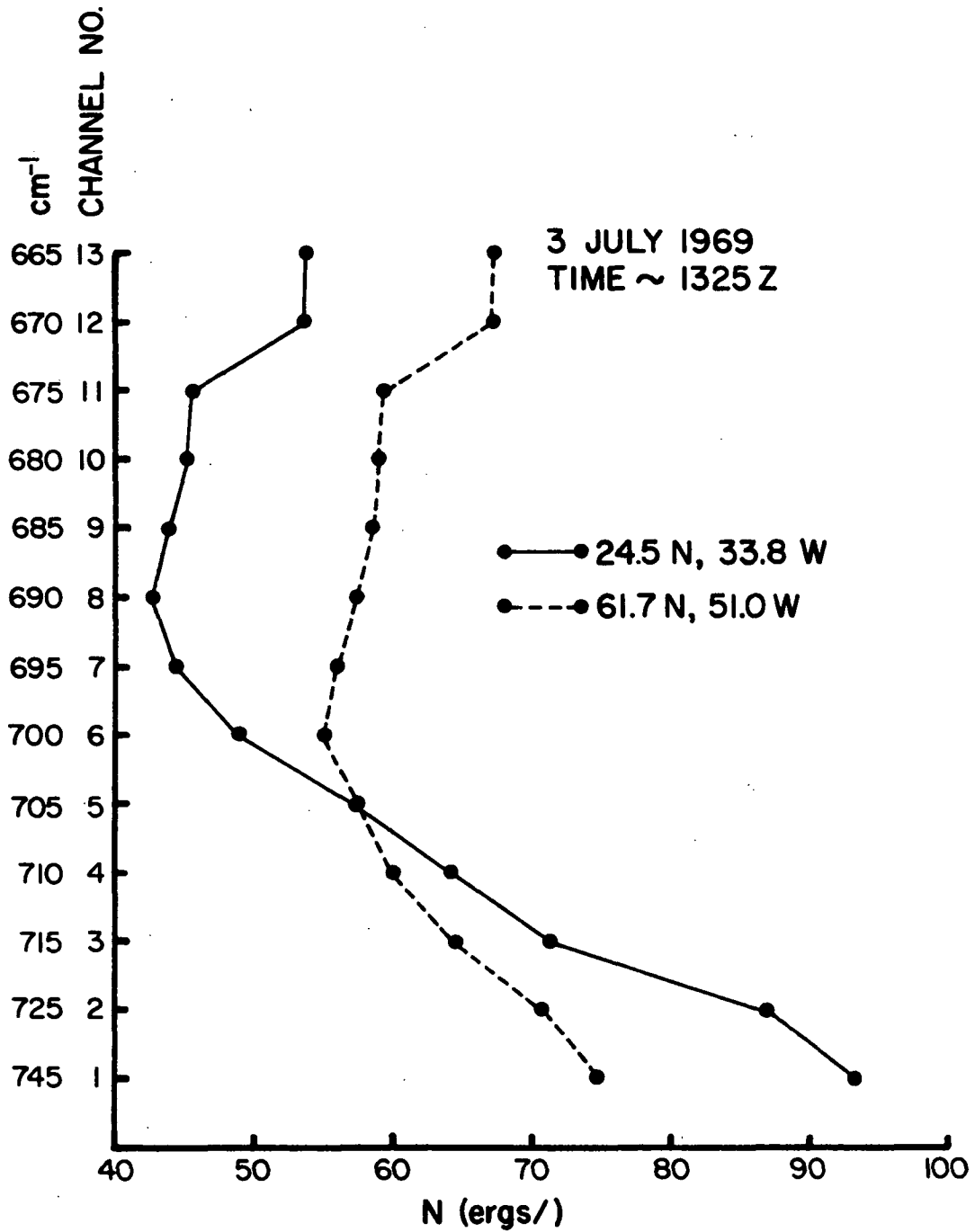


Fig. 6 - IRIS Radiance Profiles

a substantial difference between the two profiles. The low latitude profile (24.5°N) has higher radiances in channels 1 through 4 and lower radiances in channels 6 through 13. This cross-over of the two radiance profiles corresponds to a warm troposphere and cold stratosphere in low latitudes and a cold troposphere and warm stratosphere in high latitudes. The two radiance profiles also display a difference in the location of the point where there is a marked change in slope of the profile. On the low latitude profile the point of slope change is at channel 8; on the high latitude profile the slope change is at channel 6. The point at which the slope changes in the radiance profile is associated with the height of the tropopause. The tropopause is lower at 61.7°N than at 24.5°N and this is reflected in the lower position of the slope change at 24.5°N in Fig. 6. This example shows, at least in a general sense, that the position on the radiance profile of the change in slope is related to the tropopause position. The technique described in this section objectively determines the point in the radiance profile which is associated with the tropopause.

The radiance profiles to be used in the tropopause computations, such as the profiles in Fig. 6, are determined by eliminating data points with unreasonable radiances, eliminating data determined to be contaminated with clouds (using the 735 cm^{-1} channel) and averaging over five data points along the orbit. To the resulting radiance profiles a fifth degree curve is fitted by a least squares technique to channels 5 through 10 (705 cm^{-1} through 680 cm^{-1}) to give an equation of the form

$$N = a_0 + a_1C + a_2C^2 + \dots + a_5C^5 \quad (6)$$

where N is the radiance and C is the channel number which varies in this case from 5 to 10.

To pick off the point in the radiance profile which is associated with the tropopause an indicator is needed of where in the profile the change in slope is greatest. After some subjective experimentation an indicator K defined by equation (7) was determined to do a good job in finding objectively the point the author selected subjectively.

$$K = \frac{\frac{d^2N}{dC^2}}{(1 + \left|\frac{dN}{dC}\right|^2)^{\frac{1}{2}}} \quad (7)$$

The tropopause channel (C_T), in other words the point along the C axis of the profile which is associated with the tropopause, is defined as the point where K is a maximum. The tropopause radiance (N_T) is defined as the radiance N in equation (6) when $C = C_T$.

A computer program has been written to determine C_T and N_T from the IRIS data. The output of the program in addition to C_T and N_T are the position and time of the observation and the associated radiance profile.

2.32 Comparison of satellite-derived parameters with tropopause pressures and temperatures obtained from radiosondes

The parameters C_T and N_T obtained from the IRIS data should be in some way related to tropopause pressure and temperature respectively. The two parameters should represent features of a mean tropopause, i.e. a tropopause corresponding to a temperature profile smoothed with respect to height or pressure. The reason that the C_T and N_T obtained from the IRIS data should be related to a tropopause of a smoothed temperature profile is that the radiances themselves represent a smoothed structure.

However, to objectively compare C_T and N_T with some actual observations of the tropopause, a set of near-simultaneous observations of C_T , N_T and tropopause pressure and temperature were collected. The set of observations covers a 7 day period from 3 July to 9 July 1969. The data set was confined to North America where tropopause pressure and temperature is given as a significant level report in the northern hemisphere data tabulations. The radiosonde observations used had to be within 180 nautical miles and six hours of the satellite position and time. Stations with double tropopauses were eliminated. Figure (7) shows a scatter diagram of tropopause pressure versus tropopause channel C_T . There is a large scatter, but an apparent relation between the two variables with low C_T associated with high tropopause pressure and high C_T with low tropopause pressure. The scatter is obviously not gaussian but skewed so that the long tail of the scatter is towards high pressure. This type of skewed scatter is evidenced by the points falling at higher pressure than the bulk of the points. These points represent reported tropopauses on the radiosonde data that are probably lower than the smoother profile tropopause that the parameter C_T represents. A least square regression between tropopause pressure (P_T) and C_T is not applicable because of the non-gaussian scatter. For this reason the data set was divided into seven groups according to C_T so that each group contained approximately the same number of data points. For each group a median tropopause pressure was calculated and plotted against the mean C_T of the group. This plot is given in Fig. (8) with a curve fitted to the seven medians. From the fitted curve C_T of 8.0 represents a tropopause pressure of about 115 mb, C_T equal to 5.6 represents a P_T of about 280 mb.

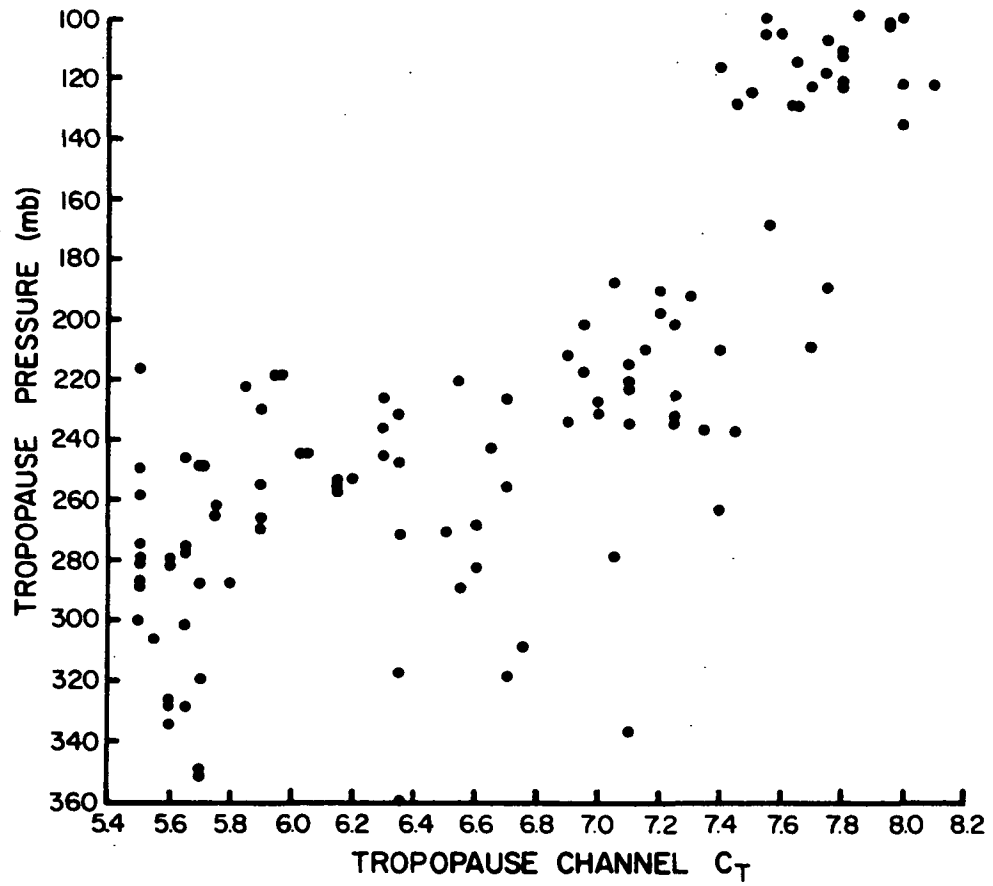


Fig. 7 - Scatter Diagram of Tropopause Pressure and Tropopause Channel

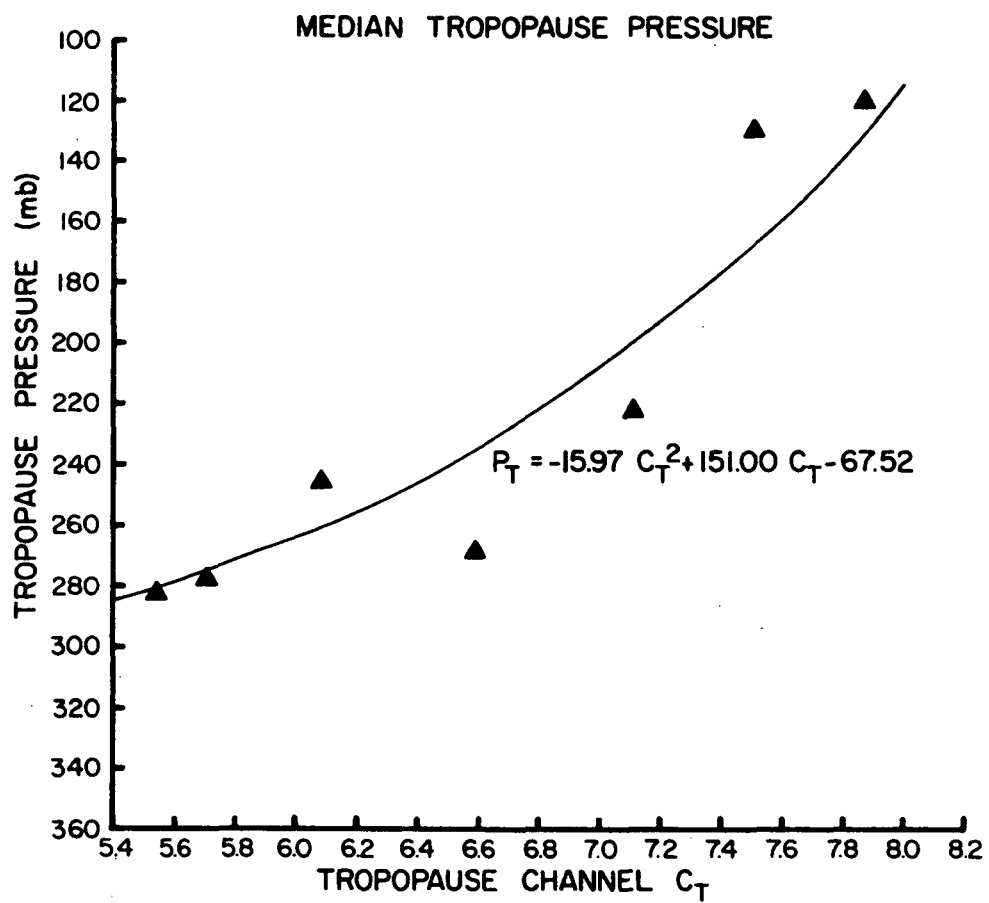


Fig. 8 - Group Medians of Tropopause Pressure versus Group Means of Tropopause Channel

Figure (9) shows the scatter diagram between tropopause temperature (T_T) and tropopause radiance, N_T . Again the data is separated into seven groups according to N_T and medians in each group are calculated and plotted against mean tropopause radiance in Fig. (10). A linear fit to the plotted points is also given. An N_T of 59 ergs/ is related to a tropopause temperature of -46°C , while an N_T equal to 42 ergs/ is about equal to a T_T of -70°C .

2.33 Comparison of analyses of tropopause channel and tropopause radiance with synoptic conditions at 200 mb

Figures (11) and (12) show analyses of C_T and N_T respectively for 3 July 1969. The C_T analysis (Fig. 11) displays, in general, large C_T over the tropics, low C_T in higher latitudes. On the N_T analysis (Fig. 12), which corresponds directly to tropopause temperature (T_T), low values are seen in low latitudes corresponding to cold tropopause temperatures, and high N_T values in higher latitudes corresponding to warmer tropopause temperatures. Also evident from the diagrams are a number of synoptic features which appear on both charts. Low values of C_T which correspond to low tropopauses are related to high values of N_T and therefore warm tropopause temperatures. The low and warm tropopause is a feature of troughs while high and relatively cold tropopauses are associated with ridges. In addition, tight horizontal gradients of tropopause pressure or tropopause temperature will be related to regions of a sharp sloping tropopause which in turn is associated with positions of jet streams.

The troughs, ridges and jet streams that are associated with the features on Figures (11) and (12) can be seen in Fig. (13), an analysis

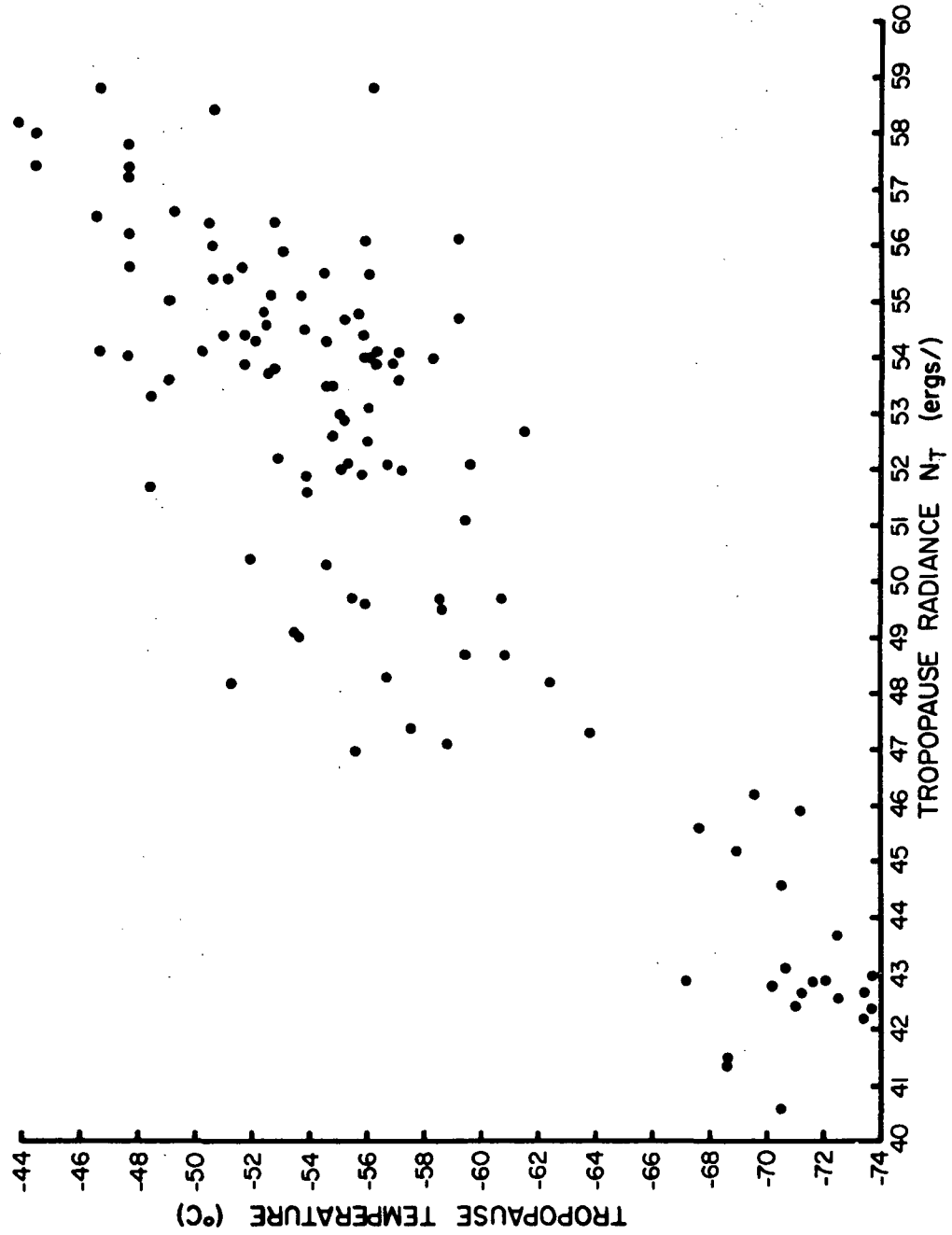


Fig. 9 - Scatter Diagram of Tropopause Temperature and Tropopause Radiance

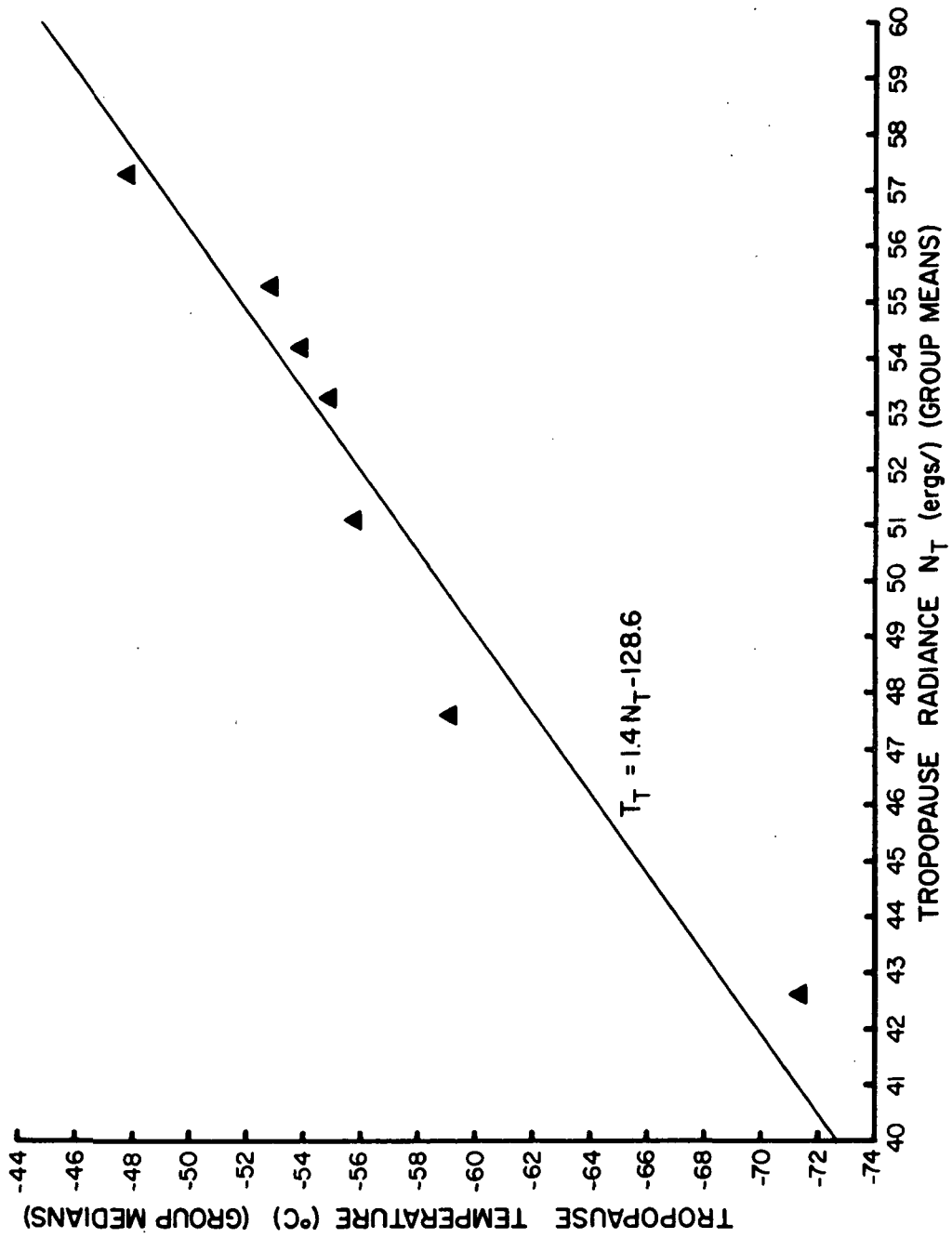


Fig. 10 - Group Medians of Tropopause Temperature versus Group Means of Tropopause Radiance

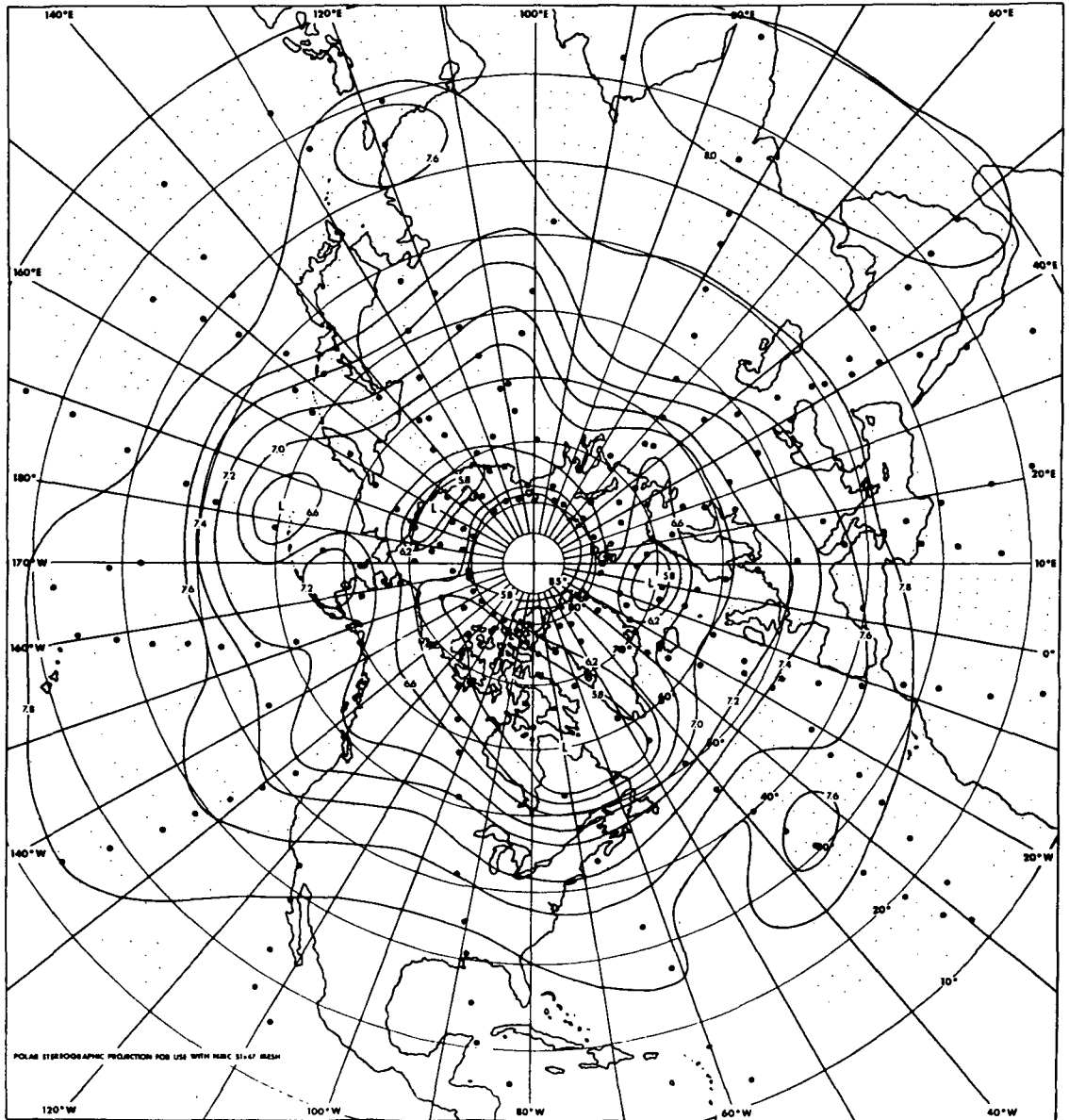


Fig. 11 - Northern Hemisphere Analysis of Tropopause Channel C_T for
3 July 1969

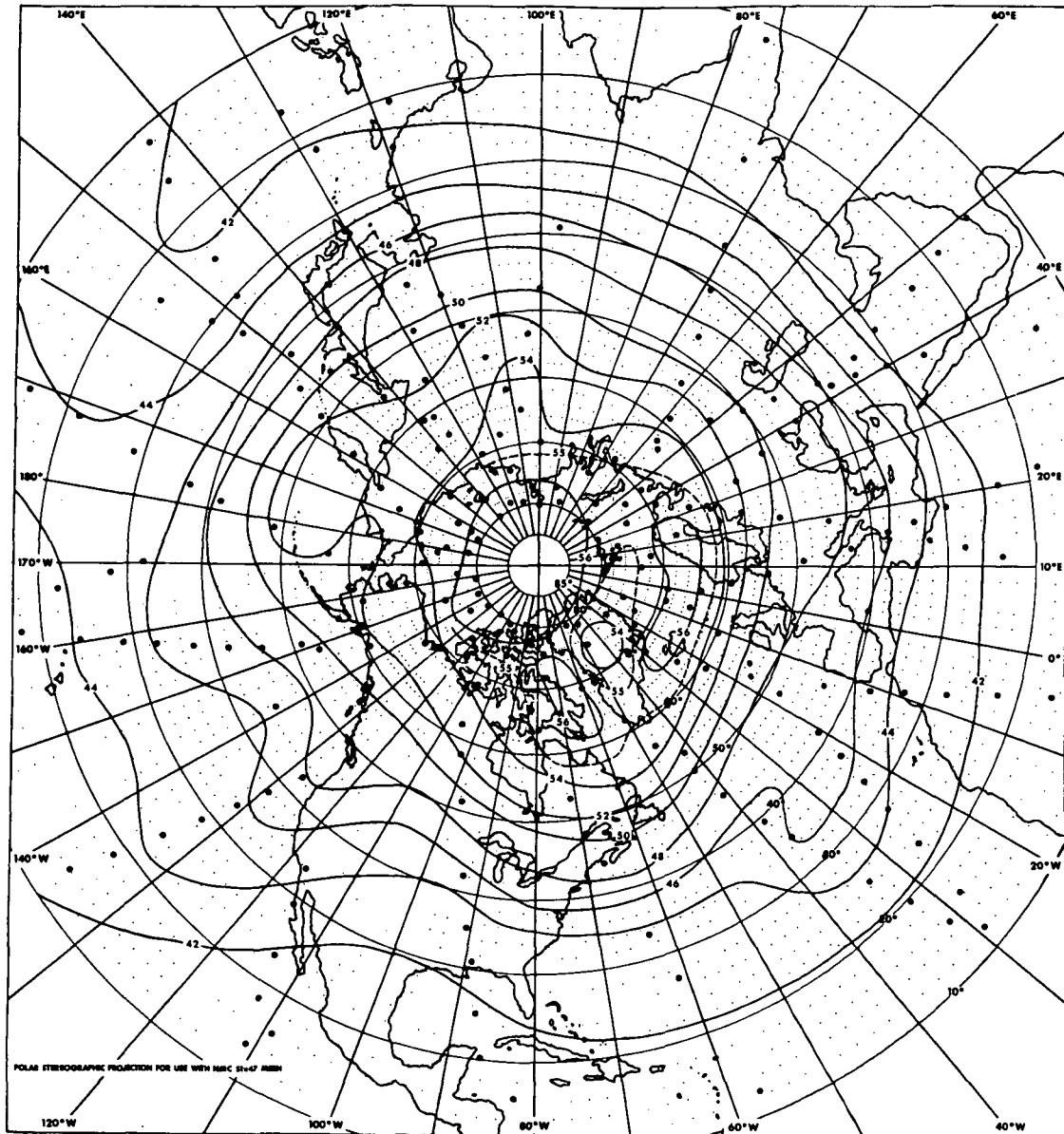


Fig. 12 - Northern Hemisphere Analysis of Tropopause Radiance N_T for 3 July 1969. Units are ergs/.

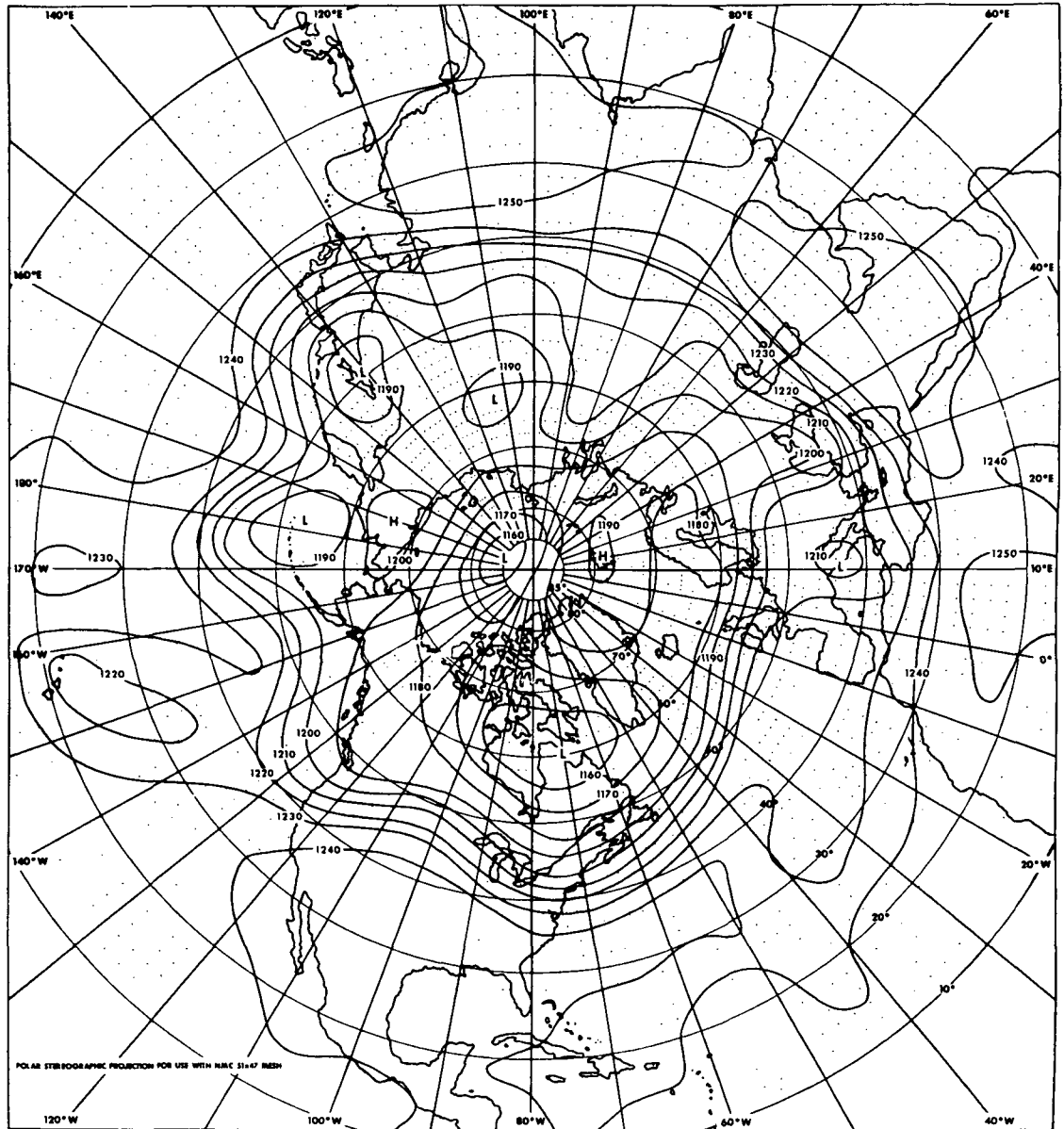


Fig. 13 - Northern Hemisphere Analysis of 200 mb Geopotential Height Field from NMC Grid Data for 3 July 1969. Units are tens of meters.

of the 200 mb height field for 1200Z 3 July 1969, from NMC grid data. Comparison of the N_T analysis (Fig. 12) with the 200 mb analysis shows a good correspondence of features between the two charts. Troughs on the 200 mb chart coincide with high radiance values associated with warm and low tropopauses. This association is evident, for example, in the trough centered about at 60°N , 70°W and its relatively weak extension eastward over southern Greenland and across the Scandinavian peninsula as seen in Fig. (13). The trough and its eastward extension is associated with high N_T in Fig. (12).

The position of the jet streams is also marked on the N_T analysis (Fig. 12). Over North America there is a confluence of N_T lines with a relatively tight gradient eastward from about 110°W . The area of tight gradient narrows over the western Atlantic and extends eastward across the North Sea and the Baltic Sea in northern Europe. This position of the tight N_T gradient coincides very well with the jet stream position as given by the 200 mb chart in Fig. (13). Tight N_T gradients over the east coast of Asia and the western Pacific Ocean and over the eastern Mediterranean Sea and eastward are also associated with jet streams.

Thus the tropopause channel C_T , which is indicative of the tropopause pressure, and the tropopause radiance N_T , which is associated with tropopause temperature show good agreement with synoptic features at approximate tropopause level.

For the same day (3 July 1969) maps of C_T and N_T were plotted and analyzed for the Southern Hemisphere with mixed results. In low latitudes, up to about 45°S , the analysis looks reasonable. At higher latitudes it becomes more difficult for the technique to determine the

tropopause information from the IRIS data. This difficulty is due to the presence of the stratospheric polar vortex in the higher latitudes. The cold stratospheric temperatures associated with the vortex reduce the radiance in channels with a significant contribution from the stratosphere. This leads to a reduction of the curvature of the radiance profile and an increase in the difficulty of picking the point in the profile to represent the tropopause. Even with this drawback positions of troughs can be deduced and seem to compare well with satellite cloud observations. Further work will be done on this high-latitude, winter hemisphere problem in the next few months.

Figure (14) gives the total ozone map for 3 July 1969 over the Northern Hemisphere. The features on the ozone map agree, in general, with both the features on the C_T and N_T maps in Figures 11 and 12 and with the 200 mb chart in Fig. 13. This is to be expected in light of the work by Lovill (1972) including the determination of a relation between horizontal gradient of total ozone and jet stream speeds. Thus the global total ozone maps and the tropopause maps are complementary.

2.4 Supporting Data

In order to match and check results from the satellite experiments over the northern hemisphere, programs have been developed to read from tape and objectively analyze standard meteorological data archived each day by the National Meteorological Center, NMC. Special statistical characteristics of the atmospheric circulation (see the previous annual report) were compiled from rawinsonde data over both

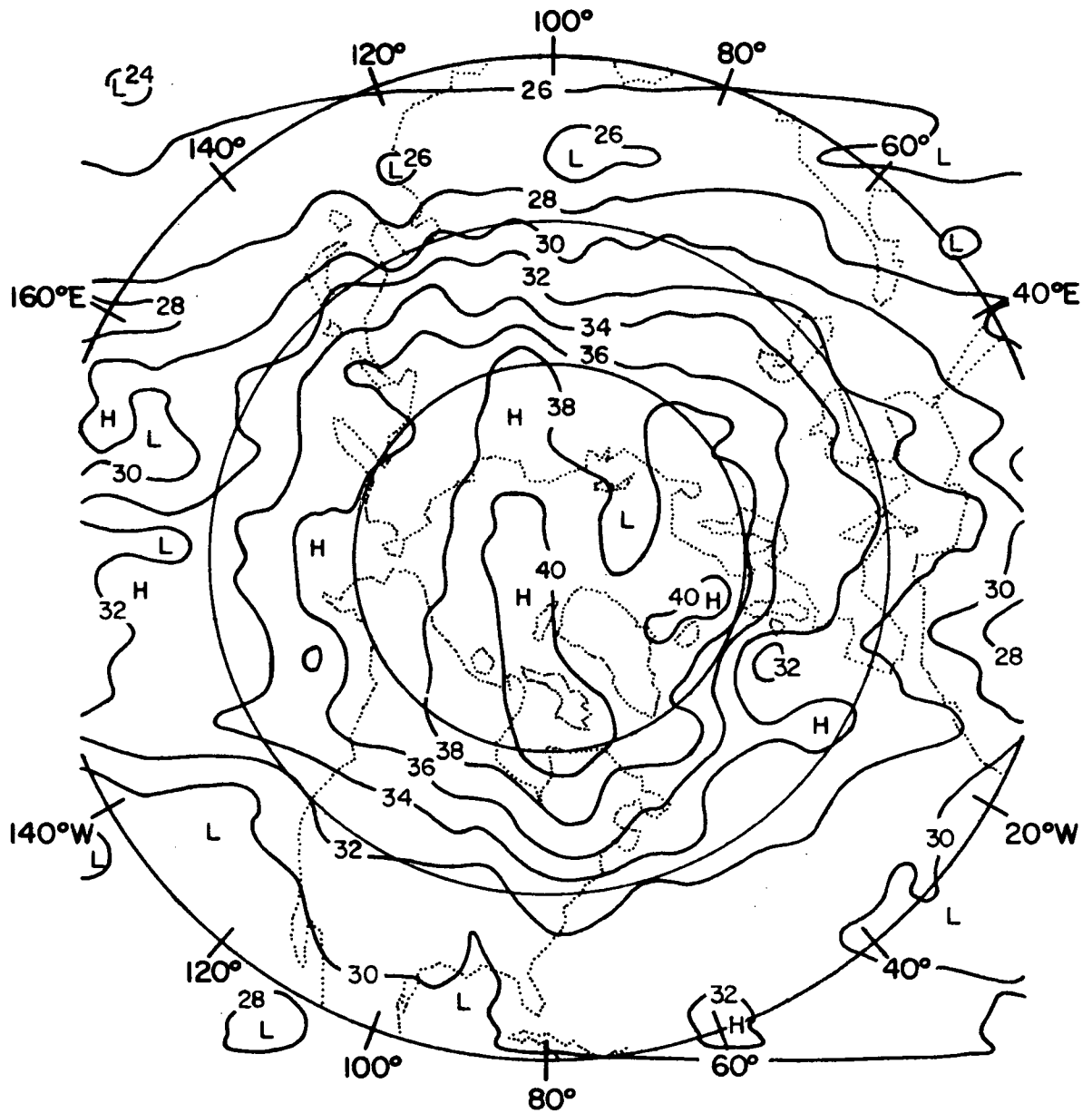


Fig. 14 - Northern Hemisphere Analysis of Total Ozone for 3 July 1969.
Units are in tens of $\text{m} \cdot \text{atm} \cdot \text{cm}$.

hemispheres. These results, compiled in a M.S. thesis by Mr. R. Abbey, provide an indication of the relative importance of various planetary and cyclone scale wave regimes in the respective hemispheres. Thus, they aid and guide the satellite-based research.

During the course of his research using ozone amounts inferred from IRIS, Dr. Lovill took full advantage of his extensive collection of ground-based ozone measurements. A library of satellite photo montages in the Atmospheric Science department is used extensively by the faculty and students for the Grant research.

Near the close of this reporting period, the first EOLE data were received by the project. Tapes can be read and use of the data will be described in the next report.

3.0 PROGRAM FOR THE NEXT REPORTING PERIOD

The ozone analysis pursued by Dr. Lovill should be extended to additional seasons in both hemispheres. From the "ozone waves" which appear in a continuity diagram presentation we can establish phase-wind group velocity effects that can be used to arrive at planetary and cyclone wave lengths. The behavior of these waves during different seasons in the two hemispheres should give some indications of cyclone frequencies and intensities. Especially in the southern hemisphere these data can be tested against the findings from the EOLE balloon experiment. These comparisons can be made on a statistical basis only, because the period of the EOLE program does not fit the NIMBUS data period.

The mapping of tropopause heights will be compared more closely with horizontal gradients in total ozone, both sets of data giving an indication of the position and intensity of jet stream. Attempts will also be made to use the information on tropopause location to improve the vertical temperature profiles derived from satellite data by inversion techniques. Instead of stratifying the data sample into latitude bands we will attempt to apply inversion methods to data arranged according to tropopause pressure and temperature as determined from IRIS data.

Regression techniques, especially non-linear regression equations will be tested further as to their usefulness in arriving at the upper tropospheric and stratospheric temperature distributions from radiance data, and at geopotential height fields of constant pressure surfaces. Again, independent knowledge of the tropopause location,

derived from IRIS data might help to improve these regression techniques. The data base of geopotential height and temperature maps derived from satellite data will be broadened considerably beyond the data set, for which the regression method has been tested so far.

With more analyses available, especially from the southern hemisphere, we will attempt to estimate the energetics of the general circulation as outlined on p. 45 of our last Annual Report (Reiter, et al., 1971). Especially values of available potential energy and kinetic energy will be derived from satellite data and the significance of the variability with time will be tested.

Our ozone analysis techniques, together with stratospheric temperature and geopotential height analyses derived from satellite data should be extended to NIMBUS 4 data. Results from these studies will lend themselves to comparisons with the Oxford analyses derived from the Selective Chopper Radiometer flown on Nimbus 4.

Analyses of the water vapor distribution, even though they were not pursued vigorously during the present grant period, will be considered as helpful augmentation in developing quantitative descriptions of flow patterns in the troposphere.

4.0 CONCLUSIONS AND RECOMMENDATIONS

Following the early work of testing and program development, the NIMBUS-3 ozone analysis is now complete (see Appendix I). Special areas for further study of the ozone data have been noted. Of course we also recommend that NIMBUS-3 results be checked using NIMBUS-4 measurements.

We have developed cloud checks independent of surface data, that will allow satisfactory study of atmosphere thermal structure in both hemispheres above the 700 mb level. We use inversion of radiances, definitely below 200 mb; regression on radiance for inferring the thermal structure at 100 mb and above. Calibration of our methods over the N. H. is satisfactory, once we have eliminated an apparent problem with the radiosonde temperatures reported at 30 mb.

In addition, a promising and economical method to infer tropopause pressure and temperature from the IRIS radiances is available. It may aid the general thermal inversion and regression measurements. It definitely complements these analyses and also those of the ozone amounts.

As this report is written we have already moved into the analysis and diagnostic phase of the thermal structure portion of the project. Development and testing has been slow but profitable. Meanwhile the data base for analysis (IRIS, SIRS) has been increasing. Fortunately, in addition to NMC data we will now have global SCR and southern hemisphere EOLE data to compare with our diagnostic results.

We are most anxious to apply the developed techniques to a large data base to allow the most meaningful analysis of interhemispheric circulation differences. If NASA can provide the basic data tapes, our experienced personnel (faculty, students and programmers) are ready for production runs on the CSU and NCAR computers. As in our prior

5.0 REFERENCES

- Abbey, R., 1972: Spectra of atmospheric motions. M.S. thesis, Department of Atmospheric Science, Colorado State University, Fort Collins, Colorado.
- Chahine, Moustafa T., 1970: Inverse Problems in Radiative Transfer: Determination of Atmospheric Parameters. J. Atmos. Sci., 27: 960-967.
- Conrath, B. J., R. A. Hanel, V. G. Kunde and C. Prabhakara, 1970: The infrared interferometer experiment on NIMBUS III. Goddard Space Flight Center, Greenbelt, Maryland.
- Craig, Richard A., 1951: Radiative Temperature Changes in the Ozone Layer. Compendium of Meteorology, T. F. Malone (Editor), American Meteorological Society, Boston, Mass.
- Finger, Frederick G., and Raymond M. McInturff, 1968: The Diurnal Temperature Range of the Middle Stratosphere. J. Atmos. Sci., 25: 1116-1128.
- Fritz, S., 1970: Earth's radiation to space at 15 microns: Stratospheric temperature. J. Appl. Meteor., 9(10): 815-824.
- Holmström, I., 1963: On a method for parametric representation of the state of the atmosphere. Tellus, 15: 127-149.
- Karandikar, R. V., 1946: Radiation Balance of the Lower Stratosphere. Part I - Height distribution of Solar Energy Absorption in the Atmosphere. Proceedings of the Indian Academy of Sciences, (A) 23: 70-96.
- List, Robert J. (Editor), 1971: Smithsonian Meteorological Tables, Sixth Revised Edition, Smithsonian Institution Press, Washington, D.C.
- Lorenz, E. N., 1967: The nature and theory of the general circulation of the atmosphere, WMO, 161 pp.
- Lovill, J. E., 1972: Characteristics of the General Circulation of the Atmosphere and the Global Distribution of Total Ozone as determined by the NIMBUS III Satellite Infrared Interferometer Spectrometer. Atmospheric Science Report #180, Colorado State University, Fort Collins, Colorado.
- Mitra, S. K., 1951: General Aspects of Upper Atmospheric Physics. Compendium of Meteorology, T. F. Malone (Editor), American Meteorological Society, Boston, Mass.
- Obukhov, A. M., 1960: On statistically orthogonal expansion of empirical functions. Izvestiya Geophys. Ser. 1960, 288-291. (English translation, 432-439.

- Reiter, E. R., et al., 1971: Interhemispheric Comparison of Atmospheric Circulation Features as Evaluated from NIMBUS Satellite Data. Annual Report, Grant NGR 06-002-098, 1 April 1970 - 30 June 1971, Dept. of Atmospheric Science, Colorado State University, Fort Collins, Colorado.
- Rodgers, C. D., 1970: Remote Sounding of the Atmospheric Temperature Profile in the Presence of Clouds. Quart J. Roy. Met. Soc., 96: 654-666.
- Smith, W. L. and S. Fritz, 1969: On the statistical relation between geopotential height and temperature-pressure profiles, ESSA Tech. Memo. NESCTM-18, U. S. Dept. Com., NESG, 16 pp.
- Smith, W. L., H. M. Woolf and W. J. Jacob, 1970: A regression method for obtaining real-time temperature and geopotential height profiles from satellite spectrometer measurements and its application to NIMBUS III "SIRS" observations. Mon. Wea. Rev., 98(8): 582-603.
- Wooldridge, G., and E. R. Reiter, 1970: Large scale atmospheric circulation characteristics as evident from GHOST balloon data. J. Atmos. Sci., 27(2), 183-194

APPENDIX I

Characteristics of the General Circulation
of the Atmosphere and the Global Distribution of Total Ozone
as determined by the NIMBUS III Satellite
Infrared Interferometer Spectrometer

CHARACTERISTICS OF THE GENERAL CIRCULATION OF THE ATMOSPHERE
AND THE GLOBAL DISTRIBUTION OF TOTAL OZONE AS DETERMINED BY THE
NIMBUS III SATELLITE INFRARED INTERFEROMETER SPECTROMETER

by

James Edward Lovill

This report was prepared with support under
Grant NGR 06-002-098, National Aeronautics
and Space Administration. Partial computer
support was funded under Contract
AT(11-1)-1340, U. S. Atomic Energy Commission.
Principal Investigator: E. R. Reiter

Atmospheric Science Paper No. 180

Department of Atmospheric Science
Colorado State University
Fort Collins, Colorado

February 1972

ABSTRACT

Ozone is an important atmospheric trace constituent. The depletion of solar radiation between approximately 2000 and 3000 Å is the result of strong absorption by ozone in the ultraviolet wavelengths. The energy absorbed in this process is the prime source of thermal energy in the stratosphere. Because of this, ozone plays an important role in the large-scale motions of the atmosphere. As a result, there is an ever-increasing interest in global total ozone measurements. The paucity of total ozone measuring stations over vast regions of both the Northern and Southern Hemispheres has greatly hindered any complete understanding of the role stratospheric ozone plays in the general circulation processes of the atmosphere. With total ozone sensors on earth-orbiting satellites the ozone over the entire earth is remotely measured daily. The conclusions of some of the analyses from the first satellite (Nimbus III) are discussed in this paper.

A strong correlation was found between the meridional gradient of total ozone and the wind velocity in jet stream systems. A procedure evolved which will allow the computation of the wind velocity at 250 mb. This should prove to be a useful relation to apply over the oceanic regions of the Northern Hemisphere and throughout most of the Southern Hemisphere. Wind velocities at jet aircraft operation levels could then be forecasted by consulting the daily satellite total ozone analyses.

A study of the total ozone distribution over two tropical storms indicated that each disturbance was associated with a distinct ozone minimum.

A comparison of time-longitude stratospheric radiance values at 60°S with values of the total ozone indicated that low (high) radiance values corresponded very closely with the low (high) ozone variations. The speed at which these ozone 'waves' progress eastward is greater in the winter hemisphere. The speed of eastward progression decreases as one approaches the lower latitudes in the winter hemisphere. In the equatorial region and in the Northern Hemisphere summer there is not a strong eastward progression of the ozone 'waves' but a westward progression.

The average latitudinal distribution of ozone is described for the first time, both temporally and spatially, during the autumn and winter in the Southern Hemisphere. The lowest mean total ozone value for the globe is observed at 6°S .

Maps are presented that describe the distribution of total ozone for the entire period (April to July 1969) for the Northern and Southern Hemispheres. Closely spaced total ozone isolines appear to reveal a rather strong jet stream west of South America at approximately 35°S . A large region of low total ozone was observed in the tropics, extending from Southeast Asia eastward to the central Pacific.

Both the Northern and Southern Hemispheres appear to provide 'anchoring' mechanisms for total ozone ridges. The most predominant ridges are also associated with the 'tightest' ozone gradients. In the Northern Hemisphere these locations are primarily Eastern North America, Central Europe and Eastern Asia. In the Southern Hemisphere

ridges are evident over the East Indian Ocean, the Central Pacific Ocean and the Eastern Atlantic. The ridges correlate closely with upper atmosphere height contours. The ridge pattern is easier to delineate in the Southern Hemisphere winter than in the Northern Hemisphere summer. The 'tightest' gradient of total ozone in either hemisphere was seen over Japan. This correlates closely with the high frequency of jet streams observed over the region.

An average global value of the total ozone for the entire period was calculated to be ^{330.3} ~~330.3~~ m-atm-cm.

James Edward Lovill
Atmospheric Science Department
Colorado State University
Fort Collins, Colorado 80521
February, 1972

ACKNOWLEDGEMENTS

The author gratefully acknowledges the patient guidance and encouragement of Dr. Elmar R. Reiter during the preparation of the work described here. Mr. Ronald Holle gave unselfishly of his time to provide pertinent conventional tropical data contained in this paper. Very special thanks must go to Drs. Thomas B. McKee, Thomas H. Vonder Haar, Myron L. Corrin, Stephen K. Cox, and William E. Marlatt at Colorado State University and Drs. Vincent V. Salomonson, C. Prabhakara, and William Nordberg at the Goddard Space Flight Center, National Aeronautics and Space Administration for their encouragement.

Mr. Robert Gobin aided significantly in data reduction. The majority of the computer programming was done by Miss Carroll Underwood, who also gave unselfishly of her time. Miss Ruth Armstrong, Mrs. Juanita Veen, and Mrs. Marjorie Kuhre typed the majority of the final manuscript.

This research was sponsored by Grant NGR 06-002-098, National Aeronautics and Space Administration. Partial computer support was funded under Contract AT(11-1)-1340, U.S. Atomic Energy Commission. Additional computer time was furnished by the National Center for Atmospheric Research (sponsored by the National Science Foundation).

TABLE OF CONTENTS

	Page
TITLE PAGE	1
ABSTRACT.....	1i
ACKNOWLEDGEMENTS.....	v
LIST OF TABLES.....	ix
LIST OF FIGURES.....	x
1.0 INTRODUCTION.....	1
1.1 The Nimbus III Spacecraft.....	1
1.2 The Photochemistry of Stratospheric Ozone.....	5
1.3 Background of Early Investigations and Inadequacies of Present-Day Conventional Data.....	8
2.0 ERROR ANALYSIS AND DATA PREPARATION.....	11
2.1 Typical Data Orbit.....	11
2.2 A Comparison of Inversion Data with Regression Data at Daily Intervals.....	14
2.3 A Comparison of Dobson Data with Regression Data at Monthly Intervals.....	15
3.0 TOTAL OZONE GRADIENTS NEAR STRONG BAROCLINIC ZONES.....	19
3.1 Meridional Gradients of Ozone Near Jet Maxima.....	20
3.2 Total Ozone Distribution Over a Strong Pacific Cyclone and the Associated Jet Stream System.....	22
3.3 Tropical Storm Ava and the Meso-Scale Total Ozone Distribution.....	24
3.4 Typhoon Susan and the Meso-Scale Total Ozone Distribution.....	26

TABLE OF CONTENTS - Continued

	Page
4.0 GLOBAL OZONE CLIMATOLOGY: TEMPORAL AND GEOGRAPHICAL VARIATIONS.....	29
4.1 General Remarks.....	29
4.2 Northern and Southern Hemisphere Comparisons.....	29
4.21 Inter-hemispherical Comparisons of Monthly Ozone Variability.....	31
4.211 A Detailed Study of April in the Northern Hemisphere.....	33
4.212 A Comparison of General Features in the April to July Mean Maps.....	34
4.213 Monthly Southern Hemisphere Variability.....	39
4.3 The Longitudinal Progression of Ozone 'Waves'....	45
4.31 The Variation of Total Ozone at 60° for 17 Days in May 1969.....	46
4.311 A Comparison of Radiance and Ozone Waves.....	46
4.312 Progression Rates for Eastward Moving Ozone 'Waves'.....	46
4.32 Hemispherical Differences in Longitudinal Progression During June 1969.....	48
4.4 Average Variation of Total Ozone with Latitude...	53
4.5 The Global Distribution of Ozone from 19 April to 21 July 1969.....	56

TABLE OF CONTENTS - Continued

	Page
4.6 Spectral Analyses of Ozone and Wind Variability..	60
5.0 SUMMARY AND CONCLUSIONS.....	63
5.1 Suggestions for Future Research.....	67
REFERENCES.....	68

LIST OF TABLES

<u>Table</u>		<u>Page</u>
2.2	A comparison of the regression vs the inversion technique for determining total ozone at 9.6 μm from the Nimbus III Satellite.....	16
2.3	Standard errors between the average Dobson spectrophotometer total ozone and IRIS regression coefficient determined total ozone values at selected locations.....	17
4.312	Eastward progression rate of total ozone 'waves' at 60°S for the Period 3-19 May 1969.....	48
4.6	Periods at selected latitudes where the coherence-squared value is a maximum.....	61

LIST OF FIGURES

<u>Figure</u>		<u>Page</u>
1.1.1	The Nimbus III Spacecraft. The locations of individual experiments are indicated. The Infrared Interferometer Spectrometer (IRIS) is at the lower right of satellite.....	2
1.1.2	The Infrared Interferometer Spectrometer thermal emission spectrum of the earth which was taken over the equatorial Pacific Ocean on 15 April 1969 (Nimbus Project, 1969).....	4
2.1	Total ozone distribution during orbital pass Number 1077 on 3 July 1969. Data have been analyzed by the Regression Technique.....	12
3.1	Graph of the non-linear relation between total ozone gradient (in m·atm·cm/km) and the jet stream core velocity (in ms ⁻¹). (Numbers identify individual cases of study.).....	21
3.2	Total ozone contours (m·atm·cm) over a large Pacific Ocean extra-tropical cyclone and its associated jet stream (7 May 1969).....	23
3.3	Total ozone analysis (m·atm·cm) over Tropical Storm Ava on 7 July 1969. Ava indicated by A and the numbers 3 - 6 indicate locations earlier in July.....	24
3.4	Total ozone analysis (m·atm·cm) over Typhoon Susan on 22 April 1969. Susan is indicated by S. The numbers 18 - 21 indicate locations earlier in April.....	27
4.211.1a	Total ozone distribution in the Northern Hemisphere for April 1969. (Total ozone values in m·atm·cm).....	32
4.212.1b	Same as 4.211.1a except for May 1969.....	35
4.212.1c	Same as 4.211.1a except for June 1969.....	36
4.212.1d	Same as 4.211.1a except for July 1969.....	37
4.213.1a	Same as 4.211.1a except for April 1969, Southern Hemisphere.....	40
4.213.1b	Same as 4.211.1a except for May 1969, Southern Hemisphere.....	41

LIST OF FIGURES - Continued

<u>Figure</u>		<u>Page</u>
4.213.1c	Same as 4.211.1a except for June 1969, Southern Hemisphere.....	42
4.213.1d	Same as 4.211.1a except for July 1969, Southern Hemisphere.....	43
4.21	Time-longitude graph of the total ozone at 60°S for May 1969. Total ozone values are in m·atm·cm. The W and C symbols represent regions of warm and cold stratospheric temperatures according to Fritz (1970). The straight lines represent the average tilt in time with longitude of the respective zone 'waves'.....	47
4.32.1	Time-longitude variations of the total ozone (m·atm·cm) during June 1969 at 60°S.....	49
4.32.2	Time-longitude variations of the total ozone (m·atm·cm) during June 1969 at 40°S.....	49
4.32.3	Time-longitude variations of the total ozone (m·atm·cm) during June 1969 at 20°S.....	50
4.32.4	Time-longitude variations of the total ozone (m·atm·cm) during June 1969 at the Equator....	50
4.32.5	Time-longitude variations of the total ozone (m·atm·cm) during June 1969 at 20°N.....	51
4.32.6	Time-longitude variations of the total ozone (m·atm·cm) during June 1969 at 40°N.....	51
4.4	The variation of total ozone with latitude, from 80°N to 80°S for April, May, June and July 1969.....	54
4.5.1	The average distribution of total ozone (m·atm·cm) for the Northern Hemisphere from 19 April to 21 July 1969. Shading represents total ozone values less than 240 m·atm·cm.....	57
4.5.2	The average distribution of total ozone (m·atm·cm) for the Southern Hemisphere from 19 April to 21 July 1969. Shading represents total ozone values less than 240 m·atm·cm.....	58

LIST OF FIGURES - Continued

<u>Figure</u>		<u>Page</u>
4.6.1	Spectra of the total ozone at 50° from 21 April to 21 July 1969.....	62
4.6.2	The same as Figure 4.6.1 except 250 mb wind velocity. The -1 line indicates the slope of the k^{-1} exponential function.....	62

1.0 Introduction

1.1 The Nimbus III Spacecraft

The Nimbus III spacecraft completes a sunsynchronous, circular orbit 1109 km above the earth once every 107.3 minutes. The satellite was launched into orbit at 07:54:03 GMT on 14 April 1969. Nimbus III represented a major upgrading of the Nimbus I and II spacecraft. Figure 1.1.1 represents the basic configuration of the Nimbus III spacecraft. The location of various experiments and spacecraft controls is indicated in the figure.

One of the major experiment packages added to this satellite was the Michelson infrared interferometer spectrometer (IRIS). The IRIS instrument has several scientific objectives. It has been providing information on the structure of the atmosphere and the emissive properties of the earth's surface. It is designed to measure the thermal emission spectrum of the earth between 5 and 25 microns (400 and 2000 cm^{-1}) with a spectral resolution of 5 cm^{-1} . (Spectra cannot be used between 5 to $7\text{ }\mu$ (1400 to 2000 cm^{-1}) because of decreased responsivity of greater than thirty percent in this portion of the wave band.) In the spectral region covered, ozone, water vapor, and carbon dioxide bands are available in addition to spectral features associated with such minor atmospheric constituents as methane and nitrous oxide. The specific intensity measured in the absorption bands and in the transparent 'windows' can be used to determine vertical profiles of ozone, temperature, and water vapor.

The essential part of the interferometer (Hanel, 1969) is the beam splitter which divides the incoming radiation into two essentially equal components. After reflection on the fixed and moving mirrors,

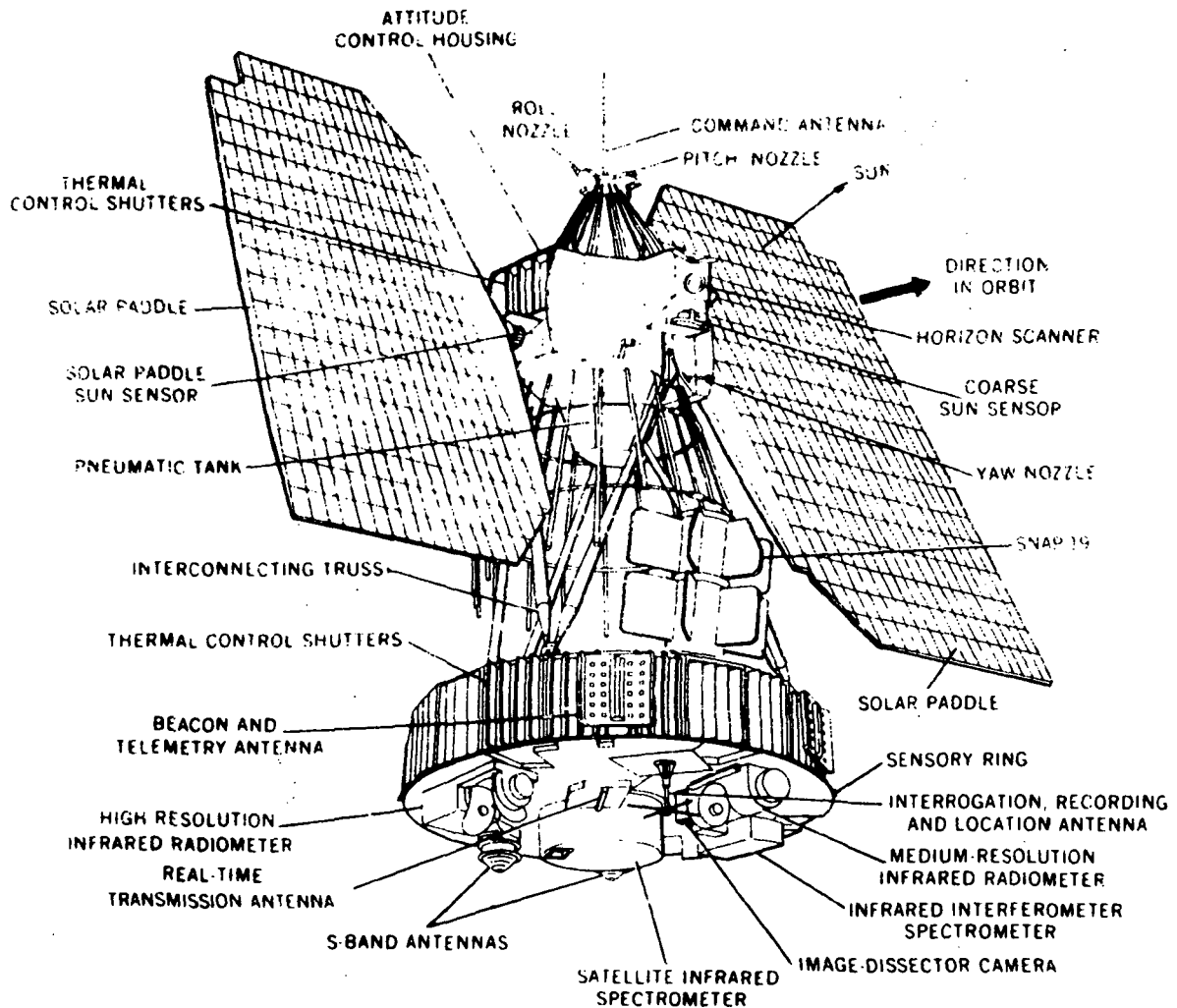


Fig. 1.1.1. The Nimbus III Spacecraft. The locations of individual experiments are indicated. The Infrared Interferometer Spectrometer (IRIS) is at the lower right of satellite.

respectively, the two beams interfere with each other with a phase difference proportional to the optical path difference between both beams. The recombined components are then focused onto the bolometer where the intensity is recorded as a function of path difference, δ . Since the mirror motion is phase locked to the

spacecraft clock, the mirror path difference is also proportional to time.

The central fringe may be light or dark depending on the δ between the two beams. For polychromatic radiation, neglecting constant terms, the signal (i) at the detector, referred to as the interferogram, is

$$i(\delta) = \int_0^{\infty} K_{\nu} (B_{\nu \text{ Scene}} - B_{\nu \text{ Inst}}) \cos (\pi \nu \delta - \phi_{\nu}) d\nu \quad 1.1(1)$$

The amplitude is proportional to a responsivity factor, K_{ν} , and the difference in radiance between the scene within the field of view, B_{ν} , and the instrument, B_{ν} . The phase is defined with respect to a point chosen as close as possible to, but not necessarily at, the zero path difference point. Imperfect optical compensation and residual phase shift in the analog part of the data spectrum cause the angle, ϕ , to depend on the wave number. Reconstruction of the spectrum is by a ground based IBM-360 computer at the Goddard Space Flight Center (GSFC).

A sample spectrum calculated from a single interferogram is shown in Figure 1.1.2. One interferogram is obtained every sixteen seconds. Twelve and one-half percent of the IRIS measurement time is consumed in a calibration procedure. After 14 interferograms are taken in the operating mode a comparison is performed with two known calibration sources to establish an absolute intensity scale. An onboard, warm blackbody provides one calibration interferogram and the interstellar void (assumed a nearly zero degree sink) the other (Nimbus Project, 1969).

Interferograms are transformed by means of the Cooley-Tukey method (Cooley and Tukey, 1965). An apodisation function is applied to each interferogram prior to transformation in order to reduce side lobes of the instrument function. The particular apodisation function has the form $(0.54 + 0.46 \cos 2 \pi \tau/T)$ where τ is the distance from the

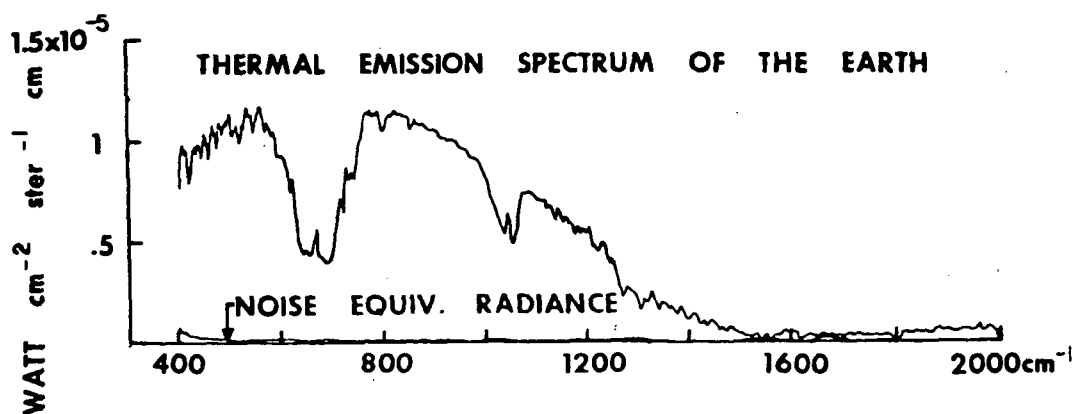


Fig. 1.1.2. The Infrared Interferometer Spectrometer thermal emission spectrum of the earth which was taken over the equatorial Pacific Ocean on 15 April 1969 (Nimbus Project, 1969).

center and T is the total length of the interferogram (see also, Blackman and Tukey, 1958).

The Fourier transformation yields two amplitudes

$$a = \int_{-\infty}^{+\infty} A(\delta) i(\delta) \cos 2 \pi \nu \delta d\delta \quad 1.1(2)$$

and

$$b = \int_{-\infty}^{+\infty} A(\delta) i(\delta) \sin 2 \pi \nu \delta d\delta \quad 1.1(3)$$

where $A(\delta)$ is the apodisation function. From a_ν and b_ν a magnitude

$$C_\nu = (a_\nu^2 + b_\nu^2)^{1/2} \quad 1.1(4)$$

and a phase

$$\phi_v = \arctan b_v/a_v \quad 1.1(5)$$

are computed. The location of the pronounced central peak of the calibration interferograms is taken as the phase reference point. For atmospheric interferograms which may or may not have a strong central peak, the average phase ($\bar{\phi}_v$) reference point of several calibration interferograms is used (Hanel, 1969). This spectrum reduction is described in a more complete manner by Hanel (1969), in which he delineates a method to eliminate noise components and defines the final calibration procedure.

The field of view of the IRIS instrument is 4° half angle (Nimbus Project, 1969). This corresponds to an area on the earth's surface with a diameter of 150 km.

High quality IRIS data were obtained until the experiment failed on 22 July 1969. Failure was attributed to the opening of the compensating clip at the bolometer which produced a large positive transient at the input to the bolometer pre-amplifier. One hundred days of data were obtained before this point in time, of which 95 days are used in this paper.

1.2 The Photochemistry of Stratospheric Ozone

The photochemistry of the stratosphere in general and of the ozone problem specifically was first thoroughly discussed by Chapman (1930). Further development and refinement of the theory have been advanced by Dütsch (1946, 1956) and Craig (1950).

Many different approaches have been taken toward a better understanding of upper atmospheric ozone photochemistry. Hunt (1966) has discussed the photochemistry of ozone in a moist atmosphere. Schiff (1964) and Norrish and Wayne (1965) have investigated the photochemistry of ozone in an oxygen-hydrogen atmosphere. Crutzen (1971) has discussed the photochemistry of ozone in an oxygen-hydrogen-nitrogen oxide atmosphere. Complicated reactions like those discussed by Crutzen (1971) may number as many as fifty-six.

To a first approximation it is sufficient to assume only an oxygen atmosphere for the discussion here. Ozone or triatomic oxygen, O_3 , may be formed by a three body collision



M is any third atom or molecule. In order for the reaction in 1.2(1) to occur, atomic oxygen must be formed. This will happen if a quantum of solar energy dissociates O_2 ,



The reaction in 1.2(2) will occur only if $\lambda < 2423 \text{ \AA}$.

Ozone may be destroyed in two ways: by collision,



or by photo-dissociation,



The reaction in 1.2(4) will transpire only when $\lambda < 11,000 \text{ \AA}$.

As one goes from the lower stratosphere to the mesosphere the ratio O_2/O approaches zero. As a result there is less O_2 available for reaction 1.2(1) and ozone is not formed as rapidly. Additionally, there is more atomic oxygen, O , available so that reaction 1.2(3) occurs more rapidly and thus ozone is destroyed. When these, and other reactions unfavorable to ozone formation, occur, the net result is a decrease of ozone. The height at which such a decrease usually commences in the middle latitudes is between 20 and 25 km. Although the ozone partial pressure may decrease above this level, the mixing ratio normally remains constant in the mesosphere at a value between 5 and 15 $\mu\text{g/g}$ (see, e.g., Hering, 1964; Lovill and Miller, 1968).

Ozone in the lower stratosphere and upper troposphere is a quasi-conservative property and serves as an excellent tracer of atmospheric motions. This is clearly seen in the values presented by Paetzold (1953). He shows that the time required for ozone to decrease $1/e$ of its value at 25 km is equal to 10^2 days; at 20 km, 10^3 days; and at 15 km, 10^4 days.

Ordinarily the region near and at the surface of the earth will act as a sink for ozone. Little is known of the actual processes that bring about ozone decomposition in this region. Volz (1952) and Cadle and Ledord (1966) have shown that ozone can be decomposed upon contact with clouds, H_2S , and other substances. On the other hand, investigations by Haagen-Smit (1952) and Renzetti (1955) have shown that ozone also may be formed near the surface of the earth. This occurs when hydrocarbons in a polluted atmosphere are irradiated by sunlight. The direct result is large local concentrations of ozone. Therefore under

these conditions this region near the surface will act as a source rather than as a sink.

The ozone concentration generally decreases in the vertical, from the surface to the vicinity of the tropopause, then increases to a maximum concentration at an average height in the middle latitudes of about 25 km, after which it steadily decreases with height. The height of maximum concentration in the stratosphere varies considerably with latitude. The height varied from 14 km at 80°S (Lovill, 1965) during the Southern Hemisphere winter of 1963 to 26 km near the equator (Hering and Borden, 1964).

1.3 Background of Early Investigations and Inadequacies of Present-Day Conventional Data

Dobson (1930) was the first to initiate a large-scale total ozone sampling program. This began over a decade after Fabry and Buisson (1913) developed the technique for the basic measurements. For his complex of stations Dobson (1931) developed a spectrophotometer (usually referred to as the Dobson Total Ozone Spectrophotometer or simply The Dobson) for the measurement of total ozone. Over the past forty years the instrument has changed little and it is still essentially the same device originally used in Dobson's first network. With few exceptions the Dobson Spectrophotometer is the standard instrument for the measurement of total ozone in most countries. The major exception is the Soviet Union which uses the Filter Ozonometer (Bojkov, 1969).

Total ozone has also been measured by the integration of the vertical distribution of ozone determined from ozonesondes. The two

primary types of ozone sensors are the chemical (see e.g. Brewer and Milford, 1960; Komhyr, 1969; Lovill, 1969, 1970a) and chemiluminescent (Regener, 1960) devices. These ozonesondes are far more useful for their ability to measure vertical ozone distribution than for their total ozone measurements. This fact will become abundantly obvious in Chapter 3 when vertical and horizontal transport processes in the vicinity of a jet stream system are discussed in relation to early work by Briggs and Roach (1963).

Climatological studies of total ozone utilizing the Dobson Spectrophotometer and the ozone sensors reveal the following for the Northern Hemisphere (for a summary see Dürsch (1969)). Total ozone reaches a maximum in the late winter and early spring. Minimum values occur during late summer and early autumn. The highest total ozone concentrations are recorded in the higher latitudes and the lowest values at the lower latitudes. Considerably less is known of the total ozone distribution over the Southern Hemisphere due to a serious lack of observing stations. Total ozone variations in the mid-latitudes of the Southern Hemisphere appear to be similar to those in the Northern Hemisphere, at least when data from sites in Australia are analyzed (most of the Southern Hemisphere large-scale ozone analyses have been conducted by Kulkarni (1966) and Pittcock (1968)).

The paucity of total ozone measuring stations over the oceans and in the tropics in the Northern Hemisphere and throughout the Southern Hemisphere has greatly hindered any complete understanding of the role stratospheric ozone plays in the general circulation of the atmosphere. Considerable information is available on the latitudinal variation of total ozone over the continents in the Northern Hemisphere (see

London, 1963) and the temporal variations of the vertical distribution of ozone at individual stations (Hering and Borden, 1964; 1965a, b; 1967). But essentially no information is available over the Northern Hemisphere oceans. Little can be advanced about the longitudinal variations of total ozone except over the continents in the Northern Hemisphere. In addition, due to the sparsity of stations in the Southern Hemisphere, almost no understanding is available of the inter-hemispherical exchange processes dealing with ozone.

The Nimbus III sensor provides two or three thousand total ozone data points over the entire globe each day. The analysis of these data will provide significant advances in research related to both ozone and the general circulation. These data will be discussed in the following sections.

2.0 Error Analysis and Data Preparation

Data obtained from an earth-oriented satellite must be calibrated in some manner. This is usually accomplished by comparison with ground-truth data. In Chapter 2.1 the pertinent data readout obtained during a typical orbit is briefly discussed. Chapter 2.2 discusses the merits of satellite data processed by the inversion method and the regression technique. In Chapter 2.3 a comparison is made between various surface ozone station data and data obtained by the Nimbus III satellite. A brief description of the method by which the data are computer-processed is given in the final section.

2.1 Typical Data Orbit

Theoretically, approximately 4000 atmospheric spectra could be obtained each day from the IRIS unit if all spectra were useful and all orbital data were transmitted to the earth receiving stations. In reality, however, only about 50% of the spectra have been reduced via regression coefficients to total ozone data. Noise problems within individual spectra eliminate many spectral data; additionally, not all data stored onboard the satellite are transmitted (see Chapter 4). Dr. C. Prabhakara (GSFC, NASA) provided the computer tape with the regression coefficient ozone data on which the analyses in this paper are based.

Figure 2.1 is representative of the typical total ozone distribution observed during a Nimbus III orbital 'sweep' from the high latitudes of the Northern Hemisphere to the high latitudes of the Southern Hemisphere. The data shown in Figure 2.1 were obtained during orbit 1077 on 3 July 1969. During this satellite pass the data orbit 'swept' from western Siberia southward across the western Pacific and into the

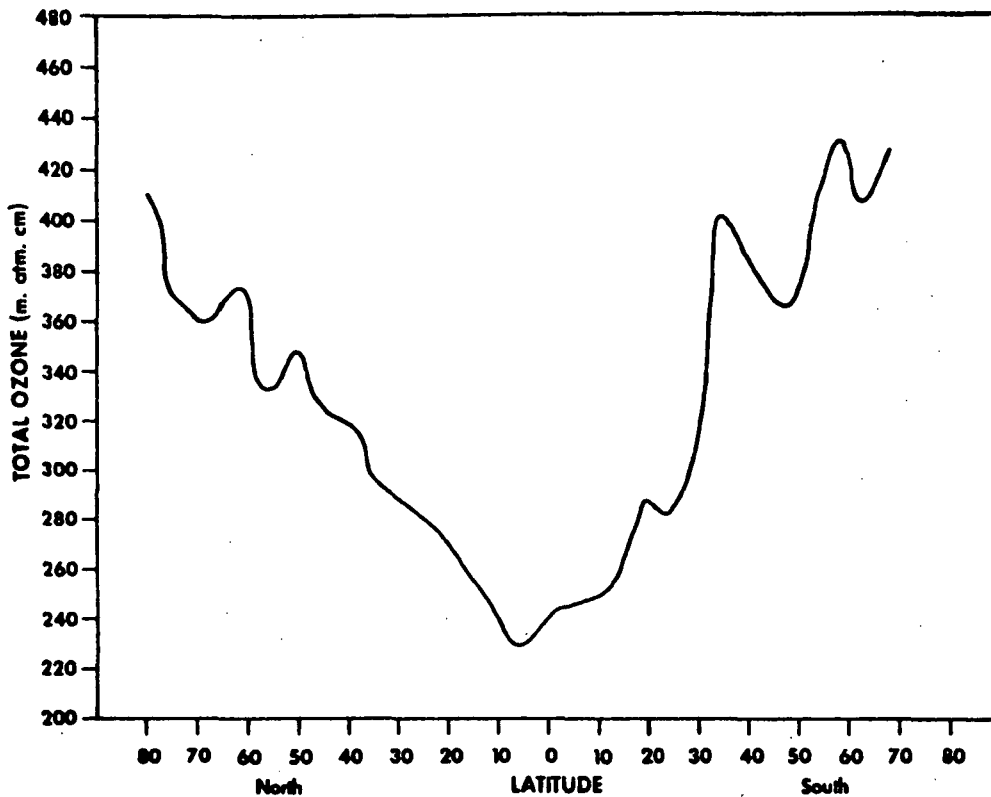


Figure 2.1 Total ozone distribution during orbital pass Number 1077 on 3 July 1969. Data have been analyzed by the Regression Technique.

Southern Hemisphere across central Australia and ended near the coast of Antarctica after covering the eastern Indian Ocean.

Even a cursory examination of Figure 2.1 indicates a large range in total ozone concentration from the polar regions to the equatorial area. Total ozone values approximately double from the 230 m.atm.cm (milli.atmospheric.centimeter) amount near the equator to 460 m.atm.cm at 58°S. In chapter 1 total ozone amounts on the average

were observed to decrease smoothly from high to low latitudes. This obviously is not the situation during this orbit. In fact the total ozone amount never decreases smoothly from the polar regions toward the equator. There are always perturbations among the best line fit. These perturbations as seen in Figure 2.1 are mostly the result of the redistribution of total ozone in the atmosphere by cyclones and anticyclones. The largest perturbations along the line in Figure 2.1 are associated with the strongest anticyclone/cyclone systems. Since over ninety percent of the ozone in the atmosphere is found in the stratosphere, it becomes quite obvious that the redistribution process will be most efficient when these systems extend to their greatest vertical extent into the stratosphere. If this reasoning is carried one additional step farther, then one may stipulate that when large height differences exist between anticyclonic and cyclonic systems in the stratosphere, large changes in ozone will occur along this height gradient.

This argument can be validated when the ozone perturbations in Figure 2.1 are compared with upper-atmosphere synoptic features. In Figure 2.1 the largest gradient of total ozone occurs near 30°S. At this location the satellite is measuring total ozone over south Australia. A strong anticyclone is evident over north central Australia and a cyclone is seen just off the south west tip of Australia, both extending into the stratosphere. The height gradient between these two systems at 300 mb is the greatest found on earth on this particular date. A 'tight' gradient such as seen in this case between two pressure systems is indicative of a strong geostrophic wind velocity. This suggests a strong positive correlation between the geostrophic wind and the

total ozone gradient. This correlation will be explored further in chapter 3.

Two other features, in Figure 2.1, both pertaining to the geographical and seasonal bias of ozone distribution, are worthy of mention. The winter hemisphere has a greater amount of ozone in its atmosphere than the summer hemisphere (see chapter 1). Since Figure 2.1 represents the winter season in the Southern Hemisphere, one expects to observe more ozone in the Southern than in the Northern Hemisphere. This is indeed the case. There is 19 percent more ozone at 70°S than at the comparable northern latitude; the largest difference indicates 11 percent more at 60°S than at 60°N . A second feature of this particular orbit indicates the global minimum of total ozone to be located in the Northern Hemisphere (the summer hemisphere) at 8°N .

2.2 Comparison of Inversion Data with Regression Data at Daily Intervals

Prabhakara (1969), Prabhakara and Conrath (1970), and Prabhakara, et al. (1971 b,c) have discussed the technique by which total ozone concentration may be determined from the IRIS instrument on the Nimbus III satellite. Prabhakara and Conrath (1970) have determined a method to invert the radiance measurements made by the IRIS. A number of calculations were made using this technique to determine total ozone. The inversion results yielded a standard error of estimate of six percent when compared with the surface Dobson spectrophotometer data. A complete discussion of the ozone inversion technique and the associated errors can also be found in Russell (1970).

The inversion technique is a time-consuming computer method and therefore a costly means of determining total ozone on a global scale. For this reason regression coefficients were determined by Prabhakara, et al. (1971a) by which total ozone amounts could be produced.

These coefficients were based upon data obtained from April 1969 Nimbus III readout. Table 2.2 is a comparison of the regression and the inversion methods for determining total ozone at 9.6μ . All global total ozone data were compared for 23 April and 3 July 1969. Since the April data were the base for determining the regression coefficients, the real test of the coefficients arrives when the comparison is made of the two methods on 3 July. However, the two dates indicate (see Table 2.2) an identical standard error of estimate of 3.7 percent when all latitudes are compared. As expected, in general, the error between the two techniques increases as one goes from low to high latitudes. This is because the remote sounding techniques do not perform well where vertical temperature profiles are nearly isothermal, as they tend to be in the lower stratosphere of high latitudes.

Fifty-eight percent of the inversion data points were greater than those found from the regression coefficients for the 23 April comparison. The 3 July case, however, indicated that 53 percent of the regression data values were greater than the inversion technique values. It, therefore, appears as though there is little bias toward positive or negative values.

2.3 A Comparison of Dobson Data with Regression Data at Monthly Intervals

The Dobson Spectrophotometer measurements of total ozone are usually considered to be highly accurate. On an absolute scale the Dobson instrument probably has an absolute error no greater than one to three percent. In the following paragraphs these data are compared with the satellite data.

TABLE 2.2

A Comparison of the Regression vs the Inversion Technique for
Determining Total Ozone at 9.6 μ m from the NIMBUS III Satellite

Date	Latitude (N, S)	Number of Compared Data Points	Standard Error of Estimate	Percent of Data Points at which Regression Value Greater than Inversion Value
23 April 1969	0 - 30	86	3.9%	42%
	30 - 60	53	3.3	49
	60 - 80	28	4.1	32
	All Latitudes	167	3.7	42
3 July 1969	0 - 30	130	3.5	44
	30 - 60	97	3.8	63
	60 - 80	68	4.1	56
	All Latitudes	295	3.7	53

Prabhakara (1969) and Prabhakara and Conrath (1970) expended considerable effort to determine the regression coefficients to be used to convert the IRIS spectra to meaningful ozone data. Sufficient satellite total ozone data are available such that a study may be made which compares the average Dobson data with the average regression determined ozone values for the period.

In order to have a comparison of the highest quality, it was necessary to eliminate some of the days during which a less than sufficient number of ozone data points were processed from the satellite. Seventy-five days were selected and a map of the average global ozone distribution during these 75 days was constructed.

Only 38 surface stations around the world took total ozone measurements during a sufficient number of days for significant statistical comparison with the IRIS data. Only six of these stations were in the Southern Hemisphere. Table 2.3 describes these results.

Table 2.3

Standard error of estimate between the average Dobson Spectrophotometer total ozone and IRIS regression coefficient determined total ozone values at selected locations.

Number of days Dobson obs taken	Number of sta- tions in sample	Standard deviation
74 - 75	9	3.6%
73 - 75	11	3.9
70 - 75	19	4.6
65 - 75	35	6.0
60 - 75	38	6.1

Table 2.3 indicates that when data were available on every day, or every day except one, that the two data sets compare quite favorably. The standard error of estimate of 3.6% is well within the acceptability limits.

When all 38 stations are included in the data sample this increased to 6.1%. However, with this number of stations, as much as 20% of the days may be missing in some cases.

The largest standard errors were found over the Soviet Union. The standard error in several instances exceeded 15%. In all cases the Soviet Filter Ozonometer reported a lower value of ozone than the IRIS instrument (see also Bojkov, 1969).

3.0 Total Ozone Gradients Near Strong Baroclinic Zones

Reiter (1971) summarized past research work on the ozone distribution in the atmosphere that could be derived from ozone soundings, aircraft measurements and ground-based umkehr techniques (For specific details see Lovill, 1965, 1969, 1970a, b, c; Lovill and Miller, 1968; Bojkov and Lovill, 1969; Reinking and Lovill, 1971). From these studies it becomes quite obvious that the dynamically induced vertical motions associated with jet maxima near the tropopause extend into the lower stratosphere and induce an appreciable vertical transport of ozone. Specifically, it was found that the stratospheric air on the cyclonic side of the jet stream, which is subject to sinking motions, abounds in atmospheric ozone; whereas the warm air in the jet core and on the anticyclonic side of the jet maxima, being of tropospheric origin, is deficient in ozone. Since the ozone surplus on the cyclonic side, as well as the deficit on the anticyclonic side, extends over a considerable depth of the atmosphere, one would expect to find a marked horizontal gradient of total ozone to be present across the axes of well-developed jet streams.

Thirty-three cases of relatively sharp meridional gradients of total ozone in the Northern Hemisphere on the objectively analyzed charts of ozone as observed by Nimbus III, have been tested with respect to the presence of absence or jet maxima. Not only was a strong correlation found between such gradients of ozone and the proximity of jet streams, but the magnitude of these gradients appeared to stand in direct relationship with the intensity of the jet stream, i.e., with the peak wind speeds observed in each case.

In one individual case of 7 May 1969, a strong Pacific cyclone and its associated jet are shown superimposed on an objective analysis of the IRIS ozone values. Maxima and minima of ozone correspond well with the postulated vertical motion fields near the jet core.

A tropical storm in the eastern Pacific and a hurricane in the western Pacific are shown with the objective ozone analysis superimposed. Both cyclones are associated with ozone minima. Horizontal and vertical circulation mechanisms of each are discussed in relation to total ozone distribution.

3.1 Meridional Gradients of Ozone Near Jet Maxima

A relation between total ozone gradients and jet stream wind maxima was first suspected when the daily maps of total ozone from Nimbus III were compared with the National Meteorological Center (NMC) wind analyses. Further work indicated that the strongest total ozone gradient was directly related to the highest wind speeds from the NMC analyses. Figure 3.1 represents the slightly non-linear relation that was found to exist between these two parameters after 33 case studies were plotted.

The plot of the total ozone gradient vs. the jet stream core velocity was found to have the least scatter when winds at the 250 mb level were used. The plot represents IRIS total ozone and NMC wind velocity comparisons for areas throughout the Northern Hemisphere, from 20°N to 70°N . The majority of the data were obtained between 30° and 60°N , over the large land masses of North America, Europe, the Soviet Union, and China as well as the oceanic regimes of the north Pacific and Atlantic.

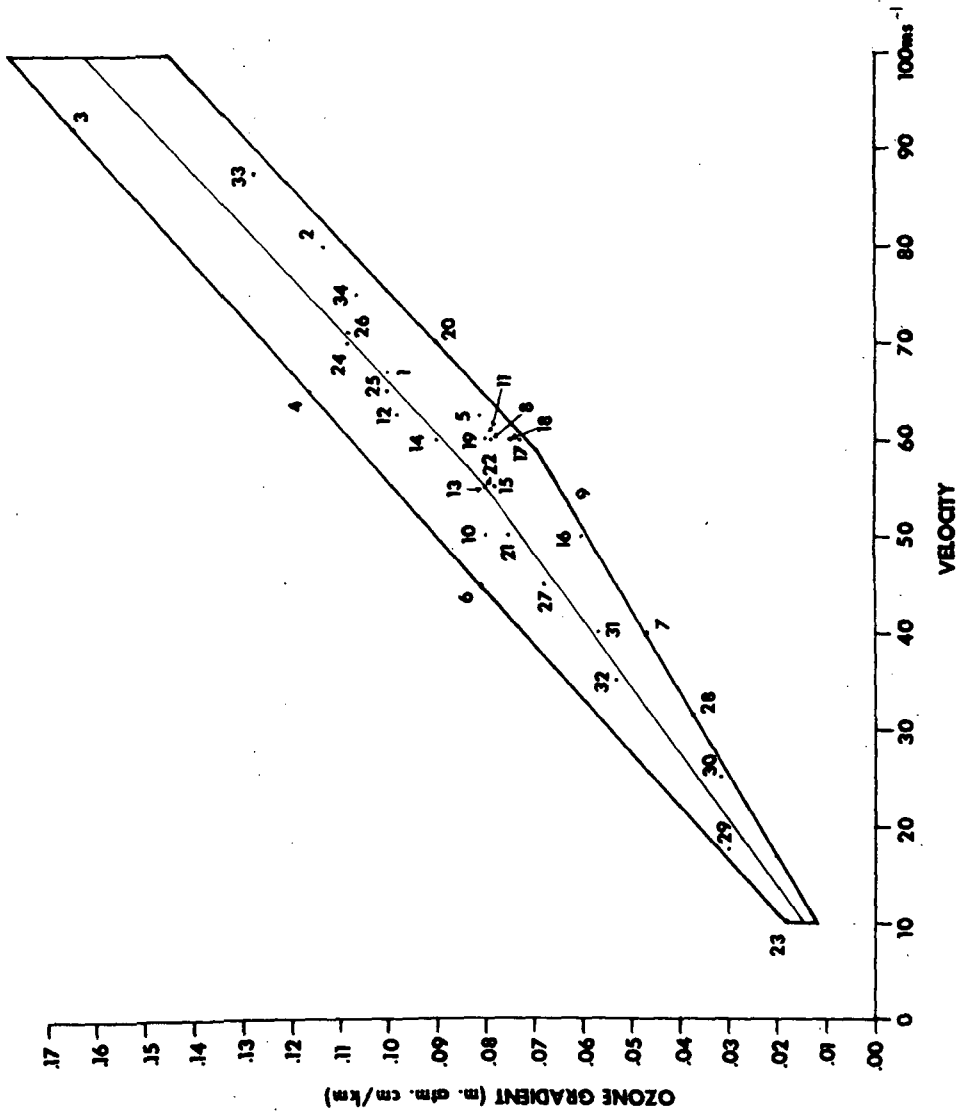


Fig. 3.1. Graph of the non-linear relation between total ozone gradient (in m.atm.cm/km) and the jet stream core velocity (in ms^{-1}). (Numbers identify individual cases of study.)

There is little doubt, after even a brief study of Figure 3.1, that the dynamics of the jet stream are extremely effective in redistributing the total ozone in the stratosphere. It is generally felt (Reiter, 1963; Lovill and Miller, 1968) that on the cyclonic side of a jet stream system where air is descending, the stratospheric air is richer in ozone concentration than on the anticyclonic side of the jet maximum where ascending motions are prevalent and air poor in ozone is found.

3.2 The Total Ozone Distribution Over a Strong Pacific Cyclone and the Associated Jet Stream System

Figure 3.2 indicates in a remarkable manner the dynamics of a strong jet stream system, such as discussed earlier. In this figure (7 May 1969) a strong Pacific cyclone and its associated jet are shown superimposed on an objective computer analysis of the IRIS total ozone values. Several features are worthy of mention.

As previously discussed, the stratospheric air on the north (cyclonic) side of the jet stream is much higher in ozone than the air on the south (anticyclonic) side. In Figure 3.2 the large ozone maximum of $450 \text{ m} \cdot \text{atm} \cdot \text{cm}$ to the northwest of the jet axis and of the cloud band is produced by the vertical motion around the jet axis and by horizontal advection of higher ozone amounts from the north. At the same time the circulation around the cyclonic system is responsible for the large ozone minimum centered at 40°N and 170°E . This minimum is a result of ascending air to the south of the system as well as the advection of ozone 'poor' air from the tropics. Notice the extremely strong north-south gradient of ozone isolines along longitude 120°E . From 27°N to 53°N there is an increase in ozone by $180 \text{ m} \cdot \text{atm} \cdot \text{cm}$.

This is an increase in total ozone of over 60% in 26 degrees of latitude. The highest wind velocity along the jet is associated with the very closely spaced ozone isolines at 45 to 50°N near 160°E. This corresponds correctly with the findings in Section one.

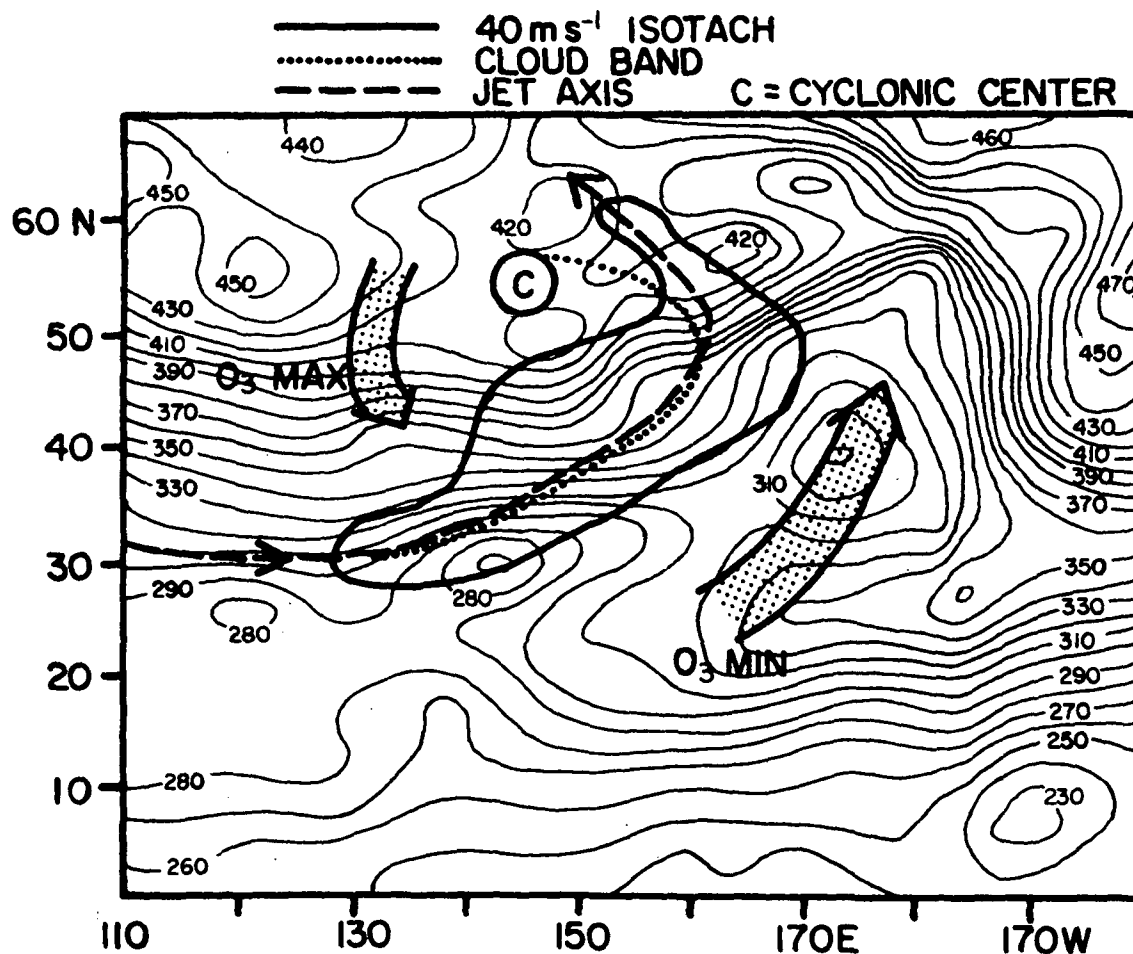


Fig. 3.2. Total ozone contours (m·atm·cm) over a large Pacific Ocean extra-tropical cyclone and its associated jet stream (7 May 1969)

3.3 Tropical Storm Ava and the Meso-Scale Total Ozone Distribution

Tropical Storm Ava was first observed as a closed circulation by ESSA 9 off the coast of Guatemala on 1 July 1969. The location of the storm for the next several days is indicated in Figure 3.3.

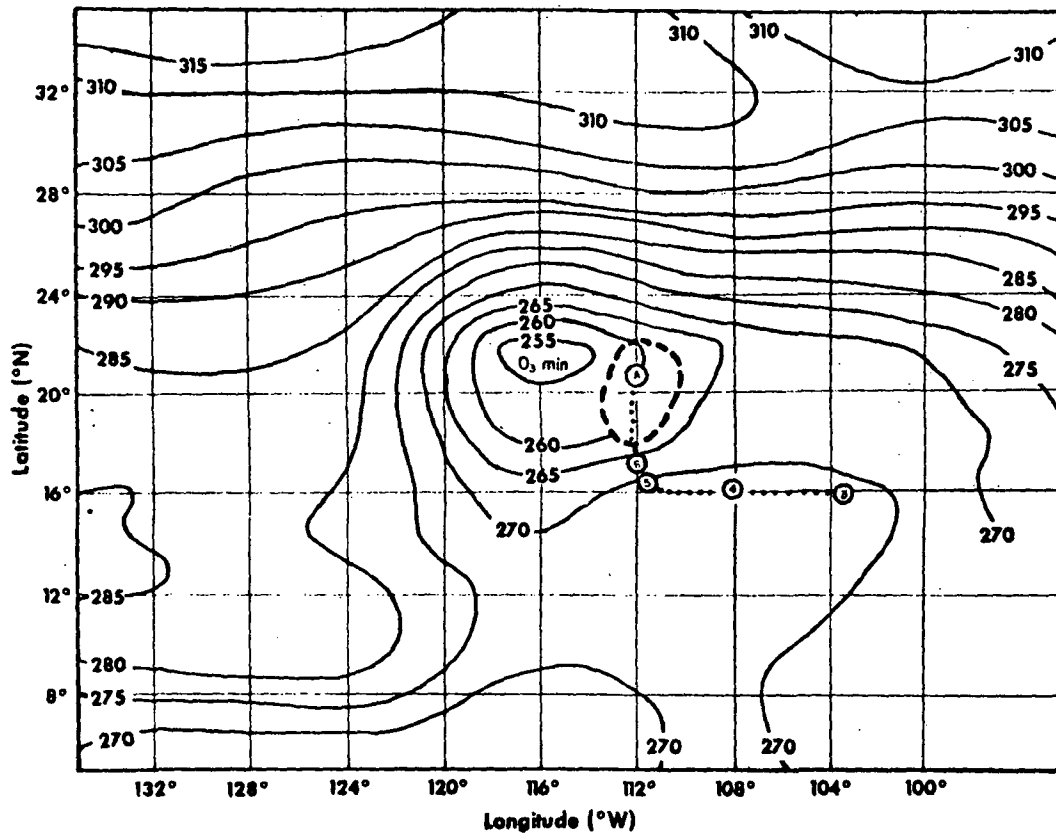


Fig. 3.3. Total ozone analysis (m.atm.cm) over Tropical Storm Ava on 7 July 1969. Ava indicated by A and the numbers 3 - 6 indicate locations earlier in July.

Ava reached a maximum intensity of 29 ms^{-1} just before a sharp turn to the north began on 5 July (see Figure 3.3). Ava had decreased in intensity by 7 July. The ESSA 9 cloud picture of the area for 7 July

indicated an inner closed cloud band of approximately 120 km diameter and an outer closed band of several hundred kilometers extent. The outer band is indicated by dashed lines in Figure 3.3. The storm appeared to have clouds associated with its movement that enclosed an area of 7° latitude by 7° longitude.

The isolines of total ozone measured by Nimbus III during this period have been superimposed upon the outline of this tropical storm which is in its dissipation stage. Penn (1965, 1966) has provided information on the distribution of ozone at various levels in two hurricanes. U-2 aircraft observations over one of the hurricanes indicated that from about 120 to 105 mb the region over the eye was warmer and considerably richer in ozone than other areas in the vicinity of the storm. Higher in the stratosphere (100 to 50 mb) the horizontal gradients were weak.

The major difference between Penn's data and the data presented here is that whereas his measurements were of the local ozone distribution at specific locations, Figure 3.3 represents the total ozone distribution over a large region which surrounds the tropical disturbance. (A similar analysis of the total ozone distribution over Hurricane Bernice was undertaken by Allison, et al. (1971) using Nimbus III data.)

In Figure 3.3 a broad region of low total ozone concentration is seen surrounding tropical storm Ava. The center of low total ozone is just to the west of the storm. The distribution of total ozone around the tropical disturbance suggests, weak though it may be, that there is sufficient rising motion and advection of lower latitude

air in the vicinity of the storm to account for the total ozone minimum.

Additional investigations of the distribution of total ozone around tropical disturbances should shed more light on the stratospheric motion patterns associated with these storms. A stronger tropical disturbance will be discussed in the next section and it will be seen there that the total ozone is also a minimum when the storm is well above minimum hurricane strength.

3.4 Typhoon Susan and the Meso-Scale Total Ozone Distribution

Typhoon Susan began forming two days after the Nimbus III spacecraft was placed into orbit. The total ozone data in Figure 3.4 were obtained on 22 April 1969, the third day after the IRIS unit became fully operational. Although the disturbance was first noticed on 16 April, it did not attain typhoon strength until 20 April,

On 22 April winds near the eye were in excess of 50 ms^{-1} . At this time the ESSA 9 cloud photographs indicated that the typhoon covered a very large region of the Pacific. Cloud bands extended from 3 to 18°N and from 122 to 140°E , an area of fifteen by eighteen degrees.

The two most obvious cloud bands visible from ESSA 9 are shown in Figure 3.4. The location of Susan on 22 April is indicated by the S in the figure. The movement of the storm during the past four days is also indicated. The typhoon has slowed its forward movement and by the 22nd has begun curving to the northwest. At the time of

its location in Figure 3.4, Susan is only 750 km southeast of Manila and has just begun to move onshore over the Philippine Islands.

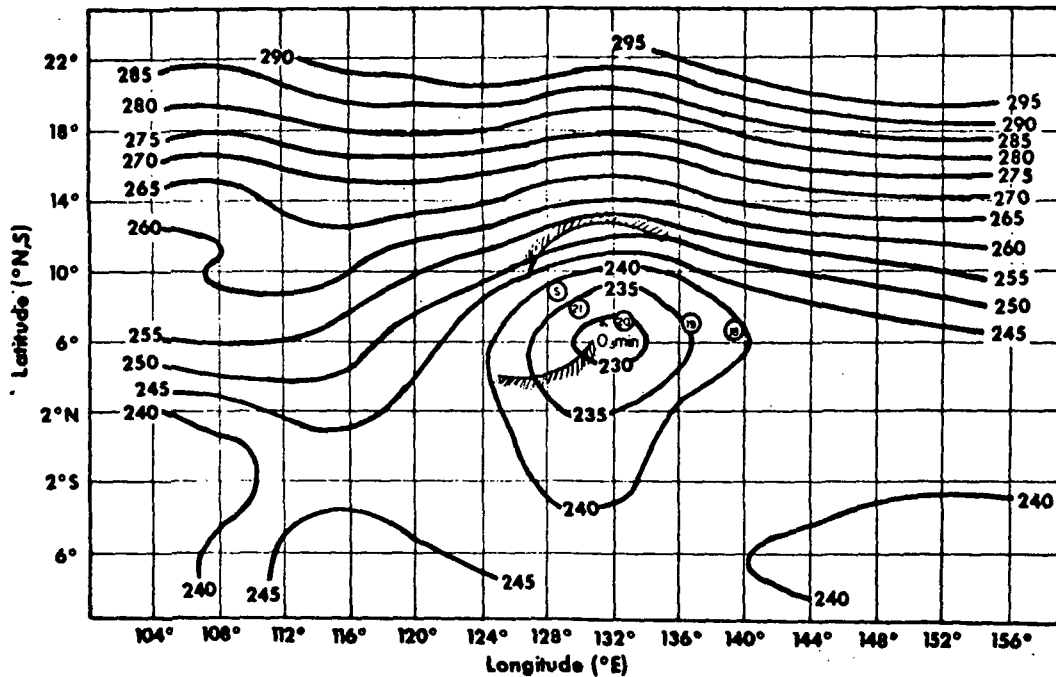


Fig. 3.4. Total ozone analysis (m.atm.cm) over Typhoon Susan on 22 April 1969. Susan is indicated by S. The numbers 18 - 21 indicate locations earlier in April.

Figure 3.4 indicates that a distinct total ozone minimum is surrounding the typhoon. The center of the minimum is approximately 390 km southeast of the typhoon center. This was the approximate location of Susan 48 hours previously.

It is suggested that the same mechanisms that were called upon to produce the total ozone distribution in tropical storm Ava may also be responsible for the total ozone distribution around Susan. The basic oddity of these two tropical storms is the following. The weaker tropical disturbance, Ava, had just as strong a total ozone minimum associated with it as did the stronger typhoon. One assumes that the vertical structure of the typhoon extends to considerably greater heights than that of a dissipating tropical storm such as Ava. Therefore the redistribution of total ozone around the more intense storm should be more obvious. This is not true in the case of the two tropical cyclones just examined in Figures 3.3 and 3.4. Evidently a great deal more study needs to evolve around this problem.

4.0 Global Ozone Climatology: Temporal and Geographical Variations

4.1 General Remarks

Dynamically induced subsiding motions, in combination with strong horizontal advection, behind a short-wave trough could produce large positive changes in the total ozone concentration over an extensive area. As was illustrated in Figure 3.2, the ozone concentration decreases rather markedly on the west side of a ridge: With these correlations we can interpret longer term temporal and geographical variations of ozone on a quasi-seasonal basis. Many general circulation characteristics may thus be portrayed by the ozone distribution.

4.2 Northern and Southern Hemisphere Comparisons

Several studies in recent years have shown distinct differences of the atmospheric general circulation of the Northern and Southern Hemispheres (for a summary, see Reiter, 1969). Whereas, earlier publications postulated a more zonal flow in the Southern Hemisphere supposedly because of less land mass and fewer mountain massifs, more recent investigations show that such statements may have to be qualified somewhat.

Wooldridge and Reiter (1970) have shown that significantly stronger horizontal anisotropy of flow prevails at cyclone wavelengths in the Southern than in the Northern Hemisphere, with meridional perturbations exceeding zonal flow perturbations. Eulerian spectral densities of the zonal component in the Southern Hemisphere were half of those in the Northern Hemisphere. This would imply that there is less energy at cyclone-wave frequencies, u , in the Southern than in the Northern Hemisphere. Wooldridge and Reiter (1970) suggest that this occurs because of a relative lack of orographically induced planetary long waves in the Southern Hemisphere that are superimposed upon the hemispheric jet

stream zones. They concluded that the relatively zonal character of the Southern Hemisphere pertains to the long planetary-scale waves only.

Starr and Dickinson (1963) have shown that standing eddies are very important in transport processes of the Northern Hemisphere. Obasi (1963a) pointed out that transient eddy processes are of utmost importance in the flux of momentum toward the pole in the Southern Hemisphere. Obasi (1963b) also found that the conversion of eddy kinetic to zonal kinetic energy by such waves was about twice as great in the Southern Hemisphere as in the Northern Hemisphere.

These studies imply that transport processes in the Southern Hemisphere depend more on the cyclone scale disturbances than in the Northern Hemisphere. In the Northern Hemisphere much transport is associated with standing eddies which have wave numbers of 1, 2, and 3.

Jet stream patterns in the Northern Hemisphere are strongly influenced by the hemispheric wave number three (Reiter, 1963). This results in the formation of the three strongest mean jet maxima over Japan, eastern North America, and Europe, (Kao and Hurley, 1962). On the average these jet stream systems are stronger in the Northern Hemisphere winter than in the summer.

In the Southern Hemisphere Van Loon (1964, 1965) finds a differently structured jet stream system: In winter, the zonal momentum is greatest. The momentum is distributed over two hemispheric jet stream systems. In the Southern Hemisphere summer only one jet stream system is reported (over the Indian Ocean) by Van Loon (1964). This single jet maximum has a greater velocity than either of the two jet maxima observed during the winter in the Southern Hemisphere.

Large-scale circulation patterns also show a disparity between the

Northern and Southern Hemispheres. Planetary waves number two and three shape the polar vortex in the Northern Hemisphere winter. In the stratosphere, the circulation is such that upward motion is seen over the North Polar Regions during the late winter during and after the breakdowns of the stratospheric polar vortex (Reed et al, 1963; Teweles, 1964). Subsiding motions are wide-spread over the middle latitudes (Reiter, 1969). Since ascending currents dominate in the equatorial regions, the general circulation of the stratosphere is accomplished by two cells which produce an observed spring maximum of ozone in middle and high latitudes of the Northern Hemisphere (Reiter, 1971). London (1963) in a state-of-the art paper presented seasonal and annual mean charts of total ozone data from sixty stations, most of which were in the Northern Hemisphere. He found in both the seasonal and annual means that three ozone maxima were evident in troughs extending from the high latitudes toward the equatorial regions. These waves in the ozone iso-lines conformed quite closely to the troughs in the stratospheric circulation pattern.

4.21 Inter-hemispherical Comparisons of Monthly Ozone Variability

Figures 4.211.1a, 4.212.1b, 4.212.1c, and 4.212.1d represent computer analyses of Northern Hemispheric total ozone data and Figures 4.213.1a to 4.213.1d show similar analyses for the Southern Hemisphere. The charts for April represent the last twelve days of the month and the analyses for July, the first twenty-one days of the month. More data were available for analysis in the Southern than in the Northern Hemisphere. For example in May in the Northern Hemisphere 22,519 points were analyzed. In the Southern Hemisphere 30,110 data points were available - an increase of 25%. This deficiency of points in the Northern Hemisphere is mostly

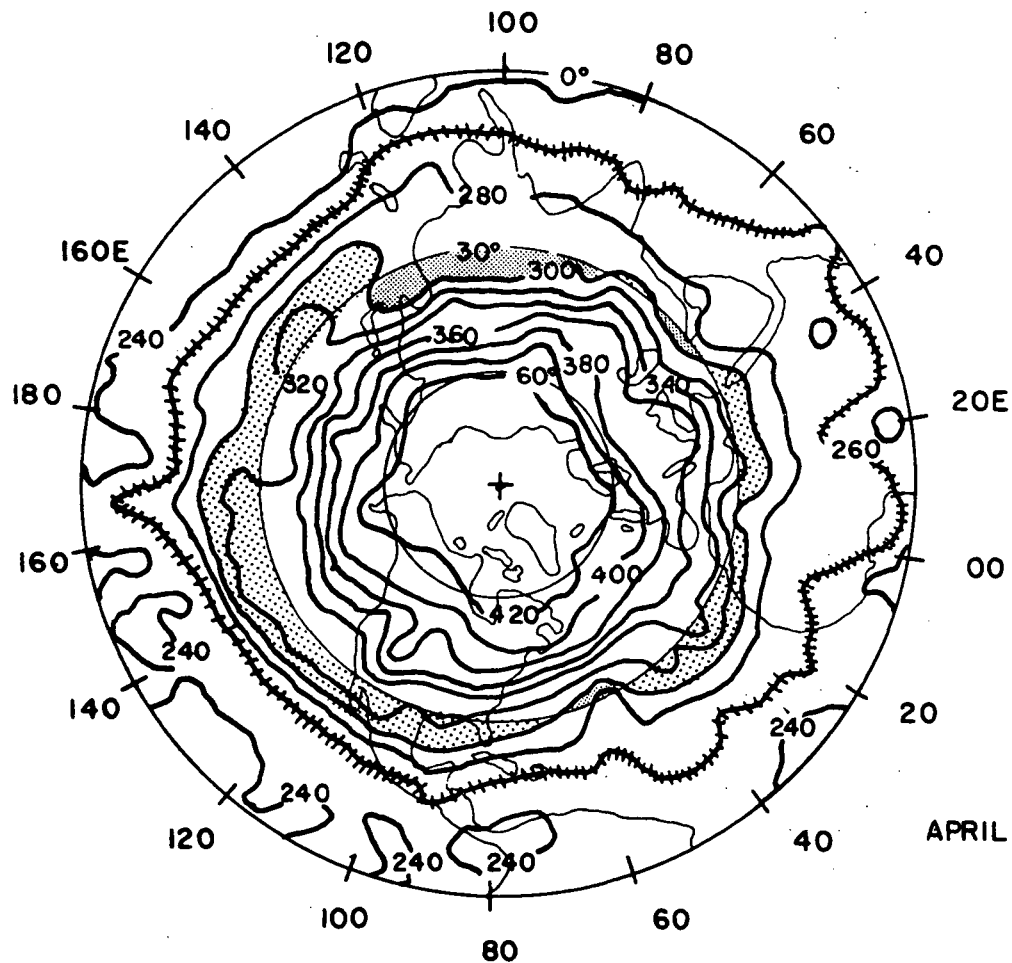


Fig. 4.211.1a Total ozone distribution in the Northern Hemisphere for April 1969. (Total ozone values in m.atm.cm)

due to data retrieval from the satellite at the two acquisition stations. All orbits cannot be recovered owing to memory storage on the satellite and to an insufficiently rapid data bit transmission from the spacecraft to the station.

4.211 A Detailed Study of April in the Northern Hemisphere

Figure 4.211.1a shows the mean total ozone distribution for April in the Northern Hemisphere. Two features are obvious in this figure: (1) a 'tight' ozone gradient extends from eastern North America to about 60°W in the western part of the Atlantic Ocean, and over eastern Asia and Japan; (2) there are four to five major waves in the ozone isolines.

An analysis of the National Meteorological Center (NMC) upper troposphere and lower stratosphere wind data indicates that the two regions with closely spaced ozone isolines coincide with the average location of strong baroclinic zones. The 'tight' gradient of mean total ozone concentration seems to be directly identifiable with the mean position of strong polar jet stream systems.

Four or five long waves also can be identified in the ozone isoline pattern. These ozone ridges (maxima) and troughs (minima) correspond closely to long-wave features found in the height contour fields at 300 to 100 mb. Shorter, transient total ozone waves tend to be filtered out in the averaging processes used to obtain monthly means. Several of these short-wave features are evident in this "April" map (Fig. 4.211.1a) however, since only twelve days of data were averaged. The other months have two to three times as many days to average, and thus identify mostly standing wave features.

In Figure 4.211.1a the areas from the 300 m-atm-cm total ozone isoline southward (northward in the Southern Hemisphere; see corresponding diagrams) of the thirty degree latitude line are widely dotted to indicate preferred global regions of southward total ozone transport by the standing, long planetary waves. The densely dotted areas from the

300 m·atm·cm isoline northward (southward in the Southern Hemisphere) of the thirty degree latitude line represent preferred global regions of northward total ozone transport. A large region over which the 300 m·atm·cm line is displaced north of 30°N extends from Central Asia to western Japan. With the exception of slight displacements to the north over Iran and Arabia and the Mid-Atlantic, the remaining area of the Northern Hemisphere has the 300 m·atm·cm isoline displaced to the south of 30°N . This implies that a larger amount of ozone is advected southward of 30°N than is advected northward at this time of the year. The orientation of the 300 m·atm·cm contour is mostly a function of the standing planetary wave system and of the resulting subsiding (ascending) and southward (northward) mass transport which results in preferred regions of total ozone maxima (minima). The average concentration of ozone along a latitude circle, however, is mostly a function of the zenith angle of the sun.

The 260 m·atm·cm contour for the months of April-June, and the 280 m·atm·cm contour for July have been marked especially, to emphasize preferred regions where ozone maxima exist in the tropics. In April (Fig. 4.211.1a) the 260 m·atm·cm contour dips far south and generally intercepts the equator over much of North Africa.

4.212 A Comparison of General Features in the April to July Mean Maps

In May, June, and July (Figs. 4.212.1b, c, d) a very 'tight' ozone gradient is evident again over eastern North America. It is worthy to note that this area of concentrated ozone contours has moved a considerable distance northward from April to July. In April the average value of total ozone off the east coast of North America at 45°N was 400 m·atm·cm. By July the value at this location had decreased to 340

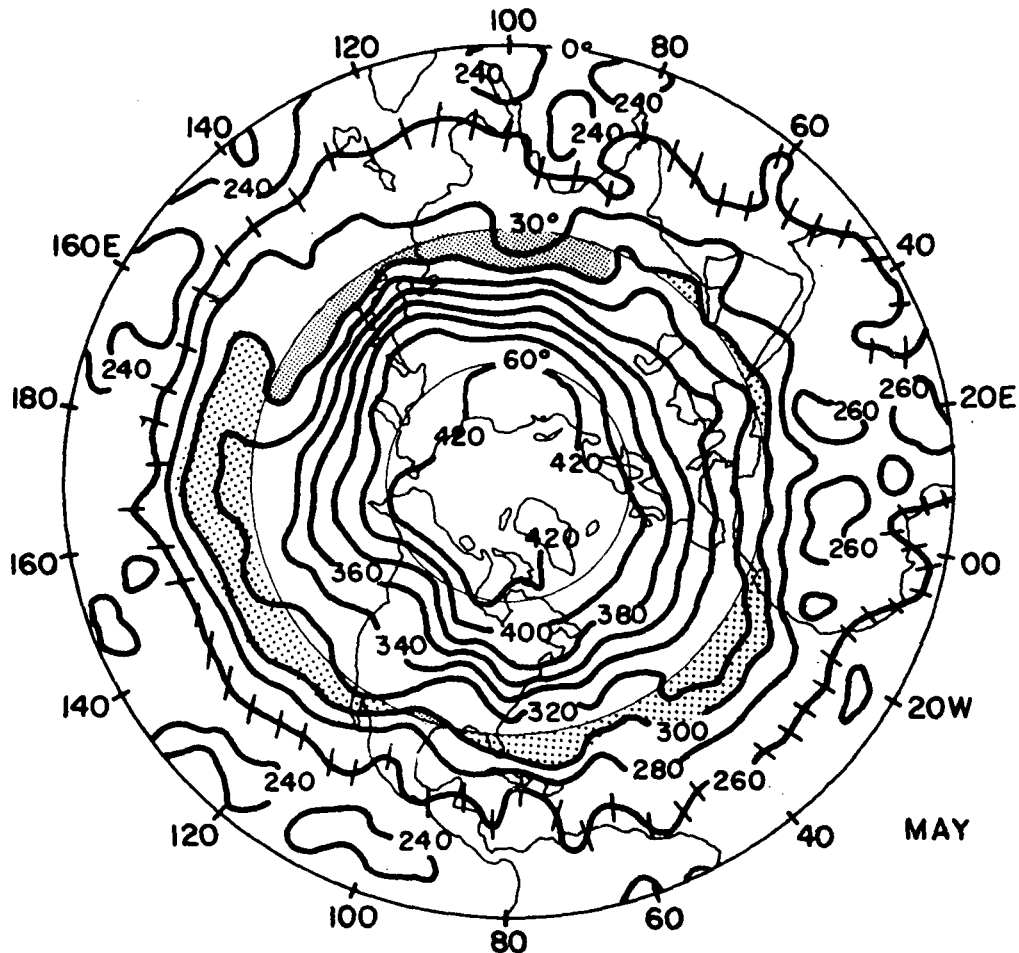


Fig. 4.212.1b Same as 4.211.1a except for May 1969.

m·atm·cm. This seems to correlate reasonably well with the weakening and movement toward the north of the baroclinic ozones. The tightly packed ozone contours seen over Central Asia and Japan in April appear to persist through July, but with considerable weakening after June over Japan. By comparison the gradient over eastern North America in July is 'tighter' than that of the gradient over Japan during that month, but about equal to that found over eastern Asia. Even though there are four standing

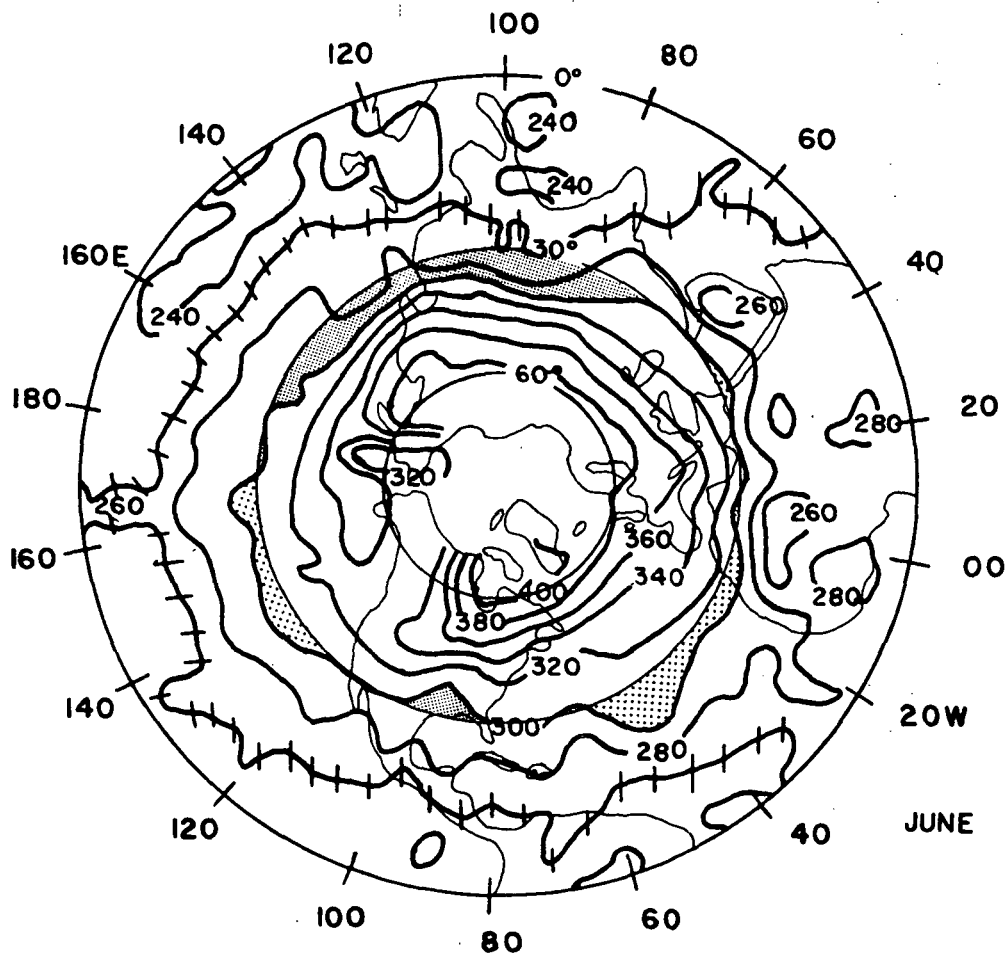


Fig. 4.212.1c Same as 4.211.1a except for June 1969.

planetary waves indicated in the height contour field (Scherhag, 1969c) and in the ozone contour field in July (Fig. 4.212.1d), it appears as though much of the jet stream activity is concentrated over eastern North America and eastern Asia. The ozone gradients over the rest of the Northern Hemisphere are considerably less than over these two regions.

Scherhag (1969a) reports that the average wind velocity for several Japanese stations between 35 to 40°N at longitude 135°E for May at 200 mb

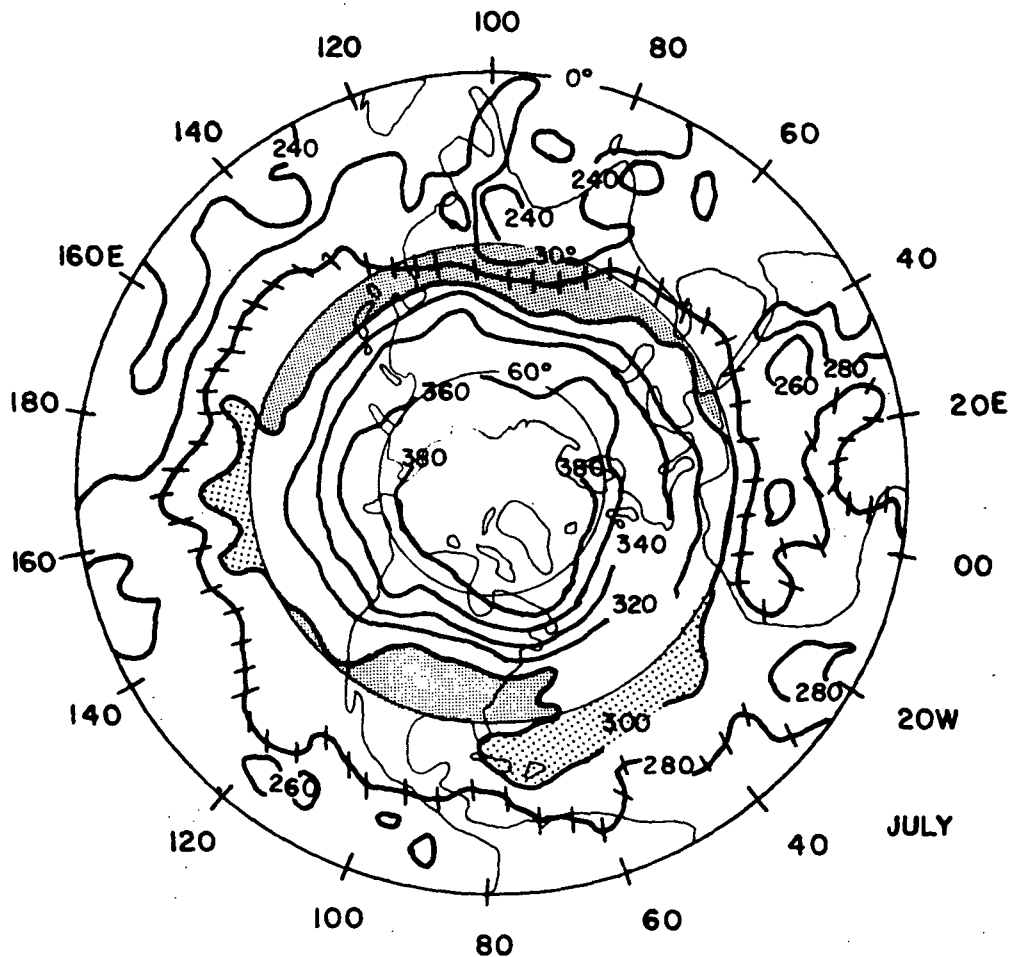


Fig. 4.212.1d Same as 4.211.1a except for July 1969.

was 40 ms^{-1} . The total ozone gradient in this region, using Figure 4.212.1b, was 0.54 in $\text{m} \cdot \text{atm} \cdot \text{cm}/\text{km}$. Using Figure 3.12.1, correlating ozone gradient and jet stream winds, we arrive at an estimated velocity of 37 ms^{-1} . This is in good agreement with the actually measured winds, even though the wind reports pertain to 200 mb, and the correlation chart was developed for use at 250 mb.

From April to July in the Northern Hemisphere (Figs. 4.212.1b-d)

there are three to five long waves visible in the total ozone contours. The month of June is the only month with a dominant three wave pattern. A closed center of total ozone appears in high latitudes at approximately 175°E longitude. A dominating feature on the 200 mb mean June contour map is a closed warm center west of Alaska (Scherhag, 1969b) in the same location as the closed ozone contours. This feature remained quasi-stationary during June and appears to have influenced rather markedly the upper atmospheric flow over western North America and northeast Asia.

In April we find most of the 300 m.atm.cm contour to the south of latitude 30°N . By July (Fig. 4.212.1d) much of this contour lies to the north of this latitude. The months in-between represent a transition period during which the general circulation in the Northern Hemisphere is in a state of decreasing kinetic energy and during which most centers of action have shifted northward.

Several interesting temporal variations of ozone at different geographical locations are worth mentioning. One of these locations is the United States. In April the 300 m.atm.cm contours extended to about 20°N in the longitude sector of the United States. But in May a small portion of this contour is noted pushing northward across 30°N over Texas. In June this area has enlarged to cover most of the south-central United States. By July a greater part of the United States has an ozone concentration of less than 300 m.atm.cm. This feature appears to imply that low amounts of total ozone are advected northward into an area centered on the 95th meridian. A region off the east coast of the United States, during April showed a north-ward indentation of 300 m.atm.cm line, and in July was seen to be a preferred region for a southward bulge of this contour line.

There was only one region in the Northern Hemisphere where the 300 m·atm·cm contour remained north of the 30°N latitude during all four months. This was the region from Central Asia to Japan. The area over which there was very little seasonal ozone variability at 30°N was from western North Africa to Iran (15°W to 60°E).

The 260 m·atm·cm contour in April, May, and June (280 m·atm·cm in July) characterizes the ozone distribution in tropical latitudes. Relatively high values of O_3 appear over Africa and the eastern Atlantic Ocean. The departures from zonal mean values are not strong, but nevertheless suggest the possibility that this is a preferred region (3°W to 60°E) for interhemispherical exchange of stratospheric air masses.

In general it appears that the western part of the Northern Hemisphere has the greatest seasonal variability of total ozone and that the eastern part has the least variability.

4.213 Monthly Southern Hemisphere Variability

There are a total of eleven active ozone surface stations in the entire Southern Hemisphere. As a contrast, the United States and Canada alone have thirteen stations. Of these eleven Southern Hemispheric stations there are four between the equator and 30°S , five between 30°S and 60°S , and two from 60°S to the pole. With a network as thin as this only a very basic understanding of the ozonosphere in the Southern Hemisphere exists and this has primarily come from the Australian network of five stations. The following maps (Figs. 4.213.1a-d) permit a first look at the longitudinal variations, the long-wave pattern, and the gradient of total ozone in the Southern Hemisphere.

In April a 'tight' gradient is located approximately along the 100th (E)

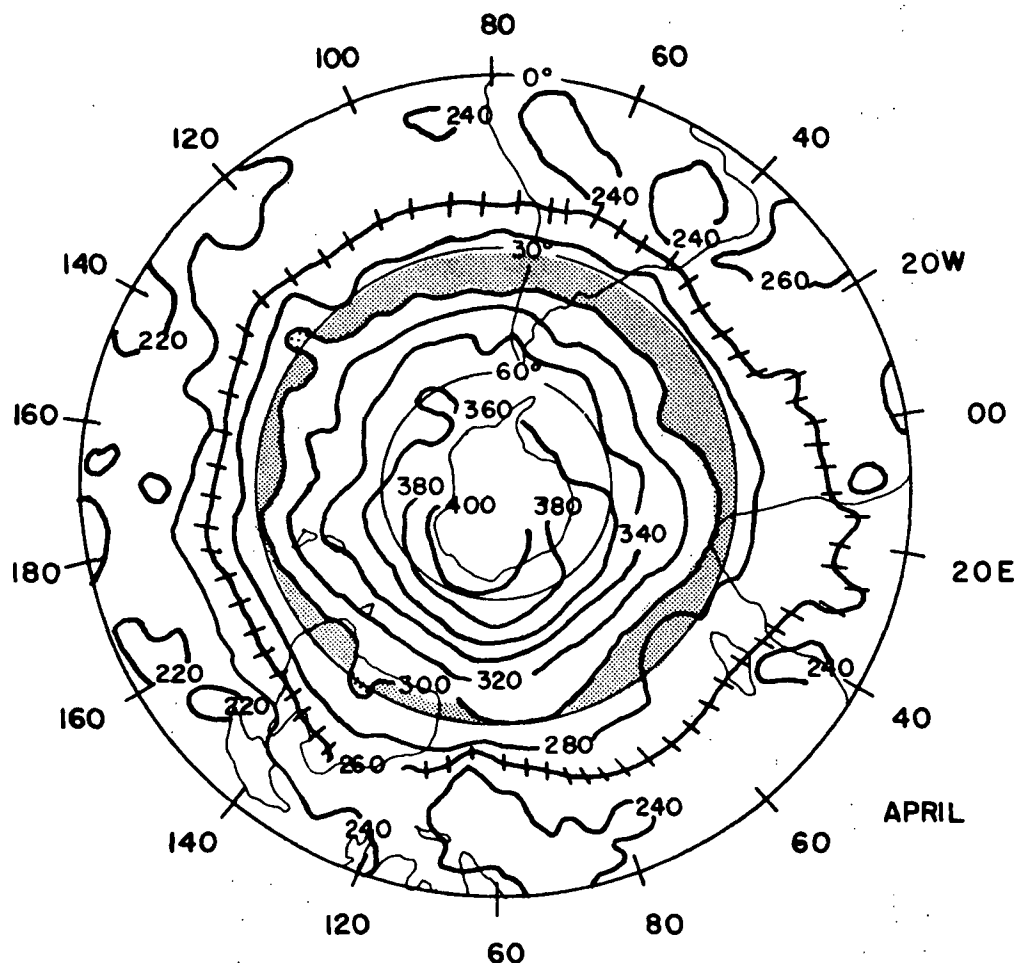


Fig. 4.213.1a Same as 4.211.1a except for April 1969, Southern Hemisphere.

meridian between 40 and 50°S. This gradient weakens considerably in May but reappears and intensifies again in June and July. In May there are two regions of strong meridional O_3 gradients - one over the eastern Atlantic and the other over the eastern Indian Ocean. The gradients over both these regions are somewhat less than the gradient southwest of Australia mentioned above. In June the strong gradient southwest of Australia is again evident. There is another region of tightly-spaced

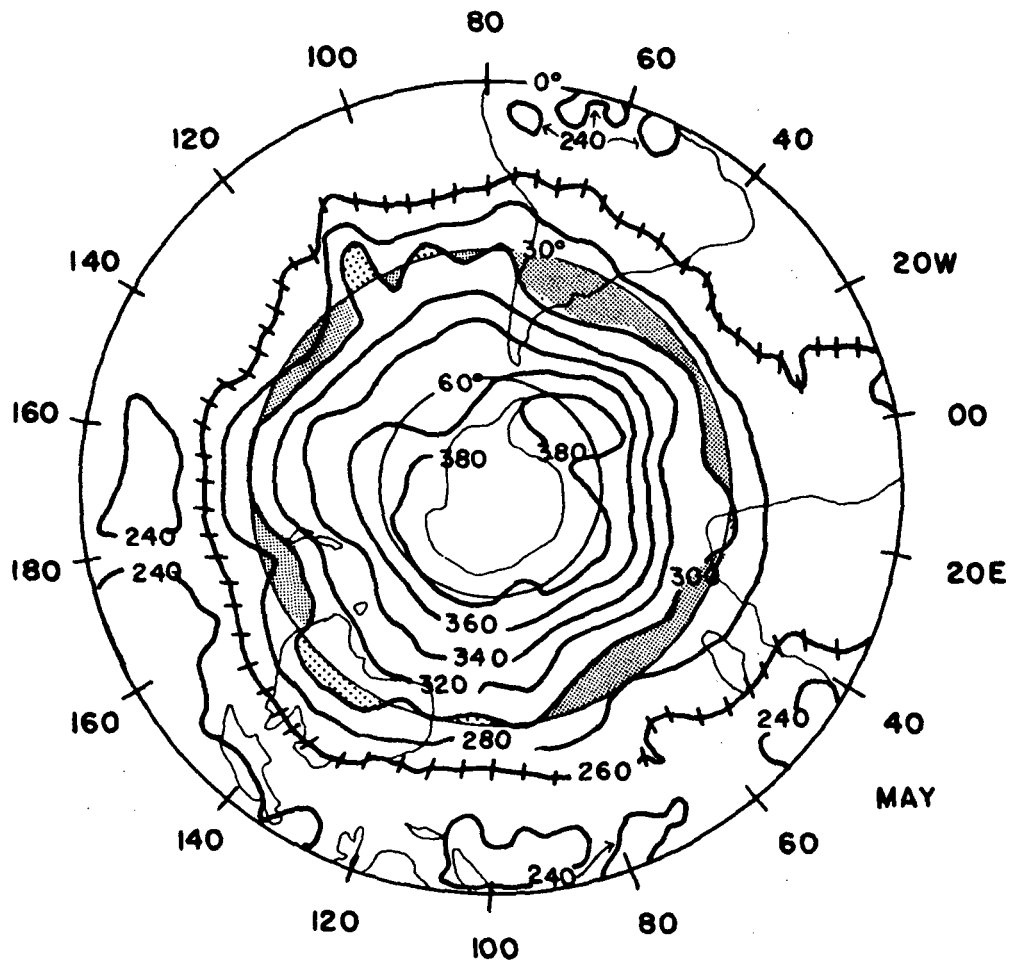


Fig. 4.213.1b Same as 4.211.1a except for May 1969, Southern Hemisphere.

contours in the south central Pacific Ocean. In July we find both of the features remaining in essentially the same locations. Van Loon (1964) reports a broad westerly wind maximum at $45-50^{\circ}\text{S}$ from $45-100^{\circ}\text{E}$. This is in more-or-less general agreement with the ozone gradients in this region. The closely spaced ozone contours from $140-160^{\circ}\text{W}$ between 25 and 40°S would indicate a mean wind maximum is located in this region.

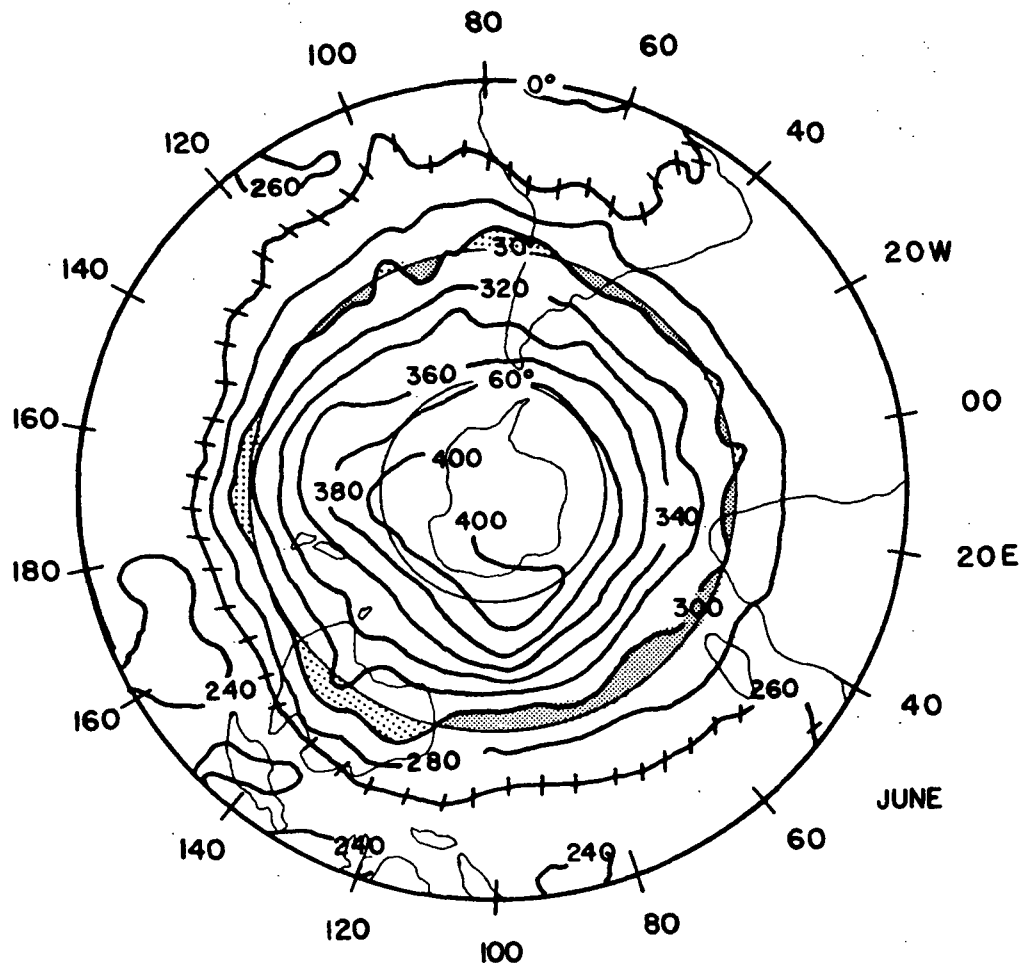


Fig. 4.213.1c Same as 4.211.1a except for June 1969, Southern Hemisphere.

This is a region of the earth about which little upper atmosphere wind data have been published. The use of total ozone gradients to locate systems of this extent may be of considerable worth in the understanding of the general circulation characteristics of the Southern Hemisphere.

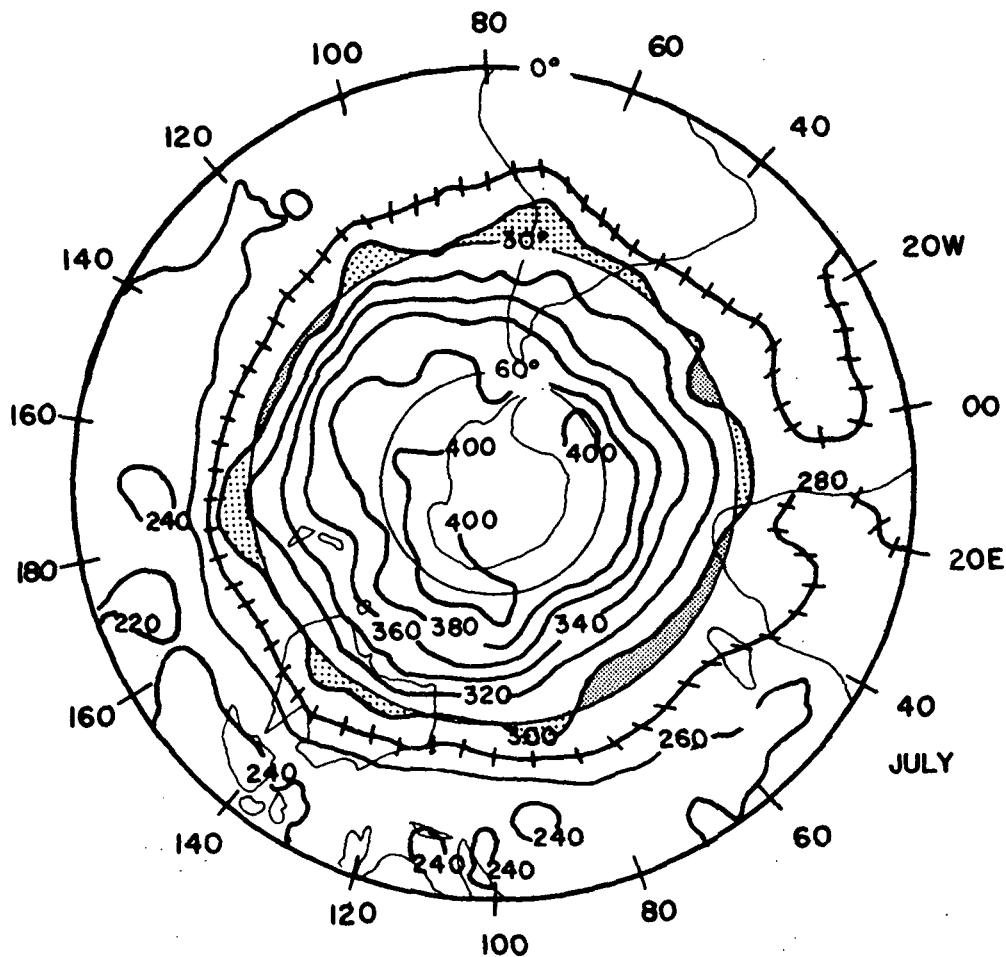


Fig. 4.213.1d Same as 4.211.1a except for July 1969, Southern Hemisphere.

The gradient southwest of Australia is nearly as strong in April as it is three months later in July, the middle of the Southern Hemisphere winter. One might infer from this that the jet stream system over this region is nearly of the same velocity in the late summer as in the middle of winter. This would support the statements on Southern Hemispheric

jet streams made in Chapter 4.2. The ozone contours indicate that the jet stream moves slowly northward from April to July as observed from wind analyses.

In the Southern Hemisphere from April to July the ozone isoline pattern is arranged in a pattern of four to five planetary waves. This is similar to the wave pattern we observed in the Northern Hemisphere. At least for the four months discussed in this paper, there appears to be four 'anchor' locations for the "ozone troughs": 100°E , 175°W , 100°W , and a broad area in the South Atlantic. The latter location is ill-defined and variable on all mean maps.

In April we see essentially that all of the 300 m.atm.cm contour is south of 30°S . The only exceptions to this are small areas over south central Australia and in the south central Pacific. This pattern appears to be typical for the Southern Hemisphere in early fall. The variation in the oscillation of the 300 m.atm.cm contour about latitude 30°S is less in the Southern Hemisphere than in the Northern Hemisphere. Peculiar seasonal variations of total ozone are indicated over Australia. In April a small positive anomaly is found over this continent. In May this small area of maximum ozone has expanded and now covers over half of the width of the continent (Fig. 4.213.1b). By June the extension is complete and the 300 m.atm.cm contour lies north of 30°S over the entire continent. In July the positive anomaly shrinks slightly, but extends further westward. During this entire period (April to July) the total ozone at 105°E and 30°S has shown in essence no variance. The increase of total ozone over Australia, as winter approaches, seems to correspond to a decrease of total ozone over the North American Continent as summer approaches.

One other area with an anomalous maximum should be noted. In May

the 300 m·atm·cm contour has a slight 'bulge' to the north of 30°S off the west coast of South America (Fig. 4.213.1b). By July this maximum has extended to 20°S and covers all of the extreme southern part of South America. A final region noteworthy of mention is the western part of the Indian Ocean. Over this entire region an ozone minimum is reflected in the 300 m·atm·cm contour.

The 260 m·atm·cm contours in April, May, and June (280 m·atm·cm in July) indicate relative high total ozone concentrations in the tropical latitudes over Africa and the eastern Atlantic Ocean.

Basic similarities of the distribution of total ozone in the Northern and Southern Hemispheres are the following: Both hemispheres show: (1) a preference for a four wave ozone pattern; (2) 'tight' ozone gradients which, we hypothesized, are directly related to jet stream system; (3) a general increase (decrease) of the ozone at a given latitude as we progress toward the winter (summer) season; (4) regions of relatively high ozone concentration in the tropics over the eastern Atlantic Ocean and the African Continent.

Basic dissimilarities in the distribution of total ozone are the following: (1) whereas two and occasionally three regions of 'tight' ozone gradients were observed over the Northern Hemisphere, two and sometimes only one such region could be seen over the Southern Hemisphere. This difference may partly be based on the fact that different seasons in each hemisphere are being compared. This should be remedied when NIMBUS IV data become available for a complete year; (2) there are larger variations of total ozone at a given latitude in the Northern Hemisphere. This may also be due to the out-of-phase seasonal comparisons.

4.3 The Longitudinal Progression of Ozone 'Waves'

4.31 The Variation of Total Ozone at 60°S for 17 Days in May 1969

Figure 4.31 shows a time-longitude distribution of total ozone for 60°S. This particular latitude was selected so that comparisons could be made with radiance values that were computed for the first two-thirds of May by Fritz (1970).

4.311 A Comparison of Radiance and Ozone Waves

Fritz's computations were for $\nu = 669.3 \text{ cm}^{-1}$. At this particular wavenumber he was measuring the radiance value of the high stratosphere. Ninety per cent of the flux which arrives at the satellite comes from above 100 mb (Fritz, 1970). This is a good frequency at which to observe and compare ozone variations, because it is centered in a region of the stratosphere between 20 and 50 mb in which a large percentage of the total ozone is concentrated.

Upon examination of Figure 4.31 several features are readily apparent. Both maxima and minima of ozone progress steadily to the east. Fritz describes the maxima and minima of radiance values as 'waves'. This seems to be appropriate here as well. These ozone 'waves' move in the same direction as the radiance 'waves' described by Fritz (1970). Fritz's low (high) radiance values correspond to low (high) stratospheric temperatures. His locations of high and low stratospheric temperatures are indicated by w and c, respectively, in Figure 4.31. Note that warm stratospheric temperatures correspond fairly well with high concentrations of ozone. Low ozone values seem to agree with cold stratospheric temperatures. This correspondence has been shown from earlier balloon-borne ozonesonde packages (Craig, 1965; Lovill and Miller, 1968).

4.312 Progression Rates of Eastward Moving Ozone 'Waves'

The light lines in Figure 4.31 sloping to the right with time are

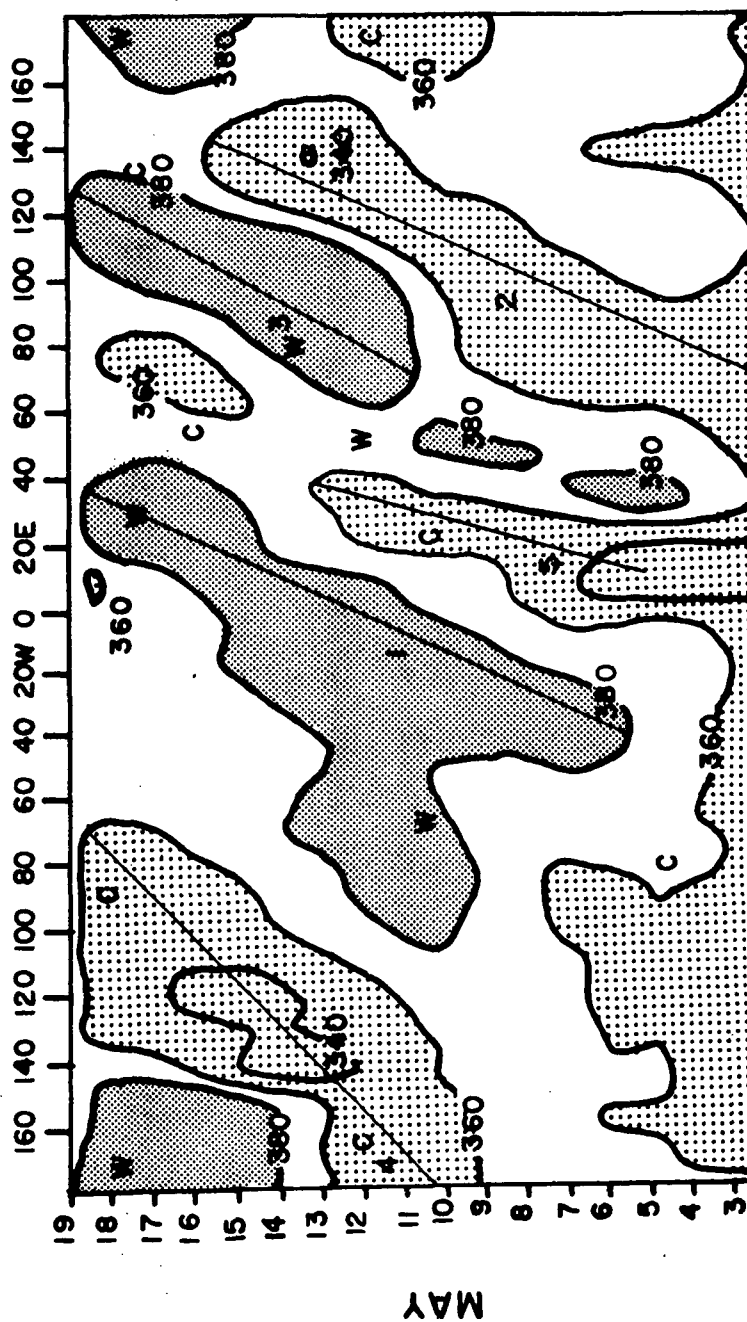


Fig. 4.31. Time-longitude graph of the total ozone at 60°S for May 1969. Total ozone values are in m-atm.cm. The W and C symbols represent regions of warm and cold stratospheric temperatures according to Fritz (1970). The straight lines represent the average tilt in time with longitude of the respective ozone 'waves'.

indications of the rate of eastward movement of the 'ozone waves'. Each line has a number associated with it. The average rate of longitude movement for each wave is indicated in Table 4.312.

Table 4.312

Eastward Progression Rate of Total Ozone 'Waves' at
60°S for the Period 3-19 May 1969

Wave Number	Progression Rate (Degrees of Longitude/Day)	Average Concentration of Ozone Within Wave (m.atm.cm)
1	5.6	380
2	5.7	350
3	7.1	380
4	13.3	350
5	3.8	360

The variability of the longitudinal progression of these waves is quite large, ranging from 3.8 to 13.3 degree longitude day⁻¹, with an average movement of 7 degrees longitude day⁻¹. Additional studies of this type should help relate stratospheric ozone variations to thermal fluctuations, and this in turn should promote a better understanding of the dynamics of the stratosphere.

4.32 Hemispherical Differences in Longitudinal Progression During June 1969

Figures 4.32.1 to 4.32.6 represent time-longitude variations of total ozone at 60°S, 40°S, 20°S, the Equator, 20°N, and 40°N, respectively. These figures are presented in order to indicate the rapid eastward movement of dynamically active ozone maxima and minima in the winter hemisphere and the rather slow movement of these centers in the summer hemisphere and near the equator.

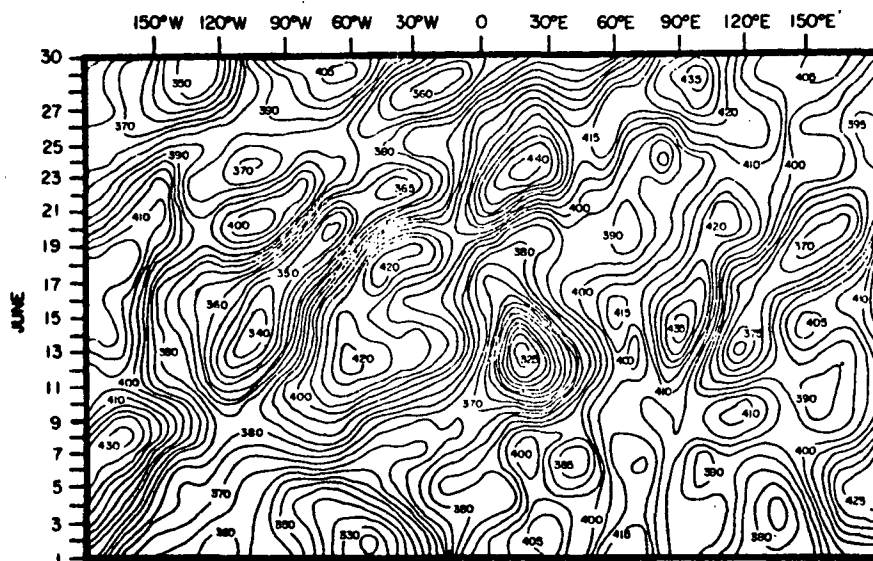


Fig. 4.32.1. Time-longitude variations of the total ozone (m.atm.cm) during June 1969 at 60°S.

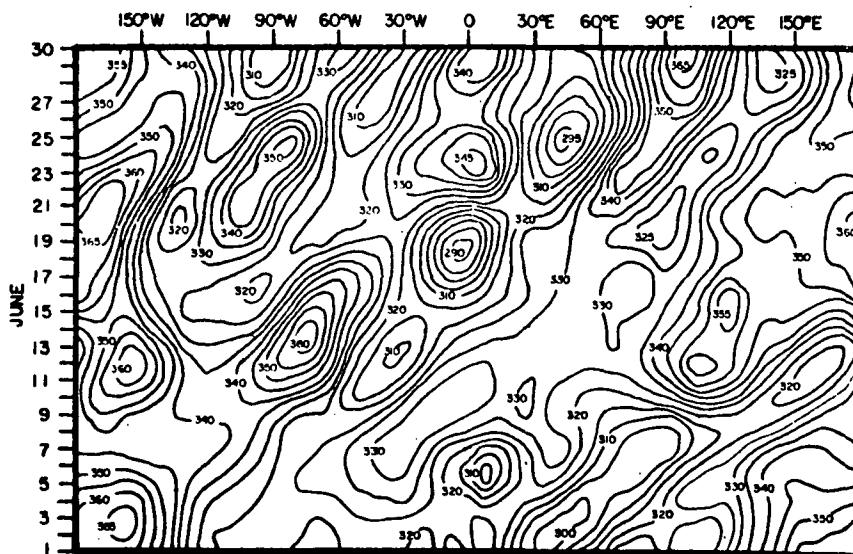


Fig. 4.32.2. The same as Figure 4.32.1, except 40°S.

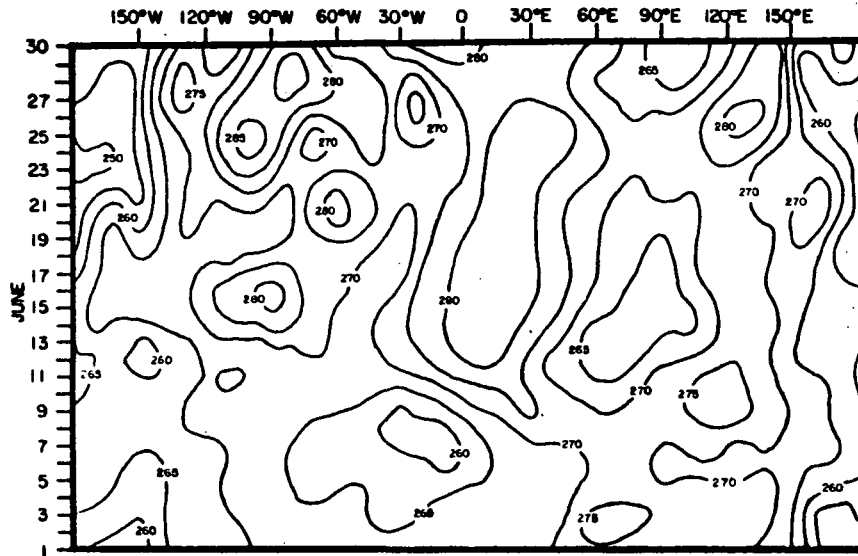


Fig. 4.32.3. The same as Figure 4.32.1, except 20°S.

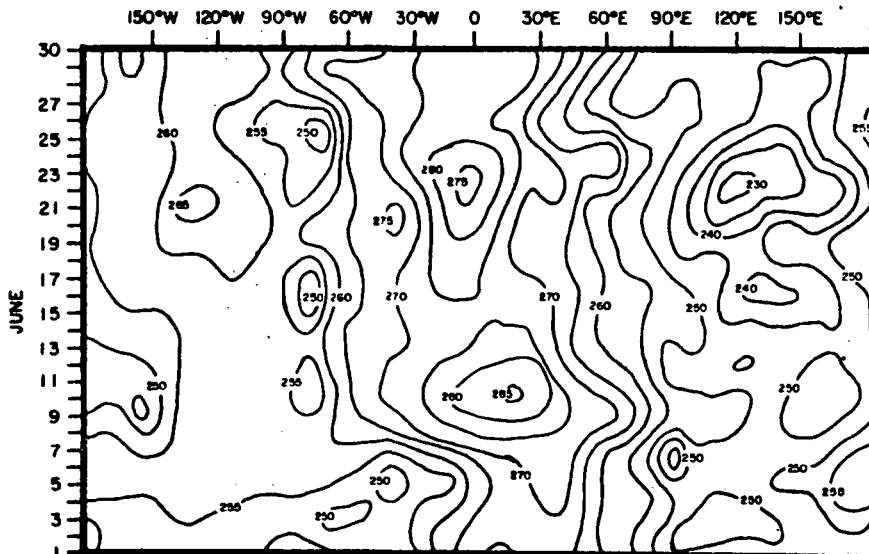


Fig. 4.32.4. The same as Figure 4.32.1, except the Equator.



Ff



F1

The data in Figures 4.32.1 to 4.32.6 for June 1969 represent the first possible analysis of longitudinal variations of total ozone on a fine day-by-day grid. The best data of the longitudinal distribution of total ozone from surface stations in the past have been at the mid-latitudes in the Northern Hemisphere. These data at best raised more questions than they answered. The data on the preceeding pages represent a solid data bank that extends around the earth over unpopulated areas from the equator to high latitudes.

Several facts are demonstrated quite early in these figures. Firstly, one can see that the speed at which the 'waves' progress eastward is greater in the winter hemisphere (here the Southern Hemisphere). Secondly, the speed of eastward progression decreases as one approaches the lower latitudes in the winter hemisphere (see Figs. 4.32.1-4.32.3). Thirdly, the intensity of the waves, as seen from the contouring intervals, increases as one goes toward the pole in the winter hemisphere. Finally, in the equatorial region and in the Northern Hemisphere (Figs. 4.32.4-4.32.6) there is not a strong eastward progression of waves. Any eastward progression at best, is only weak and sometimes is even replaced by westward progression.

The movements of the ozone 'waves' are of course closely related to winds in the upper atmosphere. Thus, one observes a strong flow from the west in the winter season in the Southern Hemisphere. In the summer in the Northern Hemisphere the flow aloft is variable and generally very weak. In the equatorial regions Figure 4.31.4 suggests a wind component from the east. The ozone 'waves' progress eastward at rates as high as $>15^{\circ}$ longitude/day at high latitudes in the Southern Hemisphere (see Fig. 4.21.1). However, near the equator and at 20°N (Figs. 4.31.4-4.31.5) a westward movement as high as 3° longitude/day may be observed.

A final interesting item to mention in relation to these 'waves' is that as one attempts to follow them in time, one sees that they change intensity continuously. A good example of this phenomenon is seen in Figure 4.31.2 which is the fluctuation at 40°S : One may identify a 'wave' maximum that begins on 1 June at approximately 160°W and follow it to 30 June at 10°E . During this time interval the 'wave' progressed 170° eastward halfway around the globe. This is an average progression rate of 5.7° longitude/day. During the interval one can observe that this maximum 'wave' ranged from a high value of 380 m·atm·cm on 13 June to a low value of 320 m·atm·cm seven days later. As one follows the 'wave' during these decreases and increases, it is also readily seen that the progression rate changes just as erratically as the total ozone concentration. These temporal fluctuations are related to the motion of dynamic stratospheric systems. The 'tighter' ozone gradients, which may be seen in the winter hemisphere set of figures (Figs. 4.32.1-4.32.3), are associated with the stronger stratospheric baroclinic zones (see Chapter 3) which are moving eastward.

4.4 Average Variation of Total Ozone with Latitude

Figure 4.4 represents the monthly total ozone distribution in the Southern Hemisphere. London (1963), basing his analysis on the ozone data available through 1959, arrived at an average curve for the spring that extended from the equator to the North Pole. His curve is plotted in Figure 4.4. Notice the remarkable agreement between his total ozone average curve for the spring and the average IRIS curves for months April and May. Notice also that his summer curve is consider-

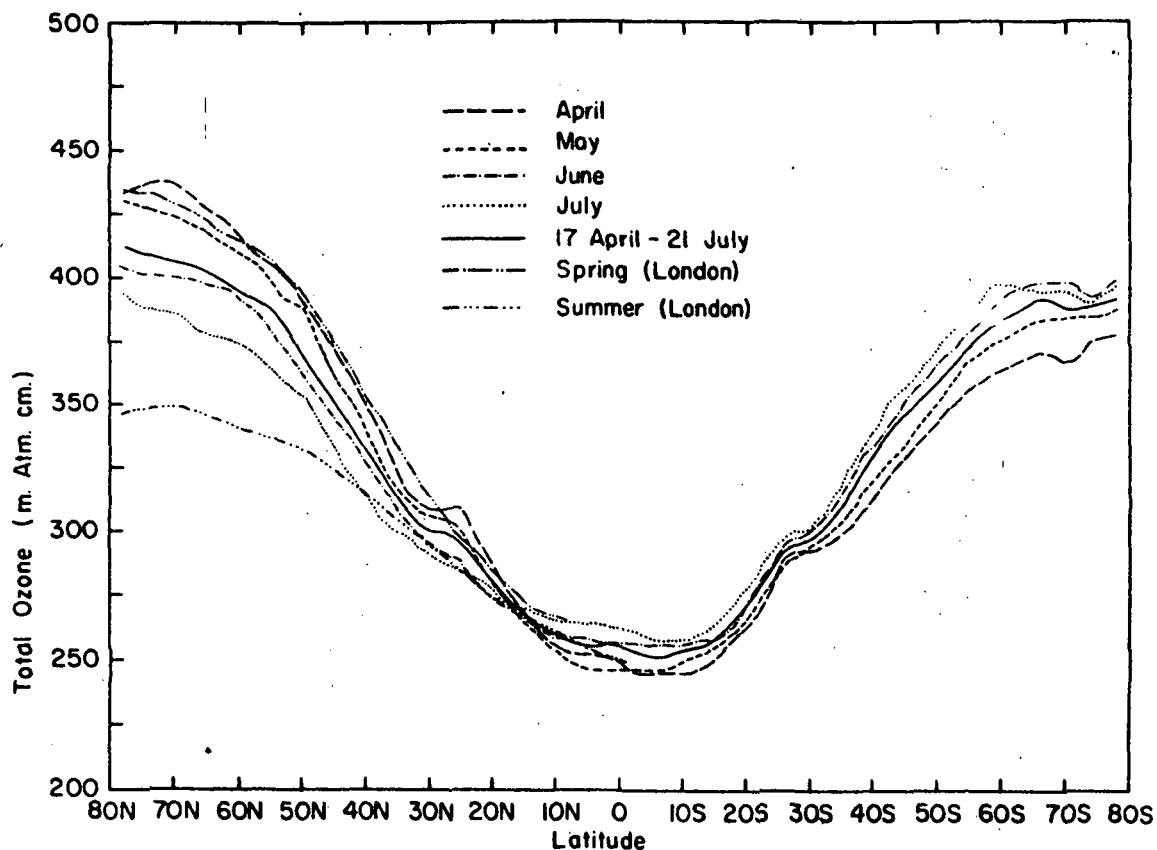


Fig. 4.4. The variation of total ozone with latitude, from 80°N to 80°S for April, May, June and July 1969.

ably lower than the curve for July from IRIS. This might indicate that during July 1969 there was an anomalously high ozone amount at the latitudes compared. The total number of ozone data points used to construct the April-July line was 1.8×10^5 . Mean total ozone is given for the months of April, May, June, and July as well. Immediately evident from Figure 4.4 are increasing ozone values from the equatorial region to the poles in each month.

The largest gradient of total ozone is clearly found in the middle latitudes (35-50°N) in the Northern Hemisphere. The location of the

steepest gradient in the Southern Hemisphere is not as well defined. Two preferred areas are indicated there. One is in the subtropics from $20-25^{\circ}\text{S}$. The other is from approximately $30-40^{\circ}\text{S}$. The former may be influenced by the change in regression coefficients used in the calculations. A slope of similar steepness, perhaps also somewhat biased by the regression coefficients, appears in the curve from April at $18-25^{\circ}\text{N}$.

Seasonal variation of total ozone is smallest in the tropics. In the Northern Hemisphere this occurs at 15°N , in the Southern Hemisphere at $20-30^{\circ}\text{S}$. The latter location may be influenced to a certain extent by the regression coefficient changeover, but nevertheless it is felt that the smallest variation is in this $20-30^{\circ}\text{S}$ latitude band.

Another interesting feature of the figure is that the minimum ozone values for all latitudes for all four months investigated are found between 5 and 10°S . It will be very interesting to see how this minimum migrates during the other months when Nimbus IV data are analyzed.

In the Northern Hemisphere the total ozone in April reaches a peak at 70°N ; this corresponds fairly well with London's (1963) winter peak at $60-65^{\circ}\text{N}$, but not at all with his curve for spring. In the Southern Hemisphere June and July have peaks at 68°S and 60°S , respectively. April has a secondary peak at 66°S and presumably another one south of 78°S . The unusual feature of an ozone minimum

value at 70°S is difficult to explain unless it is due to an anomalous standing-wave situation near Antarctica.

Several important facts have been elaborated upon in Figure 4.4:

(1) for the first time the average distribution of ozone with latitude has been determined by satellite for a period of several months; (2) the distribution agrees very well with the data from the long-term data base in the Northern Hemisphere; (3) the latitudinal ozone distribution, for the first time, has been described during the autumn and winter in the Southern Hemisphere; (4) the smallest variation of ozone from spring to summer was seen at 15°N ; (5) the lowest mean ozone value for the period was at 6°S .

4.5 The Global Distribution of Ozone from 19 April to 21 July 1969

The average distribution of total ozone for the Northern and Southern Hemispheres from 19 April to 21 July 1969 is given in Figures 4.5.1 and 4.5.2. The Northern Hemisphere analysis was computer analyzed using 0.83×10^5 total ozone data points. The Southern Hemisphere analysis used 1.01×10^5 points.

Several interesting features in the total ozone distribution are seen in these average global maps. A large region of low total ozone ($< 240 \text{ m}\cdot\text{atm}\cdot\text{cm}$), 10 to 20 degrees on either side of the equator is observed to extend from southeast Asia eastward to the central Pacific. One region of several thousand square kilometers extent (160°E , 10°S) has values less than $220 \text{ m}\cdot\text{atm}\cdot\text{cm}$. Climatological surveys of this region in the western equatorial Pacific have shown anomalously high

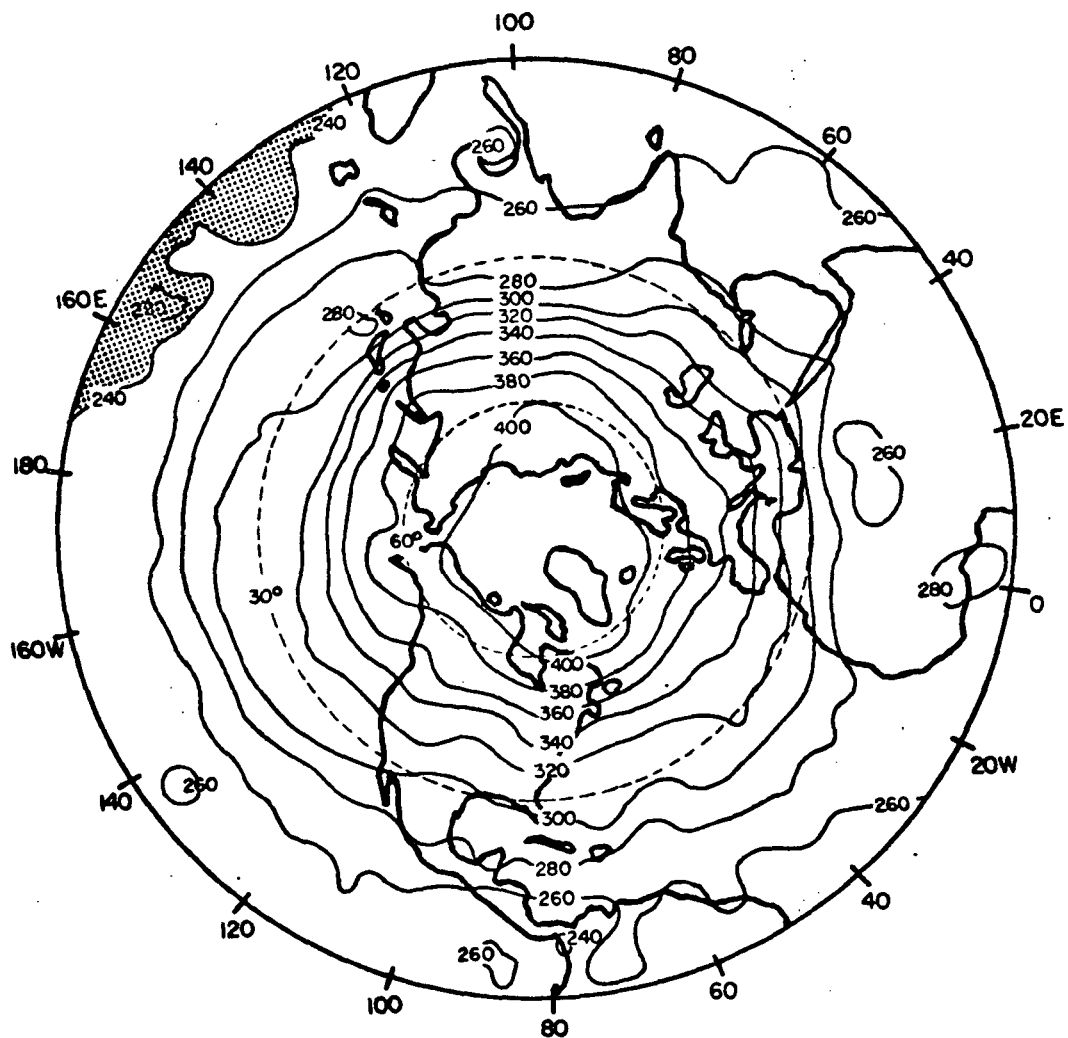


Fig. 4.5.1. The average distribution of total ozone (m·atm·cm) for the Northern Hemisphere from 19 April to 21 July 1969. Shading represents total ozone values less than 240 m·atm·cm.

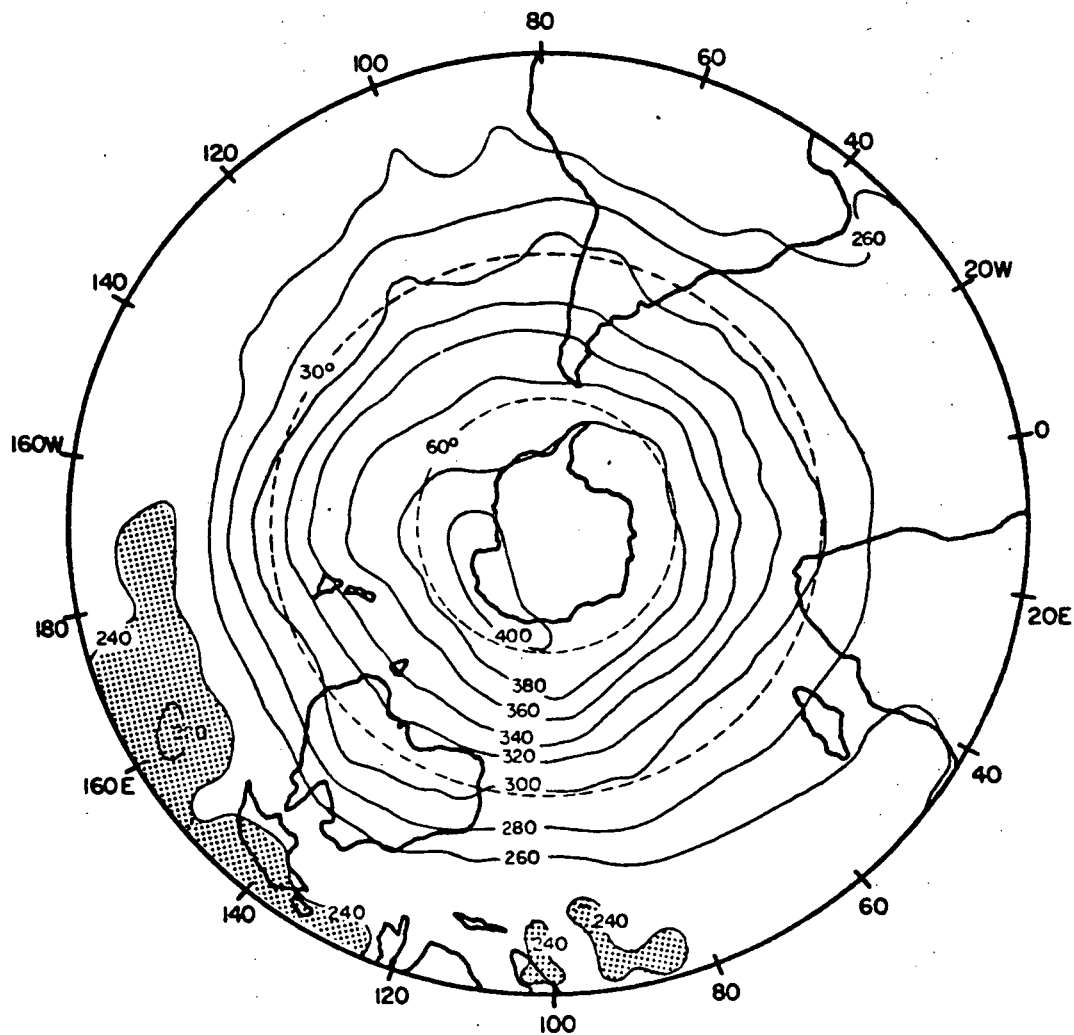


Fig. 4.5.2. The average distribution of total ozone (m·atm·cm) for the Southern Hemisphere from 19 April to 21 July 1969. Shading represents total ozone values less than 240 m·atm·cm.

amounts of low-level cloudiness and precipitation (see the work of Budyko (1963) on the anomalous heat balance in this area). From earlier satellite studies Vonder Haar and Suomi (1971) have shown that this same region also has an anomalously high albedo. This would correlate well with the high amount of cloudiness. The manner by which this correlates with low total ozone concentrations is not at all clear, since most of the daily and seasonal change in total ozone occurs in the stratosphere (Craig, 1965; Lovill and Miller, 1968). There is a possibility that on the large-scale this region is subject to a stratospheric cell that allows for generally ascending motions and horizontal out-flux of stratospheric ozone from the area. When a complete understanding of the mechanism in this anomalous ozone region is reached, it will probably not deviate far from the above speculation, for this is obviously not a problem of photochemistry alone but one of atmospheric dynamics.

A region of anomalously high total ozone in the tropics is seen to extend from the western Atlantic eastward across Africa to the western Indian Ocean. This region extends into both hemispheres. This area of relatively high total ozone may be associated by some interconnected mechanism with the anomalously low total ozone region over southeast Asia which is also in the tropical latitudes.

Both the Northern and Southern Hemispheres appear to provide 'anchoring' mechanisms for ozone ridges (high ozone amounts). The most predominant of these ridges is also usually associated with a 'tight' ozone gradient. In the Northern Hemisphere these locations are eastern North America, central Europe, western Asia, and eastern Asia. The ridge over the Soviet Union appears to be the weakest of the four ridges.

In the Southern Hemisphere ridges are evident over the east Indian Ocean, the central Pacific Ocean and the eastern Atlantic. In general the ridge pattern is easier to delineate in the Southern Hemisphere than in the Northern Hemisphere. This may be due to a basic difference in the general circulation of the Southern Hemisphere or to the time period over which the data are analyzed. Certainly some of the difference is attributable to the stronger winter circulation in the Southern Hemisphere as compared to the weaker summer circulation in the Northern Hemisphere.

The 'tightest' gradient of total ozone in either hemisphere is seen over Japan (Fig. 4.5.1). This correlates closely with the anomalously high frequency of jet stream winds usually observed over the Japanese Islands. In the Southern Hemisphere the most tightly packed ozone contours are observed over the eastern Indian Ocean. Another closely spaced group of ozone contours is seen over the Pacific Ocean, from approximately 110°W to 170°W , near latitude 35°S . These locations in the Southern Hemisphere should coincide with the highest mean winds in the upper troposphere and stratosphere during the period of investigation (refer to section 4.21).

A closed center of high total ozone content ($400 \text{ m}\cdot\text{atm}\cdot\text{cm}$) is seen in Figure 4.5.2 over the Australian sector of Antarctica.

An average global value of the total ozone for the period from 19 April to 21 July 1969 was calculated to be $330.3 \text{ m}\cdot\text{atm}\cdot\text{cm}$.

4.6 Spectral Analyses of Ozone and Wind Variability

Daily maps of the global distribution of total ozone were produced for the period from 19 April to 21 July 1969. Since only ninety-four days of IRIS ozone data are available at the present time, a data ensemble was constructed with 20° longitude intervals at various latitudes in the

Northern Hemisphere. In this manner a total of 1692 'unfolded days' of data were useable for spectral analysis. In a similar manner NMC 250 mb wind data were analysed for the same period.

Two examples of the spectra obtained at 50°N are presented in Figures 4.6.1 and 4.6.2. Figure 4.6.1 shows the spectral analysis of total ozone. A definite spectral peak is seen at a frequency of one cycle per 12.2 days. Figure 4.6.2 represents the spectral analysis of the 250 mb wind component. A spectral peak is also seen in this analysis occurring at one cycle per 12.2 days. A cross-spectral analysis of the total ozone and wind velocity was processed for several of the Northern Hemisphere latitudes. Table 4.6 presents these results.

Table 4.6

Periods at selected latitudes where the
coherence-squared value is a maximum.

Latitude	Period (Peaks) Days	Coherence ²
30 N	14.2	0.17
40 N	12.2	0.14
50 N	12.2	0.36
60 N	43.0	0.22
70 N	8.3	0.26

An examination of Table 4.6 reveals that the 12.2 day periodicity at 50°N of both the total ozone and the 250 mb wind velocity has a coherence-squared statistic of 0.36. This indicates that the two parameters are significantly related at periodicity of slightly less than once per two weeks. It is worthy to note that similar periodicities (with lesser coherence-squared values) exist also at the lower latitudes - 30 and 40°N (Table 4.6). This is certainly a distinct suggestion

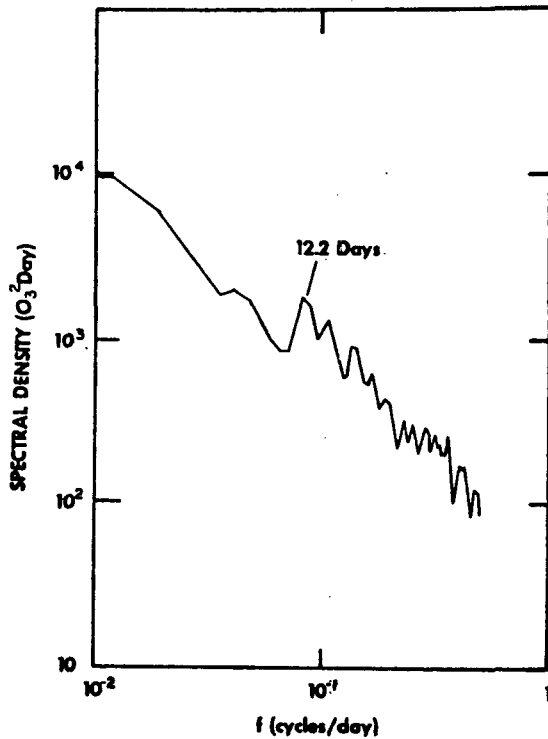


Fig. 4.6.1. Spectra of the total ozone at 50°N from 21 April to 21 July 1969.

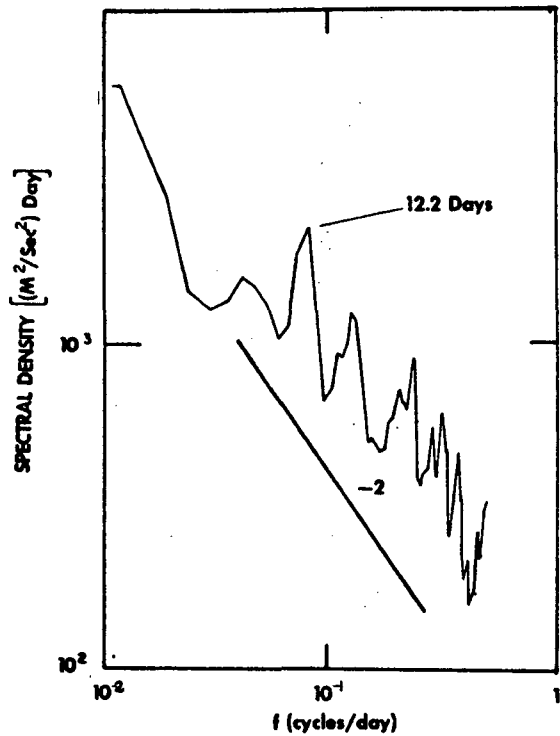


Fig. 4.6.2. The same as Figure 4.6.1 except 250 mb wind velocity. The -2 line indicates the slope of the k^{-2} exponential function.

that ozone maxima are occurring simultaneously with upper atmosphere wind maxima at a significant number of grid locations in the middle and upper latitudes of the Northern Hemisphere (at least during the late spring and early summer of 1969).

5.0 Summary and Conclusions

Studies in recent years have shown distinct differences of the atmospheric general circulation of the Northern and Southern Hemispheres. Earlier publications postulated a more zonal flow in the Southern Hemisphere supposedly because of less land mass and fewer mountain massifs. More recent investigations show that such statements need to be qualified.

Wooldridge and Reiter (1970) have shown that significantly stronger horizontal anisotropy of flow prevails at cyclone wavelengths in the Southern Hemisphere than in the Northern Hemisphere. In the Southern Hemisphere meridional perturbations exceed zonal flow perturbations. Eulerian spectral densities of the zonal component in the Southern Hemisphere were seen to be only half of those in the Northern Hemisphere. This would seem to imply that there is less zonal energy at cyclone-wave frequencies in the Southern than in the Northern Hemisphere. This may occur because of a lack of orographically induced planetary longwaves in the Southern Hemisphere that are superimposed upon the hemispheric jet stream zones. Apparently the relatively zonal character of the Southern Hemisphere pertains to the long planetary-scale waves only.

Interest in global total ozone measurements is widespread and increasing. The paucity of total ozone measuring stations over the oceans and in the tropics in the Northern Hemisphere and throughout the Southern Hemisphere has greatly hindered a complete understanding of the role that stratospheric ozone plays in the general circulation processes of the atmosphere. With total ozone sensors (such as the

IRIS instrument) on earth-orbiting satellites the ozone over the entire earth is measured daily. The conclusions of some of the analysis from the first satellite (Nimbus III) capable of these measurements follow.

A statistical analysis of the total ozone data for two days indicated that average standard error between data obtained by the inversion technique and data obtained by regression coefficients was only 3.7 percent. When surface total ozone measurements were compared with regression data at monthly intervals a standard error of 3.6 percent was seen.

A strong correlation was discovered between the meridional gradient of total ozone and the wind velocity in jet stream systems. A graph has been constructed which will allow the computation of the wind velocity at 250 mb if the total ozone distribution in the vicinity is known. This should be a very useful relation to apply over the oceanic regions of the Northern Hemisphere and throughout the entire Southern Hemisphere. Wind velocities at jet aircraft operation levels could then be forecasted by consulting the daily satellite total ozone analysis.

A study of the total ozone distribution over a Pacific Ocean extra-tropical cyclone and its associated jet stream indicated large vertical motions and strong horizontal advective processes were present near this system. Large amounts of total ozone were measured immediately behind the system and low amounts in front which were indicative of air rich in ozone moving southward and downward behind the system and air poor in ozone moving northward and upward in front of the storm.

Time-longitude variations of the total ozone for several latitudes in the Northern and Southern Hemisphere for June 1969 were analyzed. Several interesting facts were seen in these results. Firstly, one can observe that the speed at which the 'waves' progress eastward is greater in the winter hemisphere (here the Southern Hemisphere). Secondly, the speed of eastward progression decreases as one approaches the lower latitudes in the winter hemisphere. Thirdly, in the equatorial region and in the Northern Hemisphere there is not a strong eastward progression of 'waves' but at best only weak eastward movement. Progression rates as high as fifteen degrees of longitude per day were seen at the high latitudes in the Southern Hemisphere. As one follows the 'waves' in time, continuous changes in intensity are observed.

When total ozone data for the period of observation are plotted against latitude for the various months the following is indicated. For the first time the average distribution of ozone has been described during the autumn and winter at close intervals, both temporally and spatially, in the Southern Hemisphere. The smallest variation of total ozone from spring to summer was seen at 15°N . The lowest mean total ozone value for the globe was at 6°S .

When two maps were prepared describing the distribution of total ozone for the entire period for the Northern and Southern Hemispheres, the following was seen. Closely spaced total ozone isolines appear to have revealed a reasonably strong jet stream west of South America at approximately 35°S . This system, at least at the intensity indicated by the total ozone gradient, has gone more-or-less unnoticed in the past.

Additionally, a large region of low total ozone was observed in the tropics, extending from southeast Asia eastward to the central Pacific. Earlier studies have indicated that this region also has an anomalously high albedo. The manner by which this correlates with low total ozone concentrations is not at all clear.

Both the Northern and Southern Hemispheres appear to provide 'anchoring' mechanisms for total ozone ridges. The most predominant of the ridges is also usually associated with a 'tight' ozone gradient. In the Northern Hemisphere these locations are eastern North America, central Europe, western Asia, and eastern Asia. The ridge over the Soviet Union appears to be the weakest of the four ridges. In the Southern Hemisphere 'ozone' ridges are evident over the east Indian Ocean, the central Pacific Ocean and the eastern Atlantic. In general, the ridge pattern is easier to delineate in the Southern Hemisphere than in the Northern Hemisphere.

The 'tightest' gradient of total ozone in either hemisphere was seen over Japan. This correlates closely with the high frequency of jet streams observed over the region.

An average global value of the total ozone for the entire period was calculated to be ^{330.3} ~~330.3~~ m.atm.cm.

5.1 Suggestions for Future Research

The results presented in this paper represent a significant advance of our knowledge toward a better understanding of the manner in which ozone is involved in depicting both the large- and small-scale motions of the atmosphere. Future work in this area should take advantage of the ever-improving instrumentation on current and future satellites in order to improve global coverage. Many of the results can be significantly amplified in detail when the Nimbus IV IRIS data are released. All four seasons in both hemispheres will then be available for analysis and comparison. We should be able to determine accurately variations in location and strength of major motion systems in the atmosphere, such as jet streams, cyclones, and anticyclones. More proof will be offered, for example, to investigators who have suggested that stronger horizontal anisotropy of flow prevails at cyclone wavelengths in the Southern Hemisphere rather than in the Northern Hemisphere. The techniques developed in this paper should be useful for the analysis of data not only from earth-orbiting satellites but from those orbiting other planets, such as the current Martian probe by the Mariner 9 IRIS experiment.

REFERENCES

- Allison, L.J., C. Prabhakara and J. Steranka, 1971: Variations of atmospheric ozone from Nimbus 3 IRIS data over Hurricane Bernice, 1969. Presented at the 52nd Annual Meeting of the American Geophysical Union, Washington, D.C., 12 - 16 April, 1971.
- Blackman, R.B., and J.W. Tukey, 1958: The measurement of power spectra, Dover Publications, New York, 109 pp.
- Bojkov, R.D., 1969: Differences in Dobson spectrophotometer and filter ozonometer measurements of total ozone, J. Appl. Meteorol., 8, 362-368.
- _____, and J.E. Lovill, 1969: Comments on Spring warming-transfer processes in the lower Antarctic stratosphere, Tellus, 21, 284.
- Brewer, A.W., and J.R. Milford, 1960: The Oxford-Kew ozonesonde, Proc. Roy. Soc., A256, 470-495.
- Briggs, J., and W.T. Roach, 1963: Aircraft observations near jet streams, Quart. J. Roy. Meteorol. Soc., 89, 225-247.
- Budyko, M.I., 1963: Atlas of the heat balance of the globe (in Russian). Moscow, Hydrometeorological Service, 69 pp.
- Cadle, R.D., and Margaret Ledford, 1966: The reaction of ozone with hydrogen sulfide, Intern. J. Air and Water Pollution, 10, 25-30.
- Chapman, S., 1930: A theory of upper atmospheric ozone, Quart. J. Roy. Meteorol. Soc., 3, 103.
- Cooley, J.W., and J.W. Tuckey, 1965: An algorithm for the machine calculation of complex fourier series, Math. of Computation, 19, 297-301.
- Craig, R.A., 1950: The observations and photochemistry of atmospheric ozone and their meteorological significance, Meteor. Monogr. 1, No. 2, 1-50.
- _____, 1965: The Upper Atmosphere. Meteorology and Physics, International Geophysics Series, Vol. 8, Academic Press, New York, 509 pp.
- Crutzen, P.J., 1971: Ozone production rates in an oxygen-hydrogen-nitrogen oxide atmosphere. Preprint. 53 pp. To appear in J. of Geophys. Research.
- Dobson, G.M.B., 1930: Observations of the amount of ozone in the earth's atmosphere, and its relation to other geophysical conditions, part IV, Proc. Roy. Soc., A129, 411-433.

- Dobson, G.M.B., 1931: A photoelectric spectrophotometer for measuring the amount of atmospheric ozone, Proc. Phys. Soc., 43, 324-339.
- Dutsch, H.U., 1946: Photochemische Theorie des atmosphärischen Ozons unter Berücksichtigung von Nichtgleichgewichtszuständen und Luftbewegungen, Ph.D. Thesis, University of Zurich, Switzerland.
- _____, 1956: Das atmosphärische Ozon als Indikator für Strömungen in der Stratosphäre, Archiv Meteorol., Geoph., Biokl., A9, 87-119.
- _____, 1969: Atmospheric Ozone and Ultraviolet Radiation, in World Survey of Climatology, Vol. IV, H. Landsberg (Ed). Elsevier, Amsterdam.
- Fabry, C., and H. Buisson, 1913: L'absorption de l'ultraviolette par l'ozone et la limite du spectre solaire, J. Phys. Rad., 5, 196-206.
- Fritz, S., 1970: Earth's radiation to space at 15 microns: Stratospheric temperature variations, J. Appl. Meteor., 9, 815-824.
- Haagen-Smit, A.J., 1952: Chemistry and physiology of Los Angeles smog, Ind. Eng. Chem., 44, 1342-1346.
- Hanel, R.A., 1969: The infrared interferometer (IRIS) experiment. In The Nimbus III User's Guide, edited by R.R. Sabatini, NASA, Goddard Space Flight Center, Greenbelt, Maryland, 238 pp.
- Hering, W.S., 1964: Ozone-sonde Observations over North America, Vol. 1, Research Report, AFCRL-64-30(I) pp. 1-512, Air Force Cambridge Research Laboratories.
- _____, and T.R. Borden, Jr., 1964: Ozone-sonde Observations over North America, Vol. 2, Environmental Research Paper No. 38, Report AFCRL-64-30(II), Air Force Cambridge Research Laboratories.
- _____, and _____, 1965a: Ozone-sonde Observations over North America, Vol. 3, Environmental Research Report No. 133, Report AFCRL-64-30(III), Air Force Cambridge Research Laboratories.
- _____, and _____, 1965b: Mean Distributions of Ozone Density over North America, 1963-1964, Environmental Research Paper No. 162, Report AFCRL-65-913, Air Force Cambridge Research Laboratories.
- _____, and _____, 1967: Ozone-sonde Observations over North America, Vol. 4, Environmental Research Paper No. 279, Report AFCRL-64-30(IV), Air Force Cambridge Research Laboratories.
- Hunt, B.G., 1966a: Photochemistry of Ozone in a Moist Atmosphere, J. Geophys. Res., 71, 1385-1399.

- Kao, S. -K., and W.P. Hurley, 1962: Variations of the kinetic energy of large-scale eddy currents in relation to the jet stream, J. Geophys. Res., 11, 4233-4242.
- Komhyr, W.D., 1969: Electrochemical concentration cells for gas analysis, Ann Geophys. 25, 203-310.
- Kulkarni, R.N., 1966: The vertical distribution of atmospheric ozone and possible transport mechanisms in the stratosphere of the Southern Hemisphere, Quart. J. Roy. Meteorol. Soc., 92, 363-374.
- London, J., 1963: The distribution of total ozone in the Northern Hemisphere, Beitrag zur Physik der Atmosphere, 26, 254-263.
- Lovill, J.E., 1965: Antarctic spring stratospheric warming as related to upper stratosphere ozone fluctuations, presented at joint meeting IAMRC-CSIRO, Melbourne, Australia, November 1965.
- _____, 1969: Transport processes in orographically induced gravity waves as indicated by atmospheric ozone, Atmospheric Science Paper No. 135, Colorado State University, 78 pp.
- _____, 1970a: Gravity wave measurements as simultaneously, determined by satellite, ozone, and airplane, Arch. Meteorol., Geophys., Bioklim, A19, 13-28.
- _____, 1970b: Dynamics of the structure of the atmosphere over mountainous terrain from 4-70 km as inferred from high-altitude chaff, ozone sensors and superpressure balloons, Atmospheric Science Paper No. 160, Colorado State University, 51 pp.
- _____, 1970c: A note on the variability of ozone at a high mountain location. Arch. Meteorol., Geophys., Bioklim, A19, 439-442.
- _____, and A. Miller, 1968: The vertical distribution of ozone over the San Francisco Bay area, J. Geophys. Res., 73, 5073-5079.
- Nimbus Project, 1969: The Nimbus III data catalog Volume 1, part 1, Goddard Space Flight Center, Greenbelt, Maryland, 238 pp.
- Norrish, R.G.W., and R.P. Wayne, 1965: The photolysis of ozone by ultraviolet radiation. II. The photolysis of ozone mixed with certain hydrogen-containing substances, Proc. Roy. Soc., A288, 361.
- Obasi, G.O.P., 1963a: Poleward flux of atmospheric angular momentum in the Southern Hemisphere, J. Atmos. Sci., 20, 516-528.
- Obasi, G.O.P., 1963b: Atmospheric momentum and energy calculations for the Southern Hemisphere during the IGY, Scientific Report No. 6, M.I.T.

- Paetzold, H.K., 1953: Die vertikale Verteilung des atmosphärischen Ozons nach dem photochemischen Gleichgewicht, Geofis. Pura E. Appl., 24, 1-14.
- Penn, S., 1965: Ozone and temperature structure in a hurricane, J. Appl. Meteorol., 4, 212-216.
- _____, 1966: Temperature and ozone variations near tropopause level voer Hurricane Isabell, October 1964, J. Appl. Meteorol., 5, 407-410.
- Pittock, A.B., 1968: Seasonal and year-to-year ozone variations from soundings over Southeastern Australia, Quart. J. Roy. Meteorol. Soc., 94, 563-575.
- Prabhakara, C., 1969: Feasibility of determining atmospheric ozone from out-going infrared energy, Mon. Wea. Rev., 94, 307-314.
- _____, and B.J. Conrath, 1970: Global distribution of ozone from Nimbus III. Symposium on remote sounding of the atmosphere, C COSPAR, Leningrad, U.S.S.R., 22 May 1970, 12 pp.
- _____, E.B. Rodgers and V.V. Salomonson, 1971a: Global distribution of total ozone derived from Nimbus 3 satellite during April-July, 1969 and its implication to upper tropospheric circulation, NASA Report X-651-71-463, Goddard Space Flight Center, Greenbelt, Maryland, 27 pp.
- _____, B.J. Conrath, L.J. Allison and J. Steranka, 1971b: Seasonal and geographical variation of atmospheric ozone, derived from Nimbus 3, NASA TN D-6443, National Aeronautics and Space Administration, Washington, D.C., 61 pp.
- _____, V.V. Salomonson, B.J. Conrath, J. Steranka and L.J. Allison, 1971c: Nimbus III, IRIS Ozone Measurements over Southeast Asia and Africa during June and July 1969, J. Atm. Sci., 28, 828-831.
- Reed, R.J., J.L. Wolfe, and H. Nishimoto, 1963: A spectral analysis of the energetics of the stratospheric sudden warming of early 1957, J. Atmos. Sci., 20, 256-275.
- Regener, V.H., 1960: On a sensitive method for the recording of atmospheric ozone, J. Geoph. Res. 65, 3965-3977.
- Reinking, R.F., and J.E. Lovill, 1971: A comparison of ice nucleus and ozone concentrations in stratospheric air, J. Atm. Sci., 28, 812-816.
- Reiter, E.R., 1963: Jet-stream Meteorology, Univ. of Chicago Press, 515 pp.
- _____, 1969: Atmospheric Transport Processes, Part 1: Energy Transfers and Transformations. U.S. Atomic Energy Commission, Division of Technical Information, Oak Ridge, Tennessee, 253 pp.

- Reiter, E. R., 1971: Atmospheric Transport Processes, Part 2: Chemical Tracers. U. S. Atomic Energy Commission, Division of Technical Information, Oak Ridge, Tennessee, 382 pp.
- Renzetti, N. A., 1955: An aerometric survey of the Los Angeles Basin, August-November 1954, Rept. No. 9, 333 pp., Air Pollution Foundation, Los Angeles, California
- Russell, J. M., III, 1970: The measurement of atmospheric ozone using satellite infrared observations in the 9.6 μ m band, Ph.D. Dissertation, University of Michigan, 144 pp.
- Scherhag, R., 1969a: Meteorologische Abhandlungen, 101 (5), Institut für Meteorologie und Geophysik der Freien Universität Berlin.
- _____, 1969b: Meteorologische Abhandlungen, 101 (6), Institut für Meteorologie und Geophysik der Freien Universität Berlin.
- _____, 1969c: Meteorologische Abhandlungen, 101 (7), Institut für Meteorologie und Geophysik der Freien Universität Berlin.
- Schiff, H. I., 1964: Reactions involving nitrogen and oxygen, Ann. Geophys., 20 (1), 115-127.
- Starr, V. P., and R. E. Dickinson, 1963: Large scale vertical eddies in the atmosphere and the energy of the mean zonal flow, Geofisica Pura e Applicata, 55, 133-136.
- Van Loon, H., 1964: Mid-season average zonal winds at sea level and at 500 mb South of 25 degrees South, and a brief comparison with the Northern Hemisphere, J. Appl. Meteor., 3, 554-563.
- _____, 1965: A climatological study of the atmospheric circulation in the Southern Hemisphere during the IFY, Part I: 1 July 1957 - 31 March 1958. J. Appl. Meteor., 4, 479-491.
- Volz, F. E., 1952: Über die Zersetzung des Ozons in der troposphäre, Ber. Deut. Wetterdienstes US-Zone, 35, 257-259.
- Vonder Haar, T. H. and V. E. Suomi, 1971: Measurements of the earth's radiation budget from satellites during a five-year period. Part I: extended time and space means, J. Atm. Sci., 28, 305-314.
- Wooldridge, G., and E. R. Reiter, 1970: Large-scale atmospheric circulation characteristics as evident from GHOST balloon data, J. Atm. Sci., 2, 183-194.

APPENDIX II

Continued Documentation of Major Computer Programs
Developed under grant auspices

Program TIMELON

Program O3CONT

PROGRAM: TIMELON

This program contours an array formed by taking the ozone values along a specified latitude line on succeeding days and placing the "lines" in the array by their day number. The analysed data is plotted on microfilm with longitude on the horizontal axis and time on the vertical axis. The time period covered can be varied in units of 1 day up to the total period for which data is available. Each frame of microfilm contains 1 labeled graph.

Input Cards:

Card 1

Columns		<u>Description</u>
1-4	LDAY	Integer, the day no. of the first day to be included in the graph.
5-8	KDAY	Integer, the day no. of the last day to be included in the graph.

Card 2 and 3

Columns		<u>Description</u>
1-80 with format 2014	NODAY	Integer, an array of 23 elements with the day nos. of the days that have no data.

Card 4

Columns	<u>Description</u>
1-80	Alphanumeric label for microfilm

Card 5

Columns	<u>Description</u>
1-50	more labels

Card 6

Columns	<u>Description</u>
1-20	more labels

Method

The ozone values are read from the data tape along with their associated day no., latitude and longitude. Observations outside the time period of the graph to be generated or with a latitude greater than 15° from the desired latitude line and had data are eliminated. The ozone values for the remaining observations are fitted to a Rat-lon grid with 2° increments. After all the observations for one day are processed the grid is interpolated and the values along the specified latitude line are placed in another array according to the day number. The grid is then zeroed and the next days observations are processed. When the observations for the entire time period have been processed, the second array is interpolated to supply the values for (possible) missing days. The array is contoured and the results are plotted on microfilm.

PROGRAM 03CONT

This program objectively contours ozone data and outputs the analysed data on microfilm. The data is contoured over a world map (cylindrical equidistant projection) showing continental outlines and with latitude and longitude lines labelled. Each frame of microfilm contains one world map. The time period covered by each map can be varied in units of 1 day from 1 day to the total period for which data is available.

Input Cards:

Card 1

Columns

(L)line

1-4

LDAY

Description

Integer, day no. of the first day of the time period to be covered by the map.

5-8

KDAY

Integer, day no. of the last day of the time period to be covered by the map (may be same as LDAY).

9-14

LENGTH

Integer, length of the array to be read from tape containing plotter instructions for generating the background map.

two blank lines

Card 2 and 3

blank line

Columns

1-80

NODAY

Description

Integer, an array of 23 elements containing the day nos. of the days that have no data.

Card 4

Columns

1-80

Description

A Yeha numeric label for microfilm.

Card 5

Columns

1-50

Description

more labels

Card 6

Columns

1-20

Description

more labels

Method

The ozone values are read from the data take along with their associated day no latitude and longitude. The day no. is checked to determine if the observation is during the period under consideration. Then the ozone value is tested against extreme reasonable values and bad data is eliminated. The observations passing the above tests are fitted to a Lat-lon grid with 20 increments between grid lines. When all the observations have been processed, the grid is interpolated linearly by rows and by columns. The results are then merged weighting the rows 10 to 1 over columns. The grid is then contoured and the results plotted on microfilm.